

Starshade Technology Development Activity Milestone 6A

Verify Petal Shape on-Orbit Stability

David Webb, John Steeves, Flora Mechentel, Manan Arya, S Case Bradford, Doug Lisman,

Jet Propulsion Laboratory, California Institute of Technology, Pasadena CA

David Opland, Gregg Freebury,

Tendeg, Louisville CO

Jamie Abbott,

JLA, San Diego CA

Sze Chaung, Steve Connell

Northrup Grumman, San Diego CA

Jim Tucker

Southern Research, Birmingham AL

Siu-Chun Lee and Larry Chan

Applied Sciences Lab, Inc., Baldwin Park CA

CONTENTS:

CONTENTS:	1-1
Executive Summary	1-3
1 Introduction	1-4
2 Flight Design	2-7
2.1 Flight Mechanical Architecture	2-7
2.1.1 Petal Subsystem	2-8
2.2 Thermal Environment	2-9
2.2.1 Thermal Analysis Model & Thermal Design	2-9
2.2.2 Thermal Analysis Results	2-10
2.3 Validated vs Ideal Petal-Width Bias	2-12
2.4 Worst-Case Predicted Performance	2-15
3 Model Validation	3-17
3.1 Model Validation Approach	3-17
3.2 Metrology Technique	3-19
3.2.1 Abbe Error	3-21
3.2.2 Data Losses	3-22
3.2.3 Atmospheric Effect	3-22
3.2.4 Measurement Uncertainty	3-23
3.3 Petal Prototype Test Article	3-24
3.3.1 Design	3-24
3.3.2 Manufacture	3-25
3.3.3 Analysis Model	3-27
3.4 The Test Results Correlation to Prediction	3-30
4 Flight Design Validated Analysis Model & On-orbit Performance	4-33
4.1 Approach	4-33
4.2 Analysis Model	4-33
4.2.1 Petal Subsystem	4-34
4.3 Flight Design FEM Correlation to Prototype FEM	4-35
4.4 On-Orbit Performance Predictions	4-36
5 Milestone Analysis & Conclusions	5-39
5.1 Petal-Width Bias Error	5-39
5.2 Instrument Contrast Results	5-41
5.3 Concluding Statement on Performance	5-43
5.4 Future Work	5-44
Acknowledgements	5-46
Acronyms	5-47
References	5-48
6 Appendix A: Petal-Width Bias	6-49
6.1 Key Components of The Petal	6-49
6.2 Petal Shape Variations	6-50
6.3 Correlation Between Instrument Contrast and Petal-Width Bias	6-52
6.4 Summary of Simulation Results	6-55
7 Appendix B: Designing-Out Midspan Bowing	7-56

8	Appendix C: Additional Plots & Figures	8-59
9	Appendix D: Material Properties.....	9-67
10	Appendix E: Adhesive Thickness Mapping	10-70
11	Appendix F: Optical Edge Layup Geometry	11-71
12	Appendix G: Batten to Optical Edge Joint Effect on Edge Shape - Midspan Bowing.....	12-72
13	Appendix H: Prototype Petal Midspan Sensitivity Studies	13-75
14	Appendix I: Lattice-Tip Transition Strain	14-77
15	Appendix J: Petal-Inner Disk Cross Term.....	15-79

Executive Summary

We demonstrate compliance with S5 Milestone 6A, with large margin on the nominal performance, as well as positive margin on a worst-case performance scenario, against a conservative interpretation of the requirement. This milestone concerns the on-orbit thermal stability of the petals, over the full range of observational sun angles. Maximum expected thermally induced petal-width bias error versus sun angle was predicted via a system model. The analysis model was validated at the assembly level, via dimension versus temperature measurements of a sub-scale, medium-fidelity, prototype test article of the petal assembly, that included the dimension critical features. The ideal petal-width bias for the thermal environment was determined, which was the basis of comparison for the validated petal-width bias performance. Also included was a worst-case performance analysis that resulted from analyzing the system at the limits of the 3-sigma measured material bounds, combined with a $\pm 10^{\circ}\text{C}$ temperature uncertainty, with all parameters biased in the direction of worse performance.

JPL and Tendeg performed the design, analysis and fabrication of the prototypes and test article, and Northrop Grumman, in collaboration with Southern Research, designed and implemented the displacement-measuring interferometry technique, used to characterize the petal critical dimension versus temperature. This test data was used to compare to the model predictions.

1 Introduction

This report details the S5 efforts to verify starshade petal on-orbit thermal stability performance (KPP 6) and is intended to close out the S5 technology milestone 6A, which reads:

Petal subsystem with shape critical features demonstrates on-orbit thermal stability within ± 80 microns by analysis using a validated model of critical dimension vs. temperature.

This specification applies over a 40° to 83° star-sun angle (henceforth called sun angle) range that bounds the HabEx and WFIRST-Starshade Rendezvous Mission (SRM) cases. Table 1-1 shows the petal error budget sub-allocations to global petal-width bias error, as well as random petal-width bias errors.

The starshade contrast performance is affected by thermal deformations on orbit, and is dominated by petal width changes. The error budget was determined by considering the change in instrument contrast produced by a uniform petal-width strain, in parts per million, of the petals with respect to the nominal shape. In practice however, the petals undergo non-uniform thermal deformations, with the largest strains occurring at the narrow petal tips. The petal-width bias is a metric that was determined to characterize the thermal deformations ultimately driving the optical performance of the starshade. Practically speaking, petals with a constant width strain equal to the petal-width bias, will produce very similar optical performance as petals with realistic flight-like variations around the petal-width bias. Appendix A: Petal-Width Bias details the calculation and correlation of this metric to our quantity of interest, change in instrument contrast.

For a given on-orbit thermal environment, the global petal-width bias error is the difference between the petal-width bias of the flight-design, per a validated finite element model (FEM) prediction, and the ideal petal-width bias. The ideal petal-width bias was determined for each sun angle by using a breakout model of the width-wise section of the preliminary petal design. The ideal petal-width bias is the same as that explained in milestone 8A, which describes the inner disk thermal stability. The ideal inner disk design strains commensurately with the ideal petal-width.

Global petal-width bias error applies as the average petal-width bias error of the combined 24 flight petals, whereas the random error is the maximum error that any individual petal may exhibit. For this milestone, because we only test one petal, we demonstrate that the one petal demonstrates the tighter requirement of global petal-width bias error. In *conservatively* constraining ourselves to this tighter requirement, the random error sub-allocations are also satisfied. Petal-width bias is the most critical dimension for instrument contrast, and is largely determined by the battens, which are very low coefficient of thermal expansion (CTE) rods that are produced via a carbon fiber – epoxy matrix pultrusion process that is very tunable, repeatable and consistent between samples from the same lot.

Note that even though Table 1-1 includes allocations for petal lengthwise strain, these error terms are not discussed in this report with as much detail as the widthwise strain terms. This is because the contrast allocations to these terms are small (less than 5% of the total). Additionally, the allocations towards these length strain terms allow for large margins against predicted performance, based on the validated FEM results.

Table 1-1 Milestone 6A sub-allocations. Petal-width bias error dominates contrast for the petal, and is measured as the difference in bias from the validated model and the ideal. Petal-width bias (global) is a max tolerance, and petal-width bias (random) is evaluated at 3-sigma probability. There are also allocations for non-uniform widthwise petal strain (i.e. variations around the bias), and relatively small allocations for petal lengthwise strain.

Error term	Strain (ppm)	Instrument contrast degradation ($\times 10^{-12}$)
Petal-width bias (global)	25	5.78
Petal-width bias (random, 3σ)	50	0.43
Petal non-uniform width strain (global)	150	1.45
Petal-length bias (global)	50	0.30
Petal-length bias (random, 3σ)	100	0.03
Total		8.00

The milestone verification approach is to validate a FEM for predicting thermo-elastic distortion (TED) of a sub-scale, medium-fidelity prototype petal with shape critical features, and then to apply the same material properties and validated model construction technique to the flight design. The prototype petal is flight-like in terms of all component cross-sectional dimensions and materials, but is $\frac{3}{4}$ scale in terms of the overall assembly width and $\frac{1}{2}$ scale in terms of overall assembly length. The reduced dimensions support the use of available facilities. Not included in the prototype petal are the optical shield, as well as the pop-up ribs, which do not participate in in-plane shape maintenance; however, these will be included in milestone 6B.

The prototype petal in-plane shape was measured as a function of steady-state bulk average temperature in a thermal ‘hot/cold box’ at ambient pressure, because thermal gradients have a small effect on the milestone requirement, per Section 3.1. A laser-based interferometric system measured the change in separation between discrete points on the prototype petal that well define the structure’s thermo-elastic deformation response, in both width and length, to characterize the overall structure’s behavior. This milestone activity evaluates the nominal performance of the validated flight analysis model as the baseline case. We also evaluate a worst-case, in which we evaluate the performance of the validated FEM at the 3-sigma extremes of the as-measured variation in CTE’s, combined with on-orbit temperature uncertainty, all pushed in the direction of worst-case for performance, and show compliance with the milestone requirement. This assumes *all* battens and other petal materials are at the extremes of the CTE sample population, which does not account for our ability to utilize a set of material selection criteria.

Correlation was drawn between the test article measurements and FEM prediction. For the performance metric, which was our validation criterion, the difference between the FEM predictions and the measurements was less than 13% across all correlation temperatures, which is within the bounds of measurement uncertainty.

It is worth noting that this test article is also being used to satisfy milestone 5A by demonstrating shape accuracy at room temperature after thermal and deploy cycles. Milestone 5A did not interrupt 6A testing, and deploy cycling was performed after the completion of the 6A measurement effort.

The remainder of this document is organized as follows. Section 2 presents the flight mechanical architecture/design, thermal environment/analysis, the validated vs. ideal petal-width bias, and description of a worst-case predicted performance analysis. Section 3 describes the model validation approach, metrology technique, prototype test article and model correlation results.

Section 4 describes the flight design models, correlation between the flight and test article models, as well as on-orbit performance predictions. Section 5 presents the predicted on-orbit performance, and compares it to the milestone, as well as resulting instrument contrast along with conclusions and plans for future work.

2 Flight Design

2.1 Flight Mechanical Architecture

The Starshade is a deployable structure that has three subsystems, the inner disk, the petal, and the petal launch restrain and unfurl subsystem (PLUS), see Figure 2-1. The petals and truss are designed to be deployed independently, in a two-phase deployment. First, the PLUS quasi-statically releases the petals from their furled (launch) condition, then the truss launch locks are released, and the truss deploys the petals passively to their design diameter. The PLUS is jettisoned after unfurling the petals, and does not contribute to on-orbit stability.

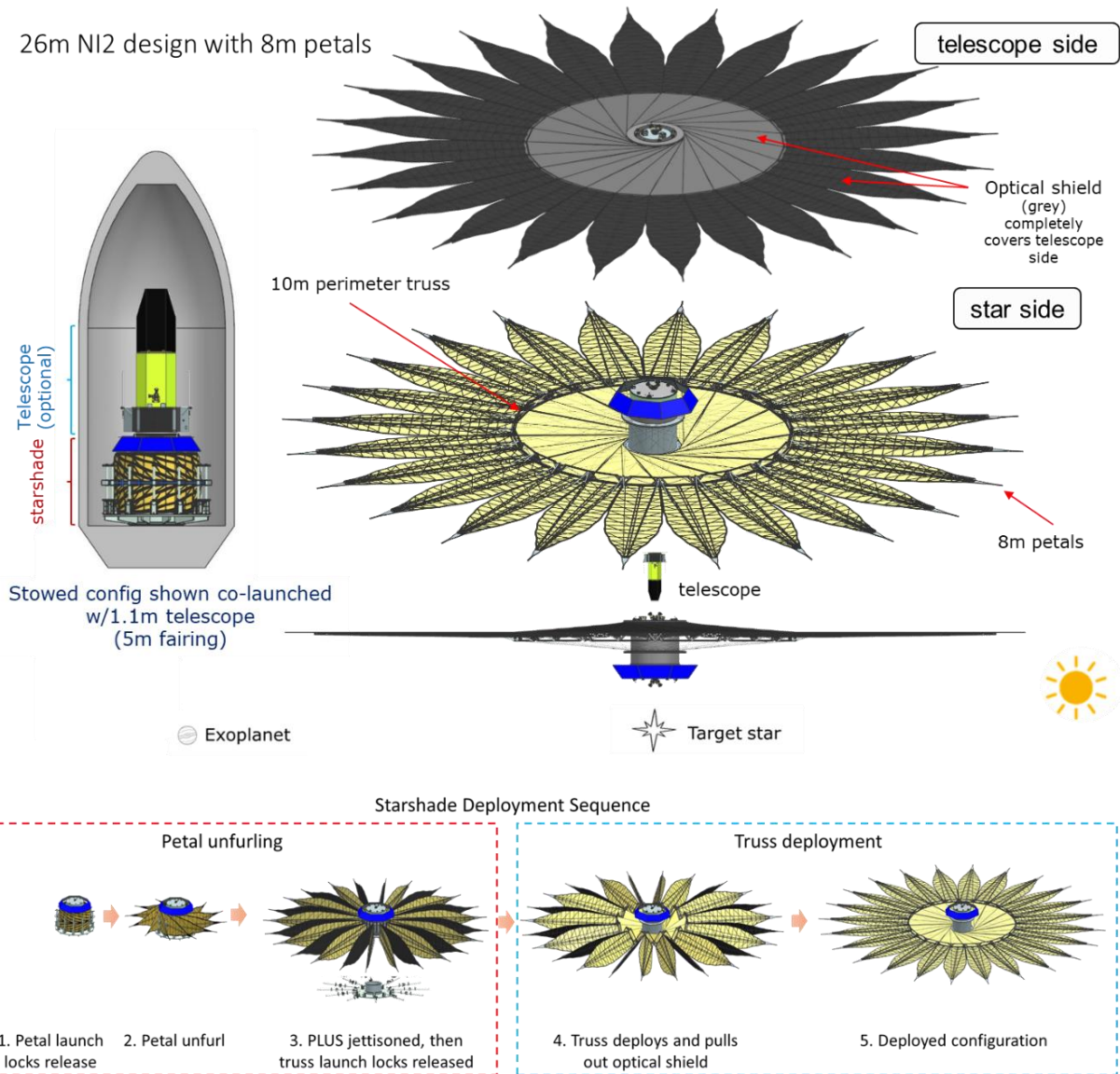


Figure 2-1. Starshade mechanical system including deployed and stowed configuration with relative position of starshade, telescope and star (top). Deployment sequence for the starshade, beginning with petal unfurling, and completing with deployment of the perimeter truss (bottom).

Part of the on-orbit stability design is to minimize load coupling between the petal and disk, which reinforces the error budget breakdown of petal position and petal shape as independent

parameters. The actual interfaces are of course non-ideal, and this coupling is present in the analysis models. The focus of this milestone is the petal on-orbit thermal stability. For a more detailed description of all starshade subsystems and the deployment sequence, see the [Probe Study \[2\]](#) and [HabEx reports \[3\]](#). The on-orbit thermal stability of the inner disk is discussed in the milestone 8A report.

2.1.1 Petal Subsystem

The petal subsystem is designed to be stiff in-plane to maintain the precise shape of the edge. This is important on-orbit, and just as importantly, on the ground during manufacture, test and launch. This is accomplished with a repeating doublet of triangular trusses, formed by the battens, braces, center spine and optical edge. The design is a result of analysis that showed the petal would be sufficiently stiff in-plane to maintain its shape through ground handling for verification after test environments. The batten spacing increases from root to tip, because it is dictated by the petal furling radius. The design of the petal can be seen in Figure 2-2. The petals are positioned and attached to the truss with three hinges at the root of the petal; the center hinge is responsible for lateral location, and the edge hinges are allowed to slip in the hinge axis, so as not to over-constrain the petal. The petal is restrained out-of-plane with two struts that connect down from the truss nodes to the bases of the two out-of-plane ribs, that run from the root corners of the petal out to the tip. These ribs provide the out-of-plane rigidity needed to meet the out-of-plane requirement, which is quite loose, at multiple centimeters at the tip. The rib is maintained out of plane with a series of small struts from the rib down to the petal, which forms a small triangular truss between the rib-strut-batten. The rib is piano-hinged along its length at its connection to each batten, and is free to slide along this hinge so as to not over-constrain the rib to the petal. For stowage, the ribs rotate down, which allows the petal to wrap around the central hub for stowage. A small spring in the rib strut, combined with the rib's over-center hinge, deploys the rib on-orbit. The petal is restrained in the launch condition at the cart assemblies, which provide a rigid interface to preload the stack of petals for launch, without imparting large loads into the individual petals. The petal optical shield covers the entirety of the telescope side of the petal, but is loosely connected to the structure so that it does not impart any load from thermal deformation.

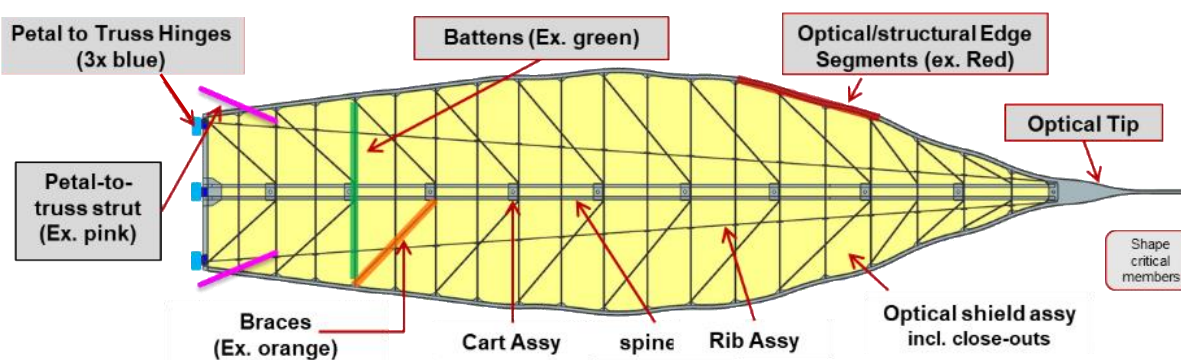


Figure 2-2. Flight petal design is 8 m long, with a maximum width of 2 m. The average width is 1.33 m, which is roughly the same as the 1.3m wide root of the petal, where it interfaces to the truss.

For our concern of on-orbit thermal stability, the critical features of the petal design are trimmed in red in Figure 2-2, and include the battens, braces, and edge. The batten dominates the width stability of the petal, but the brace and spine help maintain the shear structure. The spine does have a second order effect on width as part of the truss-like structure. Each of these critical

features is optimized to provide thermal stability, while also providing the necessary stiffness and strength for the 1g lab environment, furling and launch. Overall stiffness is easily achievable because the carbon fiber reinforced polymer (CFRP), from which they are constructed, has a high stiffness to mass ratio. Per Section 1, the battens are specifically selected to be a uni-axially pultruded carbon fiber / epoxy matrix, providing for a tunable rod, that has very consistent material properties across a production lot of 100's of meters. The braces are made from a similar pultruded rod of a thinner cross section, to allow it to furl with the petal. The spine and edge are an M55J-cyanate ester laminate, that allows the coefficient of thermal expansion (CTE) to be tuned, while also providing strength for interfacing to the petal launch tie-down cart assemblies. Ultimately, the CFRP materials layups and pultrusions will be optimized for the thermal environment, which are tunable parameters.

2.2 Thermal Environment

The thermal environment on orbit is a function of the sun orientation with respect to the starshade, defined herein as the angle of the sun with respect to the starshade normal, see Figure 2-3. Observation angles are bounded by the HabEx mission parameters of sun angle 40° to sun angle 83° . The starshade spins at a rate of $1/3$ RPM about its principal axis, which is co-axial with the long axis of the center hub. Sun angles less than 40° will only be experienced during retargeting of the starshade, and therefore do not affect thermal stability during observation, and angles greater than 83° are also not expected during observation. It is required that the starshade meet on-orbit shape stability for the given starshade temperature profile resulting from that range of sun angles.

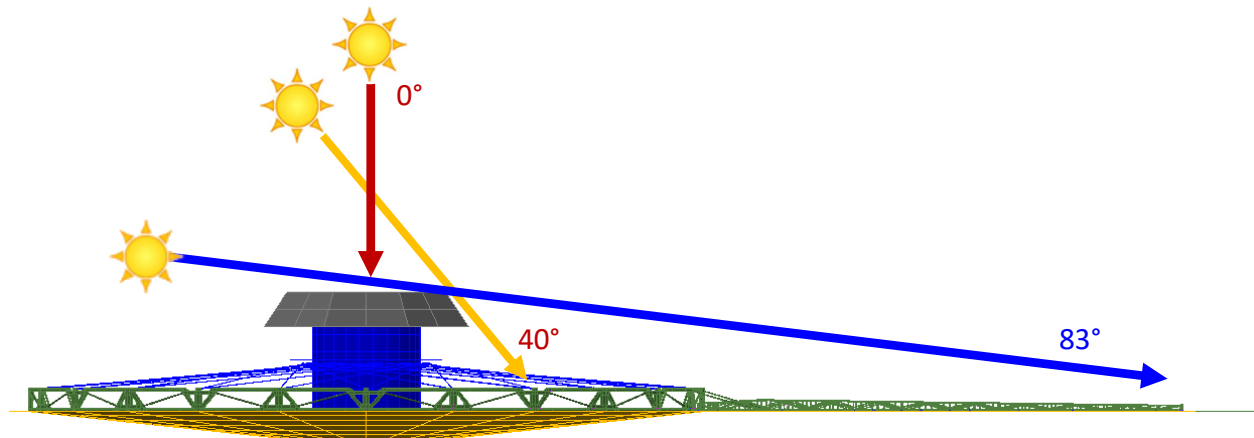


Figure 2-3. Sun angle is defined with respect to starshade normal, which equals a sun angle of 0° . Observation angles are bounded by the HabEx mission parameters of sun angle 40° to sun angle 83° .

2.2.1 Thermal Analysis Model & Thermal Design

The flight design was modeled in the Thermal Desktop analysis software package; the model can be seen in Figure 2-4. The inner disk, with its perimeter truss, spokes and hub, is well detailed, with all components relevant to thermal performance present. Also attached are two detailed petals that include all hardware and shielding, along with 22 'flat', low-detail petal shields, that provide the surrounding thermal environment for the detailed petals and truss; this was done to greatly reduce model run time. The effect of detailed vs 'flat' petals for the thermal environment was studied and shown to be a valid assumption. The temperatures of the two detailed petals are evaluated in a transient analysis, and the petals' temperatures are exported to each of the 12

positions around the starshade to obtain the temperature profile of all 24 petals. These temperatures are then mapped to the structural model.

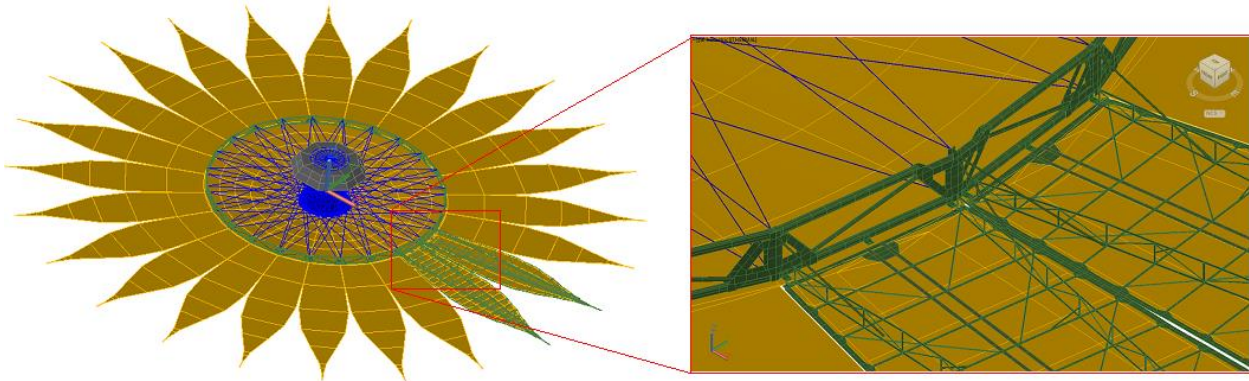


Figure 2-4 Starshade thermal analysis model includes a detailed inner disk including perimeter truss, and two detailed petals that are surrounded by simplified petals that provide an accurate thermal environment.

The thermal design approach of the starshade is centered around cold-biasing the structure, and minimizing the temperature range, resulting in smaller thermal strain variation of the shape critical components. To achieve this, each component in the structure is wrapped, or covered, in a single layer of Silicon-doped Kapton insulation, which is aluminized on the anti-sun (inward facing) surface, giving it a low solar radiation absorptivity to emissivity ratio.

2.2.2 Thermal Analysis Results

The starshade spins at a rate of 1/3 RPM, which results in a variation in the batten temperature of $\sim 2^{\circ}\text{C}$ through the spin. Sun angles of 40° and 83° represent the hottest and coldest thermal environments over the observation angles for which the starshade must meet thermal stability requirements. Figure 2-5 shows the sun angle 40° and 83° thermal plots that result from the thermal analysis.

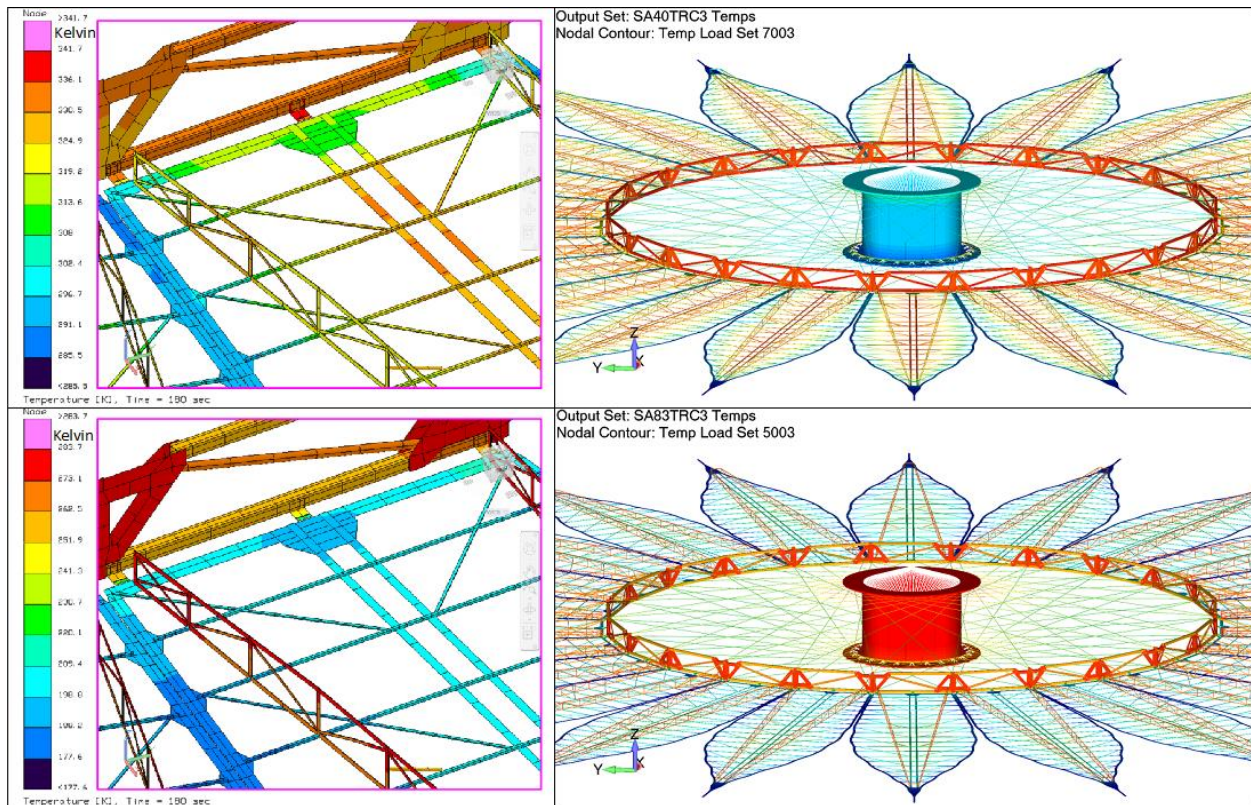


Figure 2-5. Thermal plots for sun angles 40° (top) and 83° (bottom), the extremes of the observation orientations. Note that view orientation is NOT the sun angle. Detailed view of the inboard section of the petal on the left, with scale bar in Kelvin, and to the right, the entire starshade structure.

We are concerned with the average temperature of the petal battens, which drive the petal width bias, as explained in Section 3.1. Figure 2-6 shows the average batten temperature is bounded by sun angle 40° at 50.4°C on the hot extreme, and sun angle 83° at -60.5°C on the cold extreme.

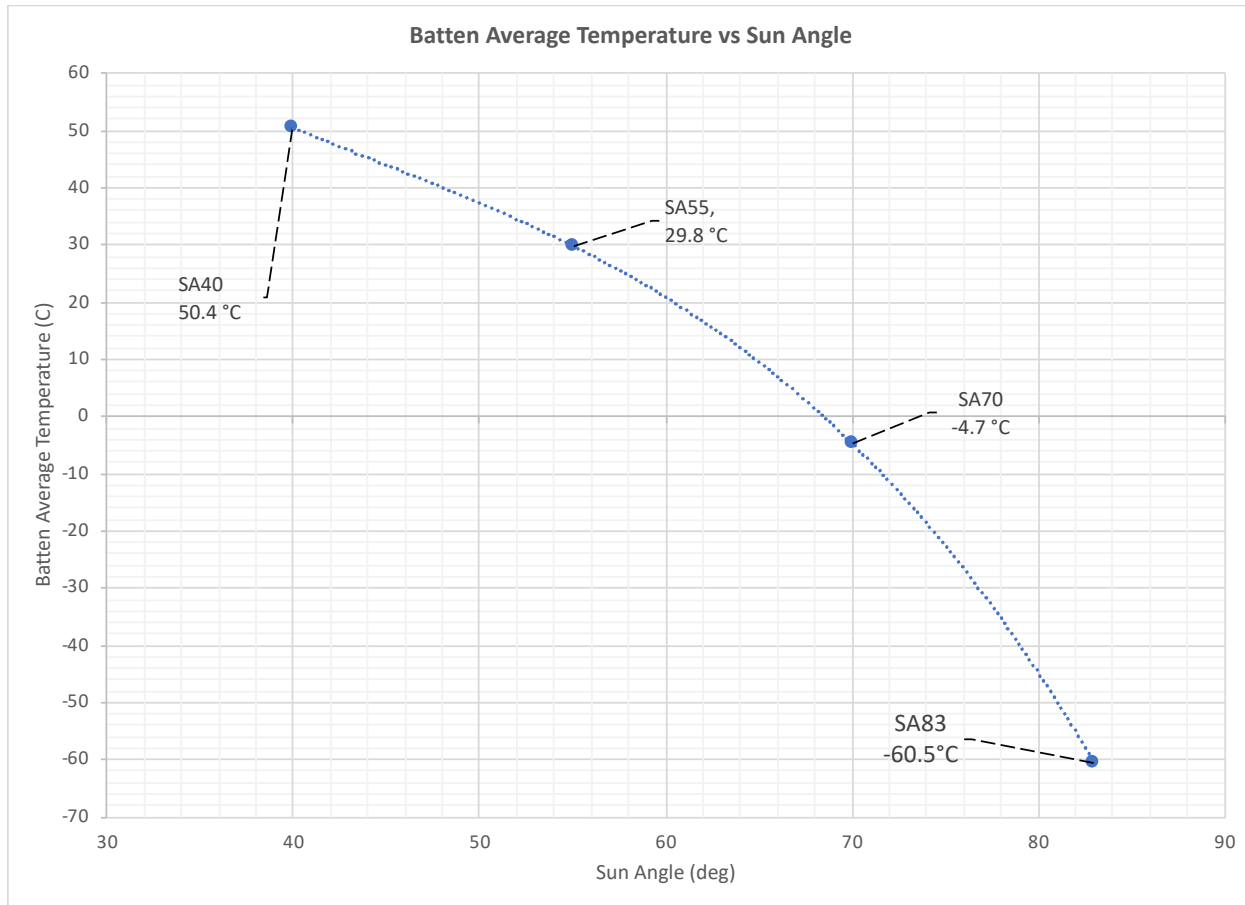


Figure 2-6. Average temperature of the petal battens as a function of sun angle. The batten temperature is bounded by 50°C at sun angle 40, and -60°C at sun angle 83, observing sun angles for the starshade. This temperature range was the basis for the prototype petal test temperature range. More sun angles cases were run to better characterize the batten temperature vs sun angle curve, however only the sun angles analyzed for performance are shown here. A trendline connects the data points, which well approximates the entire data set. Note that at SA60, the average batten temperature is approximately the reference temperature of the hardware, 20°C .

2.3 Validated vs Ideal Petal-Width Bias

Per discussion in Section 1, the *petal-width bias error* is the difference between the petal-width bias of the flight-design, *validated finite element model (FEM) prediction*, and the *ideal petal-width bias*. To establish the ideal petal-width bias for a given thermal environment (sun angle range), a width-wise section of the preliminary petal design, at the batten, was modeled as a standalone breakout model, see Figure 2-7. Because material properties were not fully characterized before the detailed design was complete, preliminary values were used in this model. The different material properties, and the assembly-level structure behavior, both drive petal-width bias, and thus the validation was an exercise in characterizing these two aspects of the design, as it pertains to petal-width bias. Milestone 6B, and a flight program, will benefit from fully characterizing material properties *before* the detailed design is complete, as well as refining the design to optimize for petal-width bias behavior at the structure level.

Once the ideal petal-width bias as a function of sun angle was established using the breakout model, it was frozen for the remainder of the program. This was necessary to allow the inner disk program, milestone 8A, to work to a common design requirement. As detailed in milestone 8A, Section 2.3 (Actual Disk Radius Design vs Ideal Disk Radius), the actual disk design

tries to best match the predicted thermal strain of the petal-width dimension. This matched thermal strain between inner disk and petal-width minimizes the effect on instrument contrast.

Petal-width thermal strain is the product of the change in temperature from the reference temperature (20°C), and the effective CTE of the combined components and materials in the width-wise direction of the petal. The thermal strain of the width-wise section of the petal was modeled utilizing industry standard modeling tools, including CompositePro for Classical Laminate Theory (CLT), and FEMAP with Nastran. The petal-width thermal strain was evaluated at a batten location along the petal that was equal to its average width of the petal (1.3 m), see Figure 2-7.

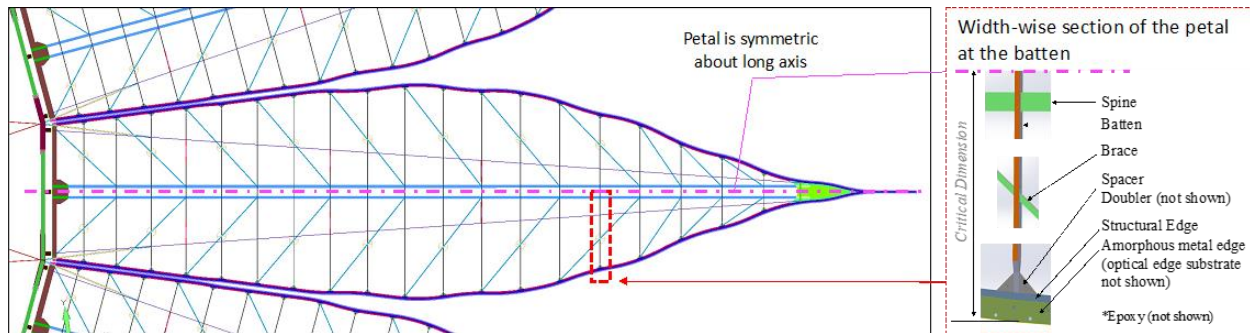


Figure 2-7. Finite element model of the detailed flight petal design. A breakout model of the petal width at the batten was used to determine the ideal petal-width bias performance as a function of sun angle. The petal is symmetric about the long axis, and thus only half the petal width needed to be modeled.

The ideal petal-width bias that resulted from the analysis of the breakout model of the petal preliminary design is plotted in Figure 2-8. Petal-width bias due to thermal strain is plotted in parts per million (ppm) as a function of the observing sun angle in degrees. The milestone requires the difference (error) between the validated flight FEM prediction and the ideal value be less than ± 20 ppm. Petal-width bias due to thermal distortion is relative to the as-built 20°C reference temperature, and the resulting petal design is as close to zero thermal strain as possible with the materials available. To minimize variability of the petal-width bias, the beforementioned uni-axial pultruded CFRP rod material is used for the battens, which dominate the width of the petal. The variability and importance of the batten rods is discussed in detail in Section 2.4.

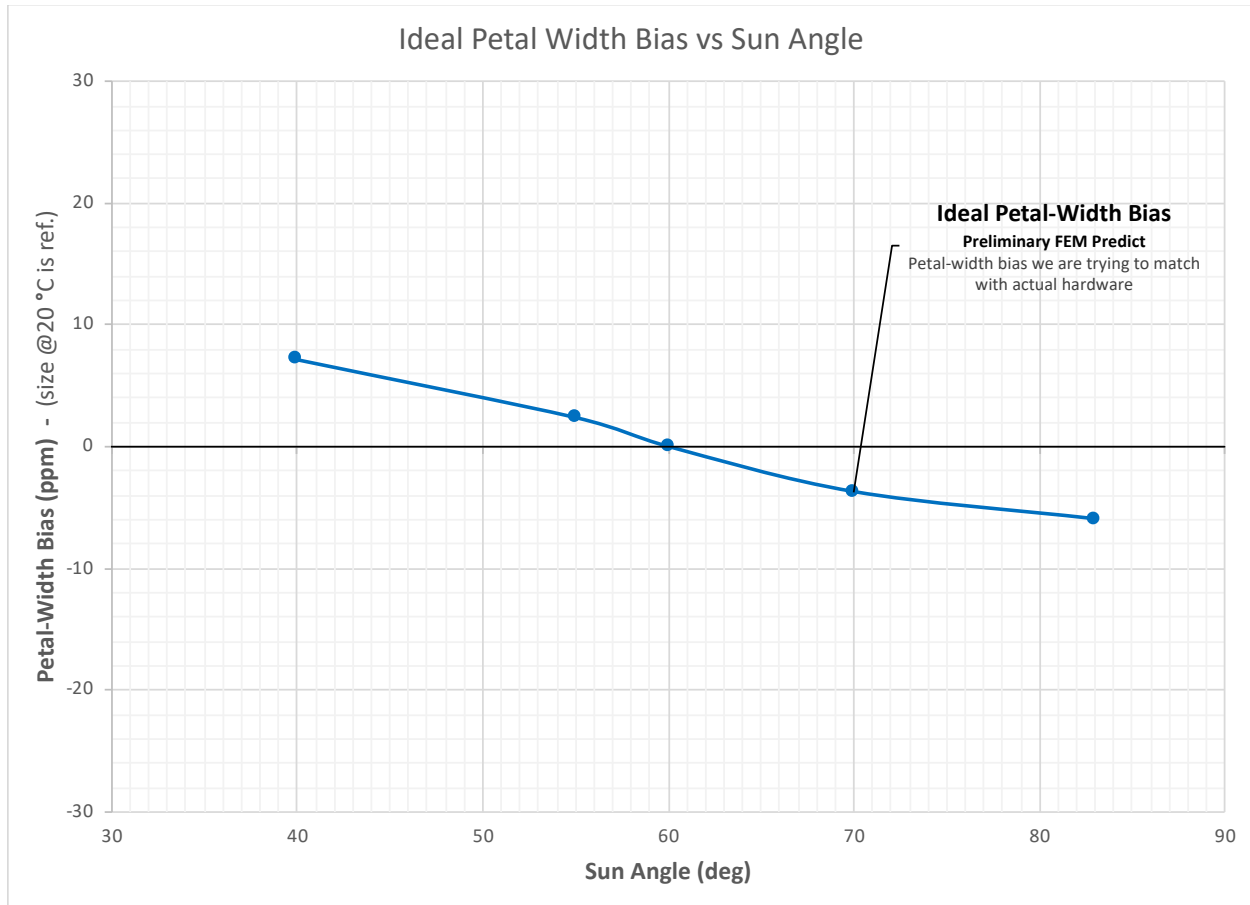


Figure 2-8 Petal-width bias in ppm as a function of observational sun angle in degrees. This was predicted by analyzing a breakout model of the petal-width at the batten located at the average petal width. To constrain the petal-width at the reference temperature, we include the approximately zero petal-width bias condition at SA60; which is carried through the analysis.

Milestone 6A is considered iteration 1 of the ideal petal-width bias error, where we compare the as-built validated FEM results to that of our preliminary petal-width bias performance prediction, upon which the requirement was based. Similarly, milestone 8A was iteration 1 of the actual disk radius. Upon the completion of milestones 6A and 8A, the ideal petal-width bias will be updated for milestone 6B, based on the validated FEM prediction of petal-width bias. This is an important point, because it was discovered that for the as-built petal, the thermal deformation results predicted by the breakout model of the petal width at the batten location did not capture bowing between the battens, which has a substantial effect on performance. The ideal petal-width bias will be updated based on the validated petal analytical model described below, which captures this bowing effect. As such, this bowing effect will not contribute to petal-width bias error in the future. The actual truss design will then be updated for milestone 8B, to best match that new ideal petal-width bias.

Milestone 6B will characterize the constituent materials before freezing requirements, which will minimize error to only the variation in material properties within the lot of material that is ordered. This program achieves this requirement without that advantage, and thus the results here are thought to be conservative.

2.4 Worst-Case Predicted Performance

The nominal finite element analysis case utilizes the average thermal strain performance of the suite of material coupons for each material/component, which represent the lot of materials from which the prototype test article was manufactured. The average of the material properties can vary from lot to lot, due to the material production process. While this process is tunable to meet the starshade requirements, and has been demonstrated on other programs, we wanted to understand the sensitivity to this parameter, and show capability for meeting the requirement at the extremes of the current production lot. In doing this, we conservatively assume the materials and components of *all petals* exhibit material properties at the 3-sigma bounds of the measured coupons. This represents a worst-case petal-width bias performance for the given material properties, satisfying the 3-sigma random bias sub-allocation term. Additionally, because we are assuming all petals exhibit these 3-sigma material property performance bounds, the worst-case performance prediction falling within the global bias sublocation term requirement, we add meaningful confidence to our ability to produce 24 petals within the requirement.

To demonstrate this, we calculated the 3-standard deviation CTE bounds for each of the materials utilized in the petal to predict a worst-case CTE (largest thermal strain) for each material. The battens are the components that have the largest contribution to petal-width strain performance. Figure 2-9 shows the average thermal strain as a function of temperature for the batten thermal strain test coupons, as well as the calculated 3-standard deviation bounds of that sample set. Appendix D: Material Properties contains all the material inputs for the nominal case of the finite element model, and also includes Figure 9-1, which shows the thermal strain vs temperature for the adhesive (EA9394) used to bond the structure together, and shows the calculated 3-sigma values used as inputs to the worst-case performance prediction. The adhesive is the second largest contributor to petal-width thermal strain after the battens. This process is performed for all materials and components in the petal, and the 3-sigma CTE's are fed back into the model. Appendix D: Material Properties contains the driving material CTE's.

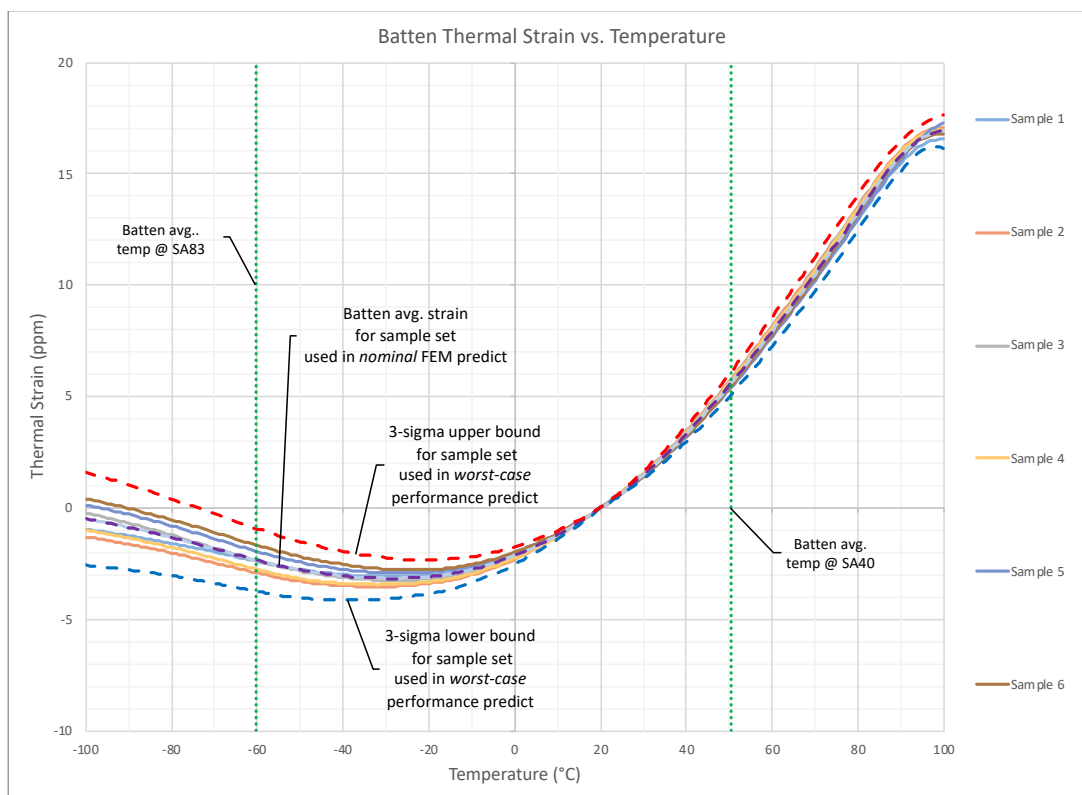


Figure 2-9. The plot shows the thermal strain performance in ppm vs temperature for each of the batten coupon samples measured for this program; the battens have the largest effect on petal-width strain. The average performance is used as an input to the nominal on-orbit thermal environment case. Also plotted are the calculated 3-sigma bounds of the sample set, which represents the max expected variation from this lot of materials, and were used as a material input in the worst-case performance prediction. The average temperature of the battens is -60°C for SA83 and 50°C for SA40. The samples were cut from the lot of materials from which the petal battens were made, and were measured at the Interferometric Metrology Facility at NGIS described in milestone 8A.

The worst-case performance prediction conservatively assumes that all components and materials that create the structure of the petal are biased to the 3-sigma CTE bounds of the coupon set measured for this program, in the worst-case direction. We then include $\pm 10^\circ\text{C}$ temperature uncertainty on the starshade structure. While there is a matrix of variations for combining 3-sigma CTE bounds and the $\pm 10^\circ\text{C}$ temperature uncertainty, the driving cases for performance are invariably the ones that drive larger thermal strain at the temperature (sun angle) extremes.

The resulting worst-case for SA40 is the larger thermal strain 3-sigma bound (red dashed curve) combined with increasing the starshade temperature in the FEA model by 10°C . For SA83, we take the blue dashed 3-sigma curve (which is more negative) and bias the starshade 10°C colder in the FEA model. The 10°C temperature uncertainty is based on historical data. The results of the worst-case performance prediction are presented in Section 4.4 along with the nominal results.

3 Model Validation

3.1 Model Validation Approach

The model validation approach was to build a sub-scale prototype test article, that included all of the critical features for thermally induced mechanical deformation performance, and then correlate thermal deformation test measurements to a detailed finite element model of the test article. The critical petal dimension is the petal width, and was therefore the focus of most of the measurement locations, but petal length and shear were also measured for overall structure characterization and as a check on overall structure correlation.

The error in petal-width bias dominates instrument contrast performance, and is our metric for on-orbit performance. In order for our model to be utilized for on-orbit performance prediction, it is necessary that our model accurately predict petal-width bias. To satisfy this, we define our model validation criterion as the following:

The model must predict the petal-width bias of the prototype petal within the uncertainty of the measurement system.

For this validation criterion, the uncertainty of the petal-width bias for the prototype petal is clearly identified as the uncertainty in the measurement system. In other words, our uncertainty in our prediction of the petal-width bias for the prototype petal is bounded by the measurement uncertainty that validates the model. For the flight petal, we must define an additional uncertainty associated with scaling. Because the prototype well represents the structural characteristics of the flight petal, more on this below, the primary concern is scaling. This is addressed by scaling the length-dependent portion of the measurement uncertainty from prototype up to flight scale, which would represent the measurement uncertainty associated with the future model validation measurements of a flight scale petal. Lastly, the uncertainty in the performance metric, petal-width bias, must be added before comparing the flight petal performance to the requirement.

For the test article to be most relevant to the flight design, the prototype petal was designed to very closely match the driving structural characteristics of the flight design, including component materials, cross-sectional dimensions, joint geometry and adhesive, and overall structure geometry.

We then measured locations on the petal structure to correlate to our FEM; we chose locations that were deterministic indicators of the petal assembly critical dimension behavior, see Figure 3-1. Deterministic locations along the edge are those that are very stiff; namely at the intersection of the batten with the optical edge, labeled on Figure 3-8, because the edge is constrained by the battens at these locations. We also measured the optical edge midspans, which are the sections of edge between each batten, which allowed us to characterize the edge with greater spatial frequency. The midspans present a challenge in that the edge is structurally less deterministic at these locations, because the structure is more compliant (soft) in these regions, as there is no batten there to constrain it. Nonetheless, the entire edge is important, which is why we measure the edge at the midspans locations.

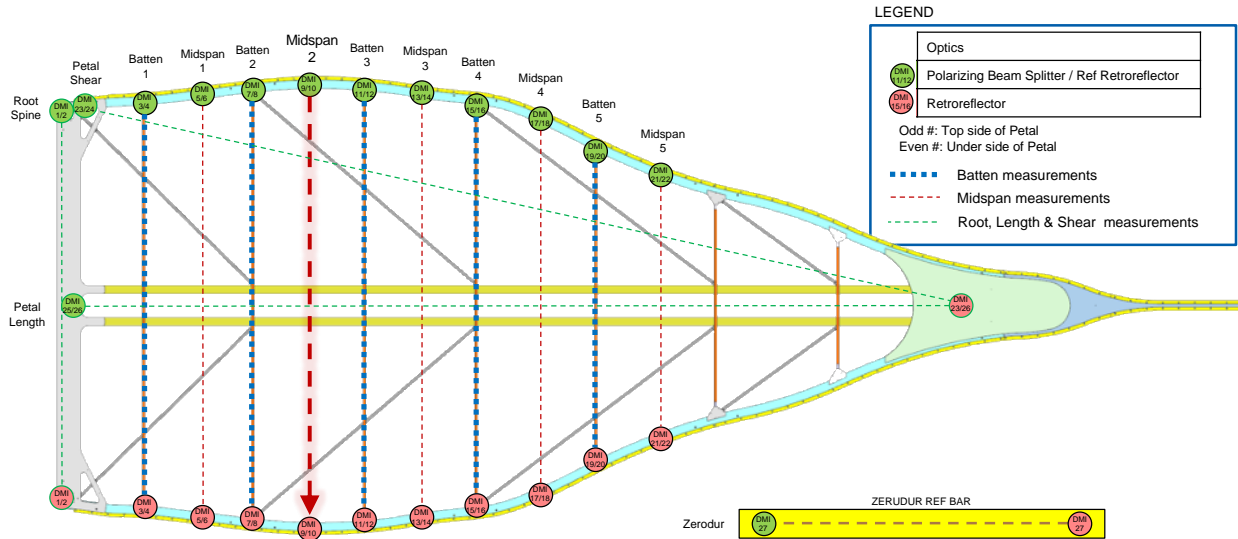


Figure 3-1. Prototype petal test article with measured dimensions identified. Each retroreflector reference (green) to target retroreflector (red) represents a petal dimension measurement. Midspan 2 is highlighted and enlarged as an example of a width-wise measurement. At each petal measurement location, two measurements were made, one top, one bottom, and then the average was taken to compensate for Abbe error. The Zerodur reference bar is very near zero CTE, and was measured to confirm that the correction factors for changes in index of refraction of the air during test were correct.

The prototype was tested in a bulk temperature soak condition, whereas the flight on-orbit environment will have gradients across the petal. To ensure that bulk temperature testing was a meaningful test (i.e. that gradients were not a significant effect that we should capture), we simulated the flight petal FEM in bulk temperature conditions, and assessed the petal-width bias for each bulk temperature condition. We then co-plotted the on-orbit sun angle environment cases, utilizing batten average temperature to map to the bulk temperature cases. Figure 3-2 shows that the on-orbit cases indeed correlate extremely well to the bulk temperature cases, with the difference in performance between the sun angle cases, and the bulk temperature cases, being less than 5%. An investigation into the cause of the petal-width bias difference between bulk and gradient cases, showed that it was driven by the increased thermal strain between components due to their different temperatures. In utilizing our bulk temperature soak model validation to predict on-orbit performance, it is only our uncertainty in the effect of thermal gradient that creates an error between our bulk soak model and the on-orbit gradient case. At less than 5% effect on petal-width bias, the uncertainty in that 5% represents a very small variation in the on-orbit environment performance prediction. For this reason, bulk soak temperature testing was deemed sufficient for this program.

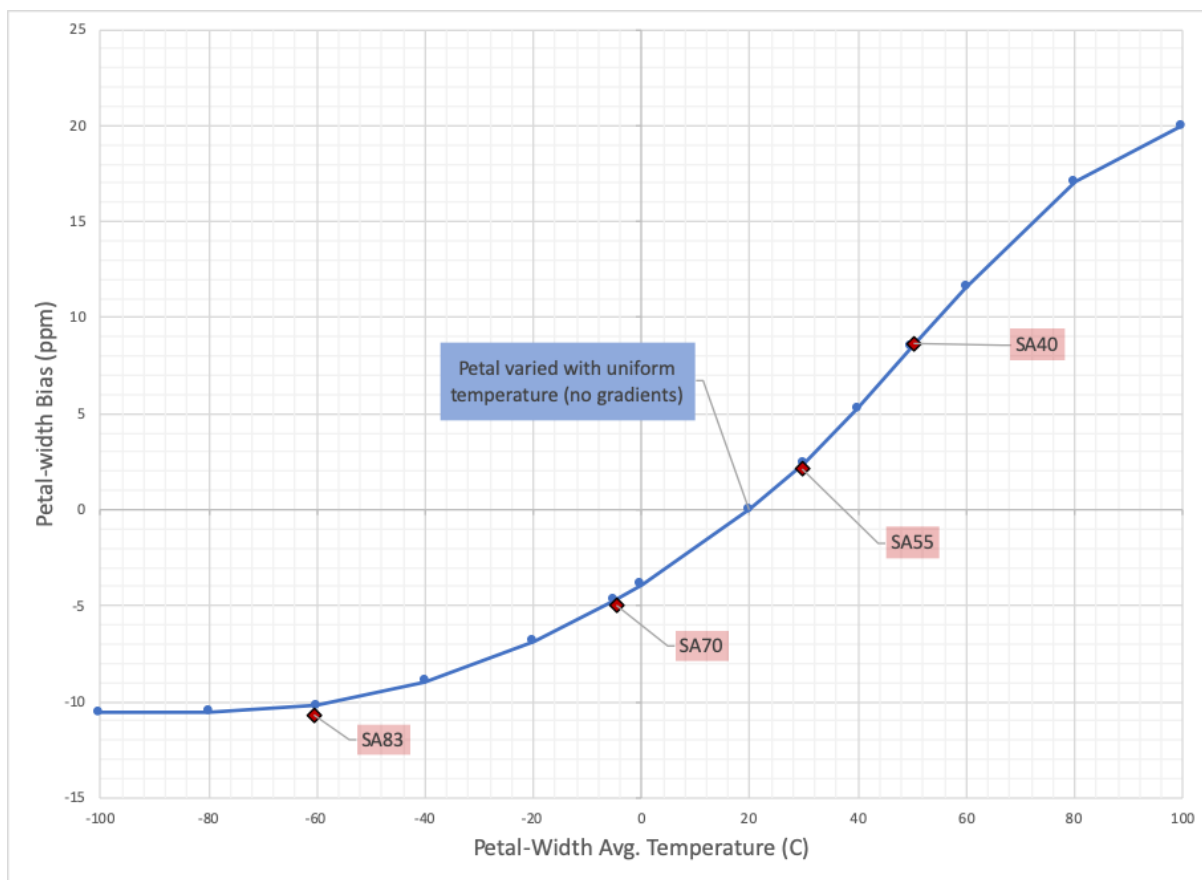


Figure 3-2. Petal-width bias of the petal for bulk temperature soak, co-plotted with the sun angle cases (plotted at the average batten temperature), shows that the sun angle cases correlate to the bulk temperature petal curve within 5%, and as such, temperature gradients are not a driver of performance.

The test temperature range was limited to that of the existing facilities, which resulted in a temperature range of -50°C to 50°C , which corresponds very well to our predicted average batten temperature range of -60°C to 50°C . The test article measurement data for each location was then compared to the test article FEM prediction at three discrete temperatures, -50°C , to -15°C and 50°C .

The relevant material properties of modulus and CTE for all materials were measured and used as inputs to the test article FEM, as well as manufactured joint geometries. Apart from as-built material properties and geometries, there were no additional inputs or adjustments made to correlate the FEM to the experimental data.

The finite element modeling technique used to construct the test article FEM was then used to model the flight petal. This flight analysis model was then used to predict performance for the on-orbit thermal environment, to which the uncertainties outlined above are added for comparison to the performance requirement.

3.2 Metrology Technique

The metrology technique for this program was displacement measuring interferometry capability of Northrup Grumman of San Diego, in collaboration with Southern Research. This technique was previously used for the JPL SWOT program.

The technique measured changes in the critical dimensions of the petal in real time using Displacement Measuring Interferometers (DMI), see Figure 3-3. A HeNe laser beam, with a doublet of wavelengths near 633nm, is injected through a beam-splitter mounted on the near end of the structural element. It is then returned by a retroreflecting corner cube mounted at the far end of the structural element. The far end return beam is mixed with the return beam from a retroreflector mounted directly atop the beam-splitter. This near-end return beam provides the stable reference length against which the far-end return beam is compared.

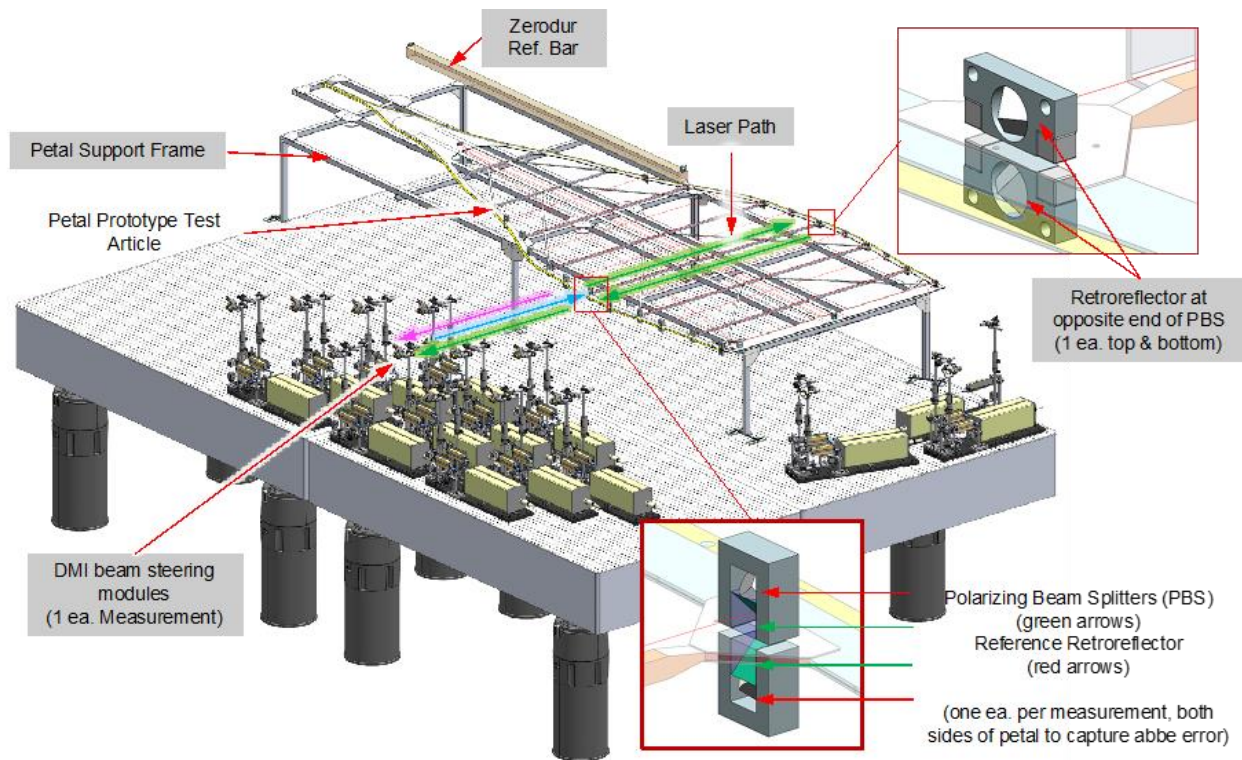


Figure 3-3. For the thermal deformation test, the petal test article was set on a low CTE CFRP frame that was pseudo-kinematically constrained to a low CTE invar optical bench (thermal enclosure not shown). The petal was pinned at the root, and free to translate in all directions. Rotation was constrained by a low friction uni-direction slide, pinned to the petal midway down its length. The remaining constraints were low friction surfaces that served to simply support the petal weight out-of-plane along the batten locations. Outside of the thermal enclosure, the lasers sources and DMI steering beams were also mounted to the invar bench, and windows in the foam thermal enclosure box, allowed the laser beams to traverse the box during the test. Northrup Grumman's metrology technique utilized DMI's between a reference retroreflector and target retroreflector on the petal to determine the change in petal dimension. A sample measurement path is outline with the blue arrow illustrating the incoming doublet frequency laser beam, the pink representing the return from the reference retroreflector and the green being of the target retroreflector.

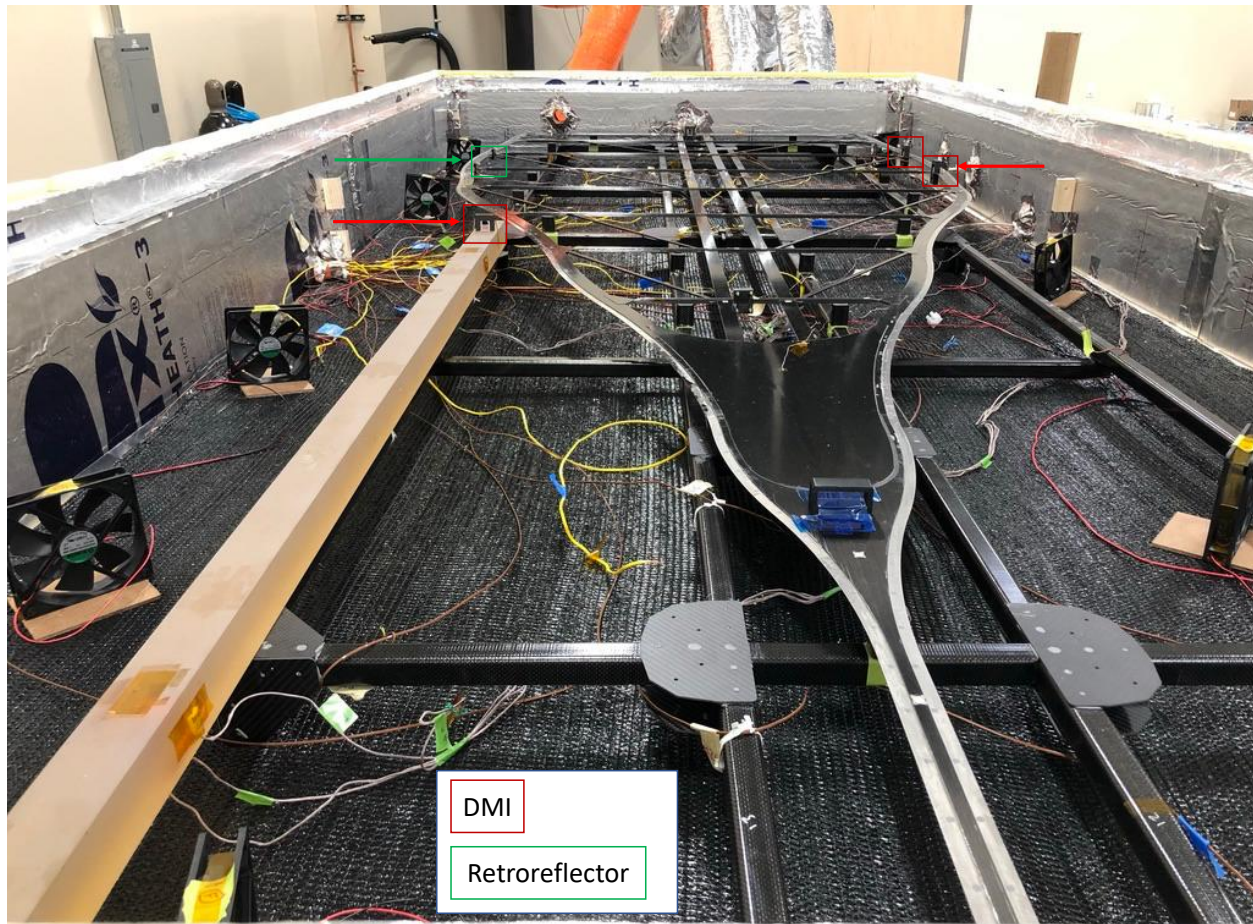


Figure 3-4. Prototype petal in thermal chamber (lid removed), being instrumented for initial proof-of-concept run of measurement accuracy. A beam splitter can be seen at the far end of the for the Zerodur reference bar, and aligned on the back wall, the measurement window. Two additional beam splitters can be seen on the right and target retroreflectors can be seen in green on the left. After the initial proof-of-concept run, the petal was outfitted with the rest of the measurement hardware.

There are several sources of error specific to our setup that must be accounted for in this measurement: atmospheric effects, Abbe error, and data losses (drop-outs). Together with the standard sources of error DMI, these form the error budget for our metrology technique. The rest of this section provides an overview of the error budget and a short description of each error source.

3.2.1 Abbe Error

Early tests showed that the petal did not stay perfectly flat during the measurement. Instead, it flexed slightly in the out-of-plane direction as the temperature was varied. To first order, out-of-plane flexure does not change the width of the petal itself. The separation between the DMI optics does change to first order, because the optics are bent towards or away from each other by the petal flexure, depending on the direction of the curvature. This apparent length change is known as Abbe error. To correct for Abbe error, DMI optics were installed on both the upper and lower surfaces of each structural element under test, and their two length changes averaged together. If the upper and lower optics have identical dimensions, their Abbe errors will be equal and opposite, and thus cancel out in the average.

3.2.2 Data Losses

DMI essentially measures length changes by counting fringes as they occur in the combined return beam. It therefore directly measures length changes only for as long as it continuously detects the return beam. If the measurement is interrupted and then restarted, DMI has no direct way of relating the measurements before and after the interruption.

When the petal temperature was below the dewpoint, water would sometimes condense on optics in the DMI beam path, keeping light from reaching the detector and causing loss of data. We injected dry gaseous nitrogen into the circulating air path of the hot/cold box to keep water vapor out of the chamber, but this proved only partially successful in preventing data losses. In addition, as warmer or cooler air was forced through the box to change its temperature, small thermal gradients in the air over the petal would at times refract the far-end beam away from perfect overlap with the near-end beam, reducing the optical interference, again causing loss of data.

We estimated the amount of petal length change during these data gaps by extrapolating the measured rate of displacement change forward from the five minutes of data preceding each gap. Displacement changes measured after the gap were ‘stitched’ to the end of the extrapolated estimate. When gaps occurred within five minutes of one another, the first gap was ‘stitched’, and the extrapolation into the second gap was estimated in part from the prior gap’s estimate.

3.2.3 Atmospheric Effect

The measurements described here were made in air, so thermorefractive effects in the atmosphere surrounding the petal contributed to the measured length change. The CFRP from which the petal is made has very low thermal expansion, and the atmospheric index change is roughly 100 times larger than the true petal strain. It was therefore necessary to monitor and correct for the atmospheric contribution to the measured length change with good precision.

The refractive index n of air is also sensitive to parameters other than temperature that also varied during the measurement. These include its pressure and relative humidity. The formula for the standard composition of air is:

$$n = \frac{N + 10^6}{10^6},$$

where

$$N = 0.3836391P \times \left[\frac{1 + 10^{-6}P(0.817 - 0.01337T)}{1 + 0.0036610T} \right] - 3.033 \times 10^{-3} \times H \times e^{0.05762T}.$$

In this formula, T is the temperature in degrees Centigrade, P is the pressure in mmHg, and H is the percent relative humidity. This formula was provided by Keysight in the technical literature for their 5517B laser which was used in this measurement, and applies at 632.8 nm.ⁱ We included pressure and RH monitors inside the hot/cold box with the petal to provide simultaneous measurements of these parameters.

The dry gaseous nitrogen we injected into the recirculating airflow displaced the room air in the hot/cold box. The refractive index formula above applies only for the standard atmospheric oxygen level. We modified the formula using the Lorenz-Lorentz equation and the known electric polarizabilities for molecular nitrogen and oxygen, the two main components of air. In the limit of

ⁱ Available at <https://literature.cdn.keysight.com/litweb/pdf/05517-90142.pdf>. This laser is now provided by Agilent.

a gas sufficiently dilute that the index of refraction n is close to 1, the Lorenz-Lorentz equation relates n of the gas to the electric polarizabilities α_i of its constituent molecules by

$$n - 1 = 2\pi(N_1\alpha_1 + N_2\alpha_2 + \dots)$$

where N_i is the density of the i^{th} molecular species. The polarizability of O_2 is 90.86% of that of N_2 , so for air at standard temperature and pressure the value of $n - 1$ of 276ppm at 632.8 nm will increase by 5.4ppm if all the O_2 is replaced with N_2 . This change in $n - 1$ is larger at lower temperatures, at which air is more dense. However, our correction assumed that the $n-1$ change at 20 C applied at all temperatures. This will be corrected in the 6B milestone; it introduces at most 1ppm strain error at the lowest temperatures we tested. The dry nitrogen did not entirely displace the room air in the hot/cold box, possibly due to leaks in the hot/cold box. We installed an oxygen monitor into the hot/cold box to measure the oxygen content directly. The oxygen sensor was unreliable for temperatures below -5°C ; for temperatures below this we assumed that the O_2 concentration equaled the last measured value at -5°C . This too will be addressed in the 6B milestone.

To verify the accuracy of the path length correction corrections, we included a 1.84 m Zerodur reference bar alongside the petal inside the hot/cold box and monitored its thermal environment similarly to that of the petal. The measured thermal deformation of the Zerodur after the corrections was within the expected range. The Zerodur data were also ‘stitched’ to correct for data gaps in the same way as the petal data. No Abbe error correction was used for the Zerodur data, because the Zerodur bar was thicker and much more rigid than the petal.

3.2.4 *Measurement Uncertainty*

The uncertainty in the measured length change depends upon many factors, including the initial length, the amount and direction of temperature change, and amount of Abbe error.

shows the estimated measurement uncertainty for the petal in the case where the Abbe rotation is 1 mrad and the petal temperature is $> -20^\circ\text{C}$. The remainder of the uncertainty tables are in Appendix C: Additional Plots & Figures, and a full copy of the NGIS metrology report is available upon request.

The table varies slightly for other temperature ranges and Abbe errors; for example, the uncertainty table for the Zerodur has no Abbe uncertainty, and for temperatures below -20°C we include an engineering estimate of 2 ppm uncertainty to account for data losses. In order to facilitate the milestone analysis, we use a conservative estimate of error, in which the largest Abbe error seen for any petal critical dimension was used to estimate error for all dimensions, and the estimated error across 1m was applied for all dimensions. This estimate is ± 1.70 microns above -20°C , and ± 2.76 microns below -20°C .

Table 3-1. Uncertainty estimate for petal thermal deformation measurements. Rows 1-3 are standard for DMI. Row 4 is differential thermal expansion between near and far optics, and rows 5-6 are differential thermal expansion of the optics relative to the petal. Row 7 is the uncertainty in Abbe error due to tolerances in optic dimensions. Rows 8-11 are uncertainties in atmospheric parameters that determine the atmospheric pathlength correction.

	Variable	Sensitivity	Coefficient	Uncertainty across 1 meter (micron)	Uncertainty across 2 meters (micron)
1	Laser wavelength	$\pm 0.067 \text{ } 2\sigma \text{ ppm/lifetime}$	path length	0.07	0.13
2	Elec Error (resolution)	$\pm 1 \text{ LSB (0.01 } \mu\text{)}$	fixed	0.01	0.01
3	Optics Non-linearity (est.)	0.0022 μ	fixed	0.00	0.00
4	BK7 Retro Reflector ϵ_T differential	7.1 ppm/ $^{\circ}\text{C}$	DT * height (est $1^{\circ}\text{C} \times 10.2\text{mm}$)	0.07	0.07
5	PBS Reference Point	0.55 ppm/ $^{\circ}\text{C}$	max D from CL (6.35mm x 70°C)	0.24	0.24
6	Invar Retro-Reflector Holder Reference Point	1.2 ppm/ $^{\circ}\text{C}$	max D from retro face 5.7mm x 70°C	0.48	0.48
7	Abbe error beam asymmetry	$[\sin\theta_x - \sin\theta_{x+\text{error}}] / 2$	0.5mm and 1000 $\mu\text{radians}$	0.25	0.25
8	Atmospheric Compensation - Relative Humidity	0.01 $\mu\text{/meter per \%RH at 620mm Hg}$	$\pm 2.5 \text{ \%RH}$	0.03	0.05
	Atmospheric Compensation - Relative Humidity	0.01 $\mu\text{/meter per \%RH at 620mm Hg}$	0.003 m	0.00	0.00
9	Atmospheric Compensation - Temperature	0.89 $\mu\text{/meter per }^{\circ}\text{C at 620mm Hg}$	1 $^{\circ}\text{C}$	0.89	1.78
	Atmospheric Compensation - Temperature	0.89 $\mu\text{/meter per }^{\circ}\text{C at 620mm Hg}$	0.003 m	0.21	0.21
10	Atmospheric Compensation - Barometric	0.36 $\mu\text{/meter per mm Hg}$	$\pm 0.225 \text{ mm Hg}$	0.81	1.62
	Atmospheric Compensation - Barometric	0.36 $\mu\text{/meter per mm Hg}$	0.003 m	0.15	0.15
11	Atmospheric Compensation - O ₂ Concentration	6ppm pure N ₂ to Air	$\pm 1\% \text{ O}_2 / 20\% \text{ O}_2 \times 6 \text{ ppm}$	0.30	0.60
			cumulative	3.51	5.60
			RSS	1.40	2.57

3.3 Petal Prototype Test Article

3.3.1 Design

The two critical parameters for petal-width performance are material properties, and the shape-critical component geometry that creates the triangular trusses of the petal in-plane shear structure. The design of the prototype petal focused on maintaining these two parameters with respect to the flight petal. Figure 3-5 details the methodology for designing prototype petal based on the full-scale flight design. The prototype petal is of medium fidelity in materials and shape critical components, but does not contain those features which do not drive petal-width bias performance, e.g. the optical shield, out-of-plane rib, and cart assemblies outlined in Section 2.1.1; milestone 6B will include these features.

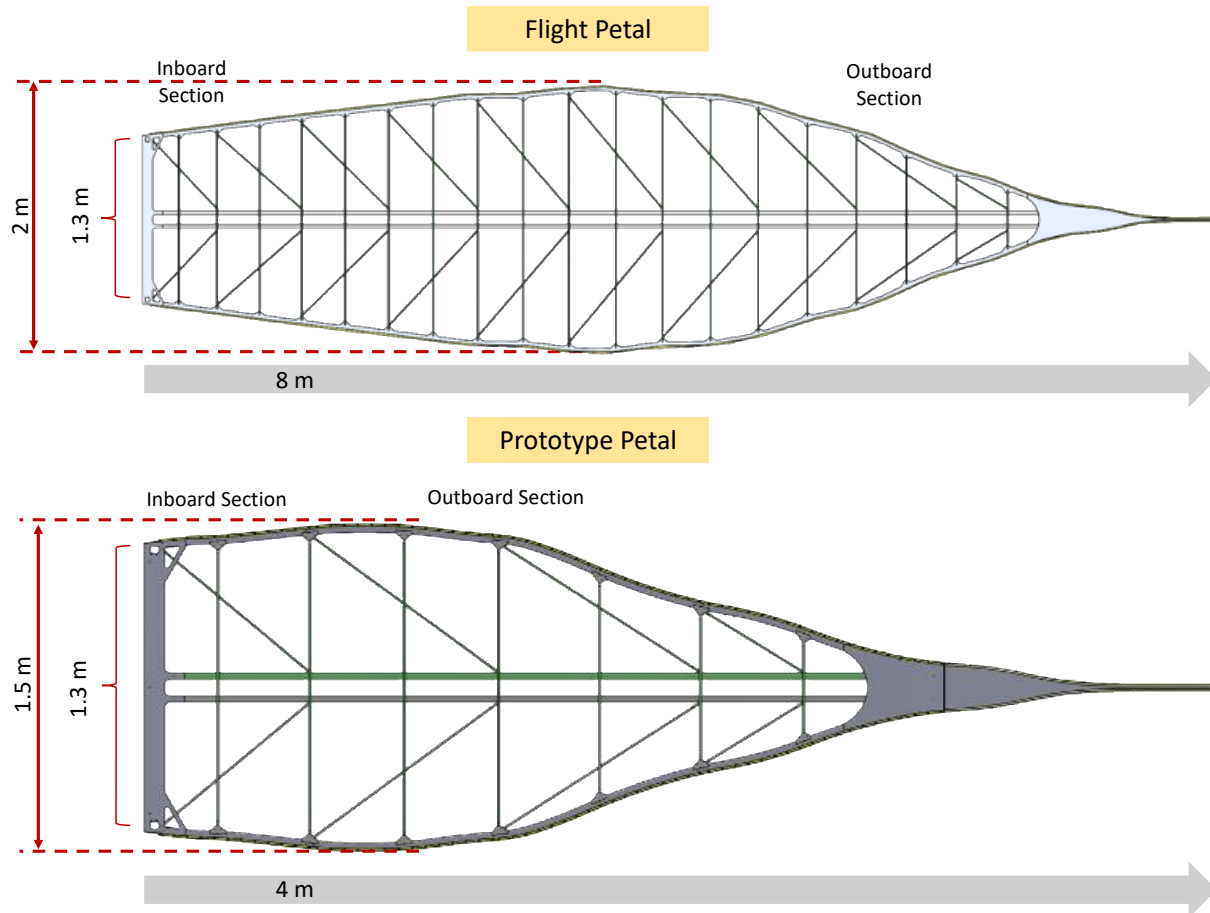


Figure 3-5. The prototype petal juxtaposed with the flight petal, showing that the prototype is a combining of the inboard and outboard sections of the flight design, and smoothed out at the transition. This allows for a fairly direct cross-correlation of the two models, as well as a general traceability of the design. The thickness of the prototype petal and the cross-section of all components were maintained.

It was important from an analytical model validation perspective to have robust traceability between the flight design and the prototype. The prototype was constrained to a max width of 1.5 m, to fit within existing Micro-Vu metrology system for milestone 5A. To maintain geometry from the flight design, and limit the petal width to 1.5 m, the inboard and outboard sections of the flight design were combined. The result was a prototype that maintained the end conditions of the flight petal at the root and tip, and also contained a large section of petal with the repeating triangular trusses that creates the structure of the petal. For model validation traceability, we also maintained the cross-sectional geometry of each component of the prototype petal to be identical to that of the flight design.

3.3.2 Manufacture

Of concern for the production of this prototype, was maintaining traceability to the flight manufacture process, such that the results of the program were wholly applicable to future programs. To that end, flight materials and manufacturing processes were used.

The components of the petal were hand-laid M55J carbon fiber laminates for the optical edge, spines, root and tip, and machine-drawn uniaxially pultruded carbon fiber-epoxy rods for the battens and braces. Flight grade EA9394 epoxy was used to room temperature bond the

components together. The assembly process was performed in a flight-like fashion, with special care taken to achieve as close to nominal geometry as possible, to mitigate these as sources of error between the as-built hardware performance and the prediction. The principle concern was offsets in hardware geometry, which could cause moments internal to the structure, and epoxy thickness in joints, because epoxy has a significant contribution to local joint thermal strain. To that end, the petal was laid out with a combination of custom manufacturing tooling, and off-the-shelf linear stages, visible in Figure 3-6. The tooling was laid out with a coordinate measuring machine (CMM) Faro Arm. The structure of the petal (before edge install), is not required to have high accuracy, and this was more than sufficiently accurate for the structural layout of the petal. The as-bonded joint thicknesses were measured at each step along the way, and recorded for use as inputs into the test article FEM, Appendix E: Adhesive Thickness Mapping.

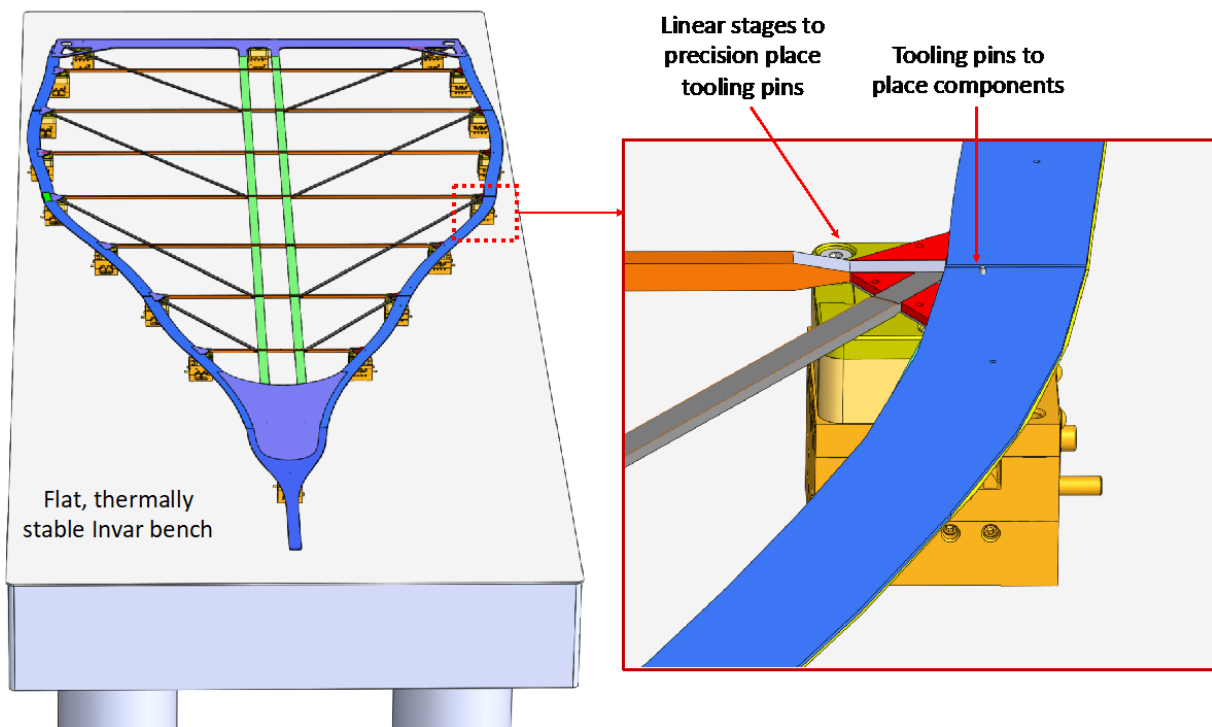


Figure 3-6. Petal manufacture was performed on optical benches, which allows for precision jiggling of the structure before epoxy bonding at room temperature. Right detail shows a linear stage used to align the pins that held the components in the correction location during bonding.

The optical edge foil was bonded to the CFRP laminate substrate in analogous fashion to that performed for milestone 3, however the edges of milestone 6A are not required to meet solar scatter requirements, and no measurements were taken. The edge segments were then bonded to the petal structure in sequential fashion from root to tip. The placement of the edges is only as accurate as the tooling, because the milestone 6A petal is not required to meet the manufacturing shape accuracy that the milestone 6B petal will demonstrate. Milestone 6A focuses on shape stability only.

Figure 3-7 shows the as-manufactured petal atop the tooling used to assemble it. The optical bench was key in providing a stiff and stable structure on which the tooling could be accurately placed. Of concern to us was ensuring the petal was flat when bonded up, and that all

the components were strain free when laid out, to minimize residual stresses in the petal after bonding the components together.

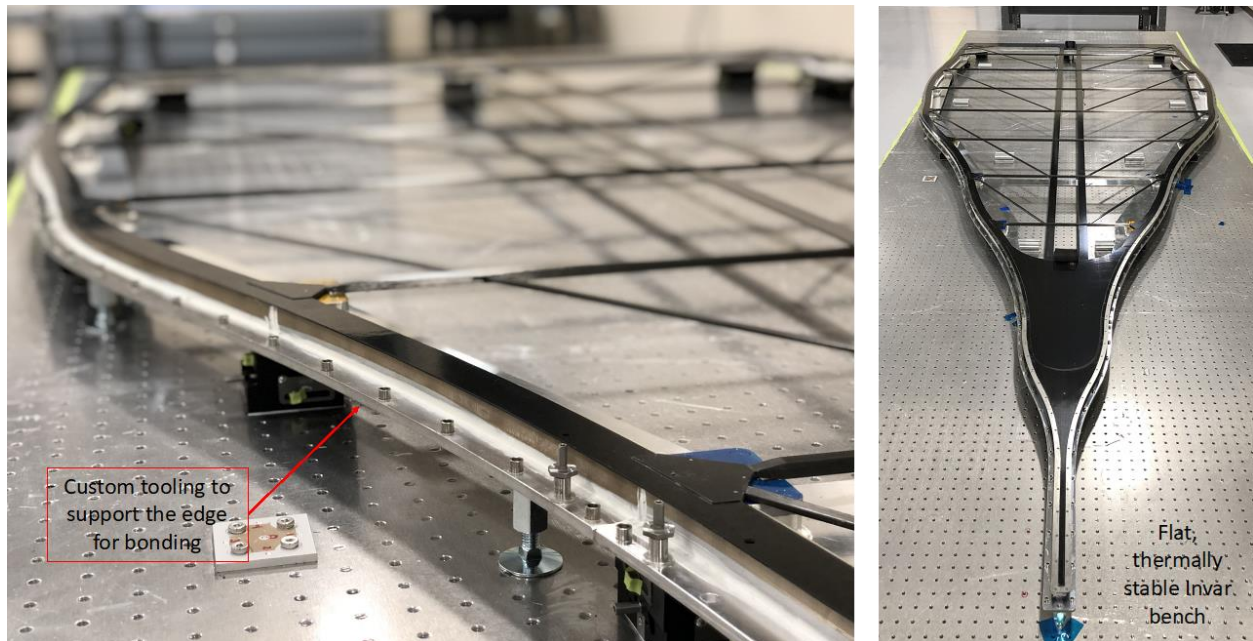


Figure 3-7. As-manufactured petal completed and sitting on manufacturing tooling that allowed precision placement of all components, and precise epoxy bonding. Left image shows petal with the telescope side down, and the optical edge is barely visible, extending only 0.5 mm beyond the CFRP edge substrate. Right image shows the petal telescope side up, with about 12mm of the edge foil showing. The CFRP structural edge is set back to prevent scattered light from reflecting off it at SA83. Aside from the edge, the remainder of the petal structure is symmetric about the midplane. The petal is sitting on precision tooling that supported the structural edge of the petal within $\sim .010''$ flatness across the structure, while the joints and edge were being bonded.

3.3.3 Analysis Model

A finite element model of the prototype petal assembly test article was built in FEMAP/NX Nastran. The model includes a high level of fidelity that maps to the as-built test hardware, the details of which are included in Figure 3-8. This model was correlated to as-measured test deflections at -50°C , -15°C , and 50°C . The FEM utilized measured values for the thermal distortion critical material properties, CTE and Young's modulus, for all materials in the assembly. Appendix D: Material Properties, contains detailed plots of the thermal strain curves used to create the CTE model inputs. Young's modulus data can be provided upon request.

A detailed model, including 3d geometry of the components, was initially built to understand sensitivities to modeling technique, e.g. component geometry, and then later simplified based on the cross-correlation results with the simplified model. Solid element breakout models were also created as needed to investigate predicted behavior before simplifying the model, e.g. a breakout model of the batten to optical edge joint was compared to the 2D representation. The batten to edge joint turned out to be critically important in properly capturing the edge behavior observed in the as-measured data, and had a significant effect on petal-width bias. The batten to optical edge joint, and its effect on thermal deformations of the petal width at the midspans is further discussed in Appendix G: Batten to Optical Edge Joint Effect on Edge Shape - Midspan Bowing. The final model version includes all physical geometry, and joint details, including individual CFRP laminate layups, and as-measured joint epoxy thicknesses.

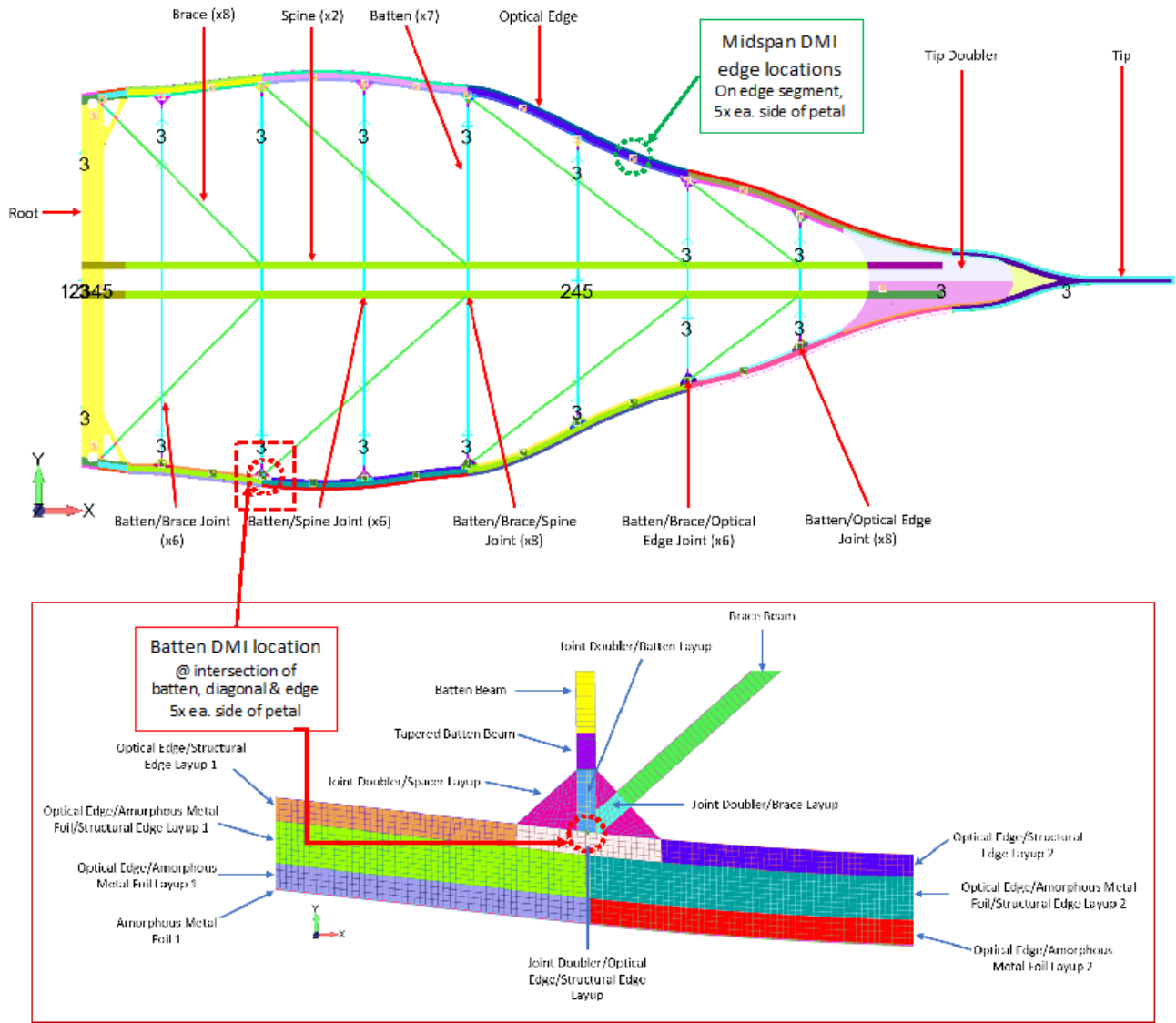


Figure 3-8: Prototype petal test article FEM includes all thermal stability critical features at a high level of fidelity. The varying element types (colors) account for the as-measured material properties for each layer of the optical edge (structural edge substrate, EA9394 adhesive, amorphous metal foil, and optical edge substrate). Detail of batten-brace-optical edge joint shows the intricacy of the model to capture behavior at critical joints. We can also see the location of the DMI for the batten measurements, which is at the deterministic intersection of the batten and brace, which should minimize the effects of any moments. We can also see the DMI at the midspan location is labeled, and it can be seen that it is less stable (softer) than the batten DMI location. Lastly, the numbers on the petal represent model constraint locations that simulate the test condition. A pin in the root (12345) is used to constrain all but rotation in-plane, which is restrained midway down the middle of the petal (245) to constraint rotation, and many (3)'s to support the thin petal out of plane.

The various components were individually modeled based on their individual properties, and each unique joint was modeled to its geometry; Figure 3-8 detailed view of the edge shows the intricacy of the modeling, with each color representing a separate laminate element, that represents the actual through thickness cross-section of the petal at that location.

Figure 3-8 also shows the boundary conditions applied to the prototype petal FEM to simulate the conditions seen by the test article. The prototype petal test article was set on a low CTE CFRP-tube frame. The frame assembly used low friction pads, upon which the petal rested, to support it in the out-of-plane direction only (in the direction of gravity). Gap elements were

used in the FEM to simulate this constraint. To rigid body constrain the petal in-plane, the test setup included two vertical pins, one in the middle of the petal root, and one approximately half-way along the length of the petal that was attached to a low friction slide on the test frame. The petal was free to expand and contract relative to the support frame.

Thermal loads were applied to the prototype petal FEM to simulate the critical temperatures that were tested using a nonlinear static solution sequence to allow the analysis to reference the CTE vs. temperature material data, as well as to allow the use of the gap elements. Three different bulk thermal load cases were applied to the prototype petal FEM: -50°C , -15°C , and 50°C . Figure 3-9 shows the results for 50°C , with the -15°C and -50°C results in Appendix C: Additional Plots & Figures. The thermal loads were applied in combination with a 1G gravity load.

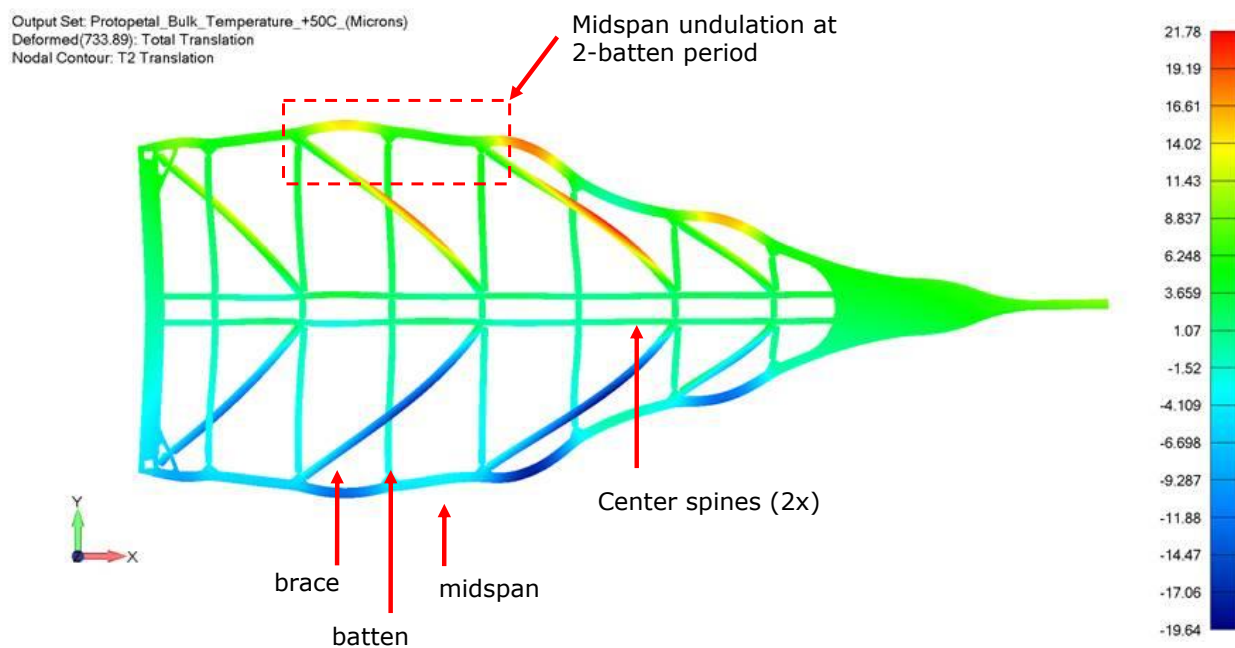


Figure 3-9. Thermally deformed FEM prediction for the test article for 50°C , scale in microns. Deformations are highly exaggerated to show the characteristic behavior of the petal test article as it thermally distorts. With respect to the requirement of petal-width bias, we note that the midspans of the petals thermally deform more than at the batten locations. The pattern follows a period of every other batten, which tracks the braces.

We find that for the thermal environment, with the as-built material properties, the batten to optical edge joint has a large effect on the midspan deformations, and ultimately the petal-width bias. For temperatures above room temperature, the midspans tend to bow outboard of the battens, and for temperatures below room temperature, the midspans tend to bow inboard of the battens. This results in an undulation along the edge, about the connection point to the battens. The pattern has a period of two battens, which logically follows from the petal structure, which has the diagonal brace that spans two battens. The initial modeling of the petal did not predict this bowing characteristic, and because the midspans tend to bow either all inboard, or all outboard, this has a substantial effect on petal-width bias, and was therefore an important characteristic of the as-built petal design to capture in the model. The effect on instrument contrast of midspan bowing, as compared to uniform petal width strain, was shown to be within the uncertainty of the petal-width bias metric described in Appendix A: Petal-Width Bias.

Future work will incorporate the effect of midspan bowing on ideal petal-width bias, which will reduce the error of future petals with respect to a new reference. It is desirable, however, to

minimize midspan bowing, because, as a general principle, the smaller the magnitude of petal-width strains, the less overall magnitude of uncertainty we will have in our prediction of the edge position due to model validation uncertainty; this effort is already underway, with some discussion in Appendix B: Designing-Out Midspan Bowing.

3.4 The Test Results Correlation to Prediction

The petal test article was measured across the entire temperature range from -50°C to 50°C , a total of four cycles, and also included a fifth hot cycle to 50°C . Measurements focused on petal width at the deterministic batten locations, as well as the midspan of the edge between the measured battens, and overall petal shape, e.g. length and shear. Of concern was the consistency (repeatability) of the measured values across the multiple measurements at each temperature, because large variations could indicate a bad measurement, or that our structure is not repeatable in its thermal deformation. Figure 3-10 plots the variation (repeatability) in measured values of the petal-width measurement locations across all thermal cycles. The measurement system had an estimated minimum uncertainty of $\pm 1.4 \mu\text{m}$ for measurements of 1 m in length, at temperatures greater than -20°C . Measurement uncertainty increased below -20°C , as well as with longer lengths. The average batten measurement path length was 1.2 m. With the exception of midspan 5, all variations fall within the uncertainty of the metrology system. Midspan 5 measurement variation only exceeds the error budget below -40°C , and is thought to be due to measurement dropouts, which were much more prevalent below that temperature. The variation in measurement for all locations, including petal length and shear, can be found in Appendix C: Additional Plots & Figures.

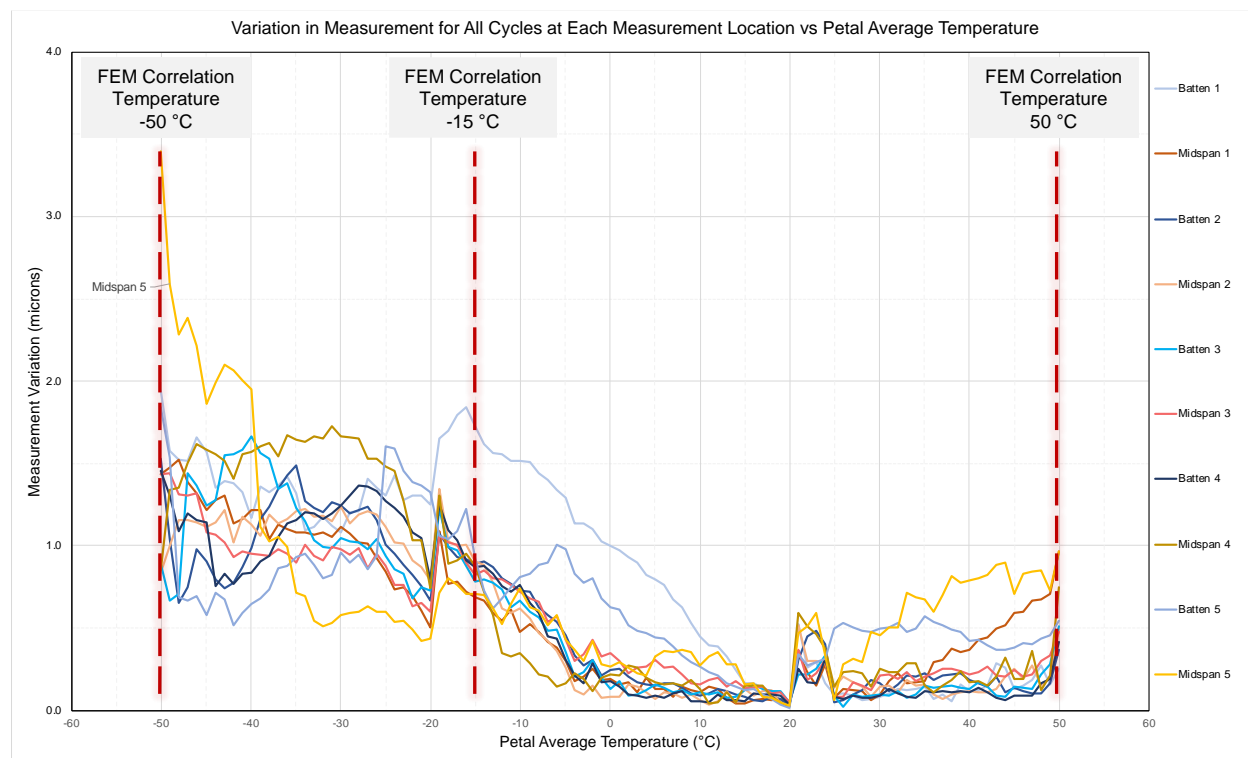


Figure 3-10. The variation in measurement values for all cycles at each of the petal width measurement locations as a function of the petal average temperature. The largest variation was midspan 5, likely because of increased dropouts below -40°C at that location. The variation in measurements between cycles falls within the system measurement uncertainty, which increased for colder temperatures, largely due to freezing of moisture in the air, which caused measurement dropouts, and because the oxygen

and other sensors used for measurement correction, became unreliable below -5°C. The batten measurement locations are plotted in the blue spectrum, and the midspans are plotted in the red spectrum; there is no identifiable difference in measurement variation cycle to cycle between midspans and batten locations. The largest source of variation was due to the dropouts at cold temperatures. The various cycles are zeroed at the reference temperature of 20°C, which causes the variation in the measurement cycle to cycle to express itself directly after passing through the reference temperature on the way up to 20°C.

The FEM was exercised at -50°C, -15°C and 50°C to predict the thermal deformation at each location for correlation to the average measurement values across all cycles. Per discussion in Section 3.1, the results of the FEM of the test article are the raw result of the as-measured material properties, nominal structure geometry, and as-measured joint adhesive thicknesses. There were no free parameters or other adjustments made to better fit the petal test article measurement data.

Section 3.1 defines our model validation criterion as:

The model must predict the petal-width bias of the prototype petal within the uncertainty of the measurement system.

To compare this, we calculate the petal-width bias for the test article, and compare it to that of the model, Table 3-2, and find that the model predicts petal-width bias across all correlation temperatures well within the uncertainty of the measurement, with no worse than a 13% difference. Note that for the purposes of comparing the petal-width bias to the measurement uncertainty, which is in microns, we have evaluated it at the average prototype petal width.

As described in section 3.1, the test article is subscale, and does not exactly match the flight design, and therefore also of interest is the correlation of specific structural features that are indicative of petal-level structural behavior, particularly those that are inputs to petal-width bias. It is important to note that the petal structure behaves as a system, with multiple elements and joints contributing to the thermal deformation response at any given measurement location. The response of a given measurement location is therefore dependent on the as-built characteristics of the local elements and joints, as well as the surrounding elements and joints. It is therefore not expected that individual measurements will agree within the measurement uncertainty, nor is it required; ultimately, the petal-width bias is the aggregate effect of these individual locations. For this reason, we compare the average response of the batten & midspan measurement locations to that of the model predictions. For reference, Figure 8-3 in Appendix C: Additional Plots & Figures, shows the correlation between the individual measurement locations for correlation temperatures, 50°C, -15°C and -50°C.

For the average value of all batten locations, which are structurally *more* deterministic, we find that the FEM prediction is within the system measurement uncertainty across all correlation temperatures, with no greater than 12% difference, Table 3-2. For the average value of all midspan locations, which are structurally *less* deterministic, we find that the FEM prediction is within the system measurement uncertainty for the extremal temperatures, -50°C, and 50°C, but deviates slightly at the interim temperature of -15°C, by 0.3 microns, or 16%. While it is preferred that all measurements, across all temperatures, fall within the measurement uncertainty, we know that performance on-orbit is driven by the extremal temperatures, and that our performance metric is robust to this small variance, as demonstrated for this temperature in Table 3-2. Additionally, it is

observed that the variances trend higher at the interim temperature of -15°C, where the strains are smaller, and the measurement uncertainty is large compared to the overall strain.

Lastly, as a check on overall structure correlation, the petal length and shear also found to agree very well with the respective model predictions, across all temperatures, at no worse than 1.7 microns, or 6%, adding confidence in our structural model validation.

Table 3-2. Test article correlation to FEM prediction for the metric of concern (petal-width bias), as well as for the batten & midspan locations. The correlation for the petal-width bias is well within the measurement system uncertainty across all temperatures, our model validation criterion. Note that for the purposes of comparing the petal-width bias to the measurement uncertainty, which is in microns, we have evaluated it at the average prototype petal width.

Measurement	FEM Model Correlation to Test Data					Measurement Uncertainty
	Temperature	Measured Value	FEM Prediction	Delta (Measured - FEM)		
	°C	Microns	Microns	Microns	% diff	
Petal Width Bias (PWB)	+50	14.0	12.9	1.1	8%	+/- 1.80
Battens (avg)		9.9	9.3	0.6	6%	
Midspans (avg)		18.1	16.5	1.6	9%	
Petal Width Bias (PWB)	-15	-11.5	-10.0	-1.5	13%	+/- 1.80
Battens (avg)		-7.0	-6.2	-0.9	12%	
Midspans (avg)		-15.9	-13.8	-2.1	13%	
Petal Width Bias (PWB)	-50	-18.1	-16.5	-1.6	9%	+/- 3.00
Battens (avg)		-9.4	-8.6	-0.7	8%	
Midspans (avg)		-26.8	-24.4	-2.4	9%	

4 Flight Design Validated Analysis Model & On-orbit Performance

4.1 Approach

The validated flight analysis model is used to predict petal-width bias for the thermal environment (sun angle), which is used to compare to the milestone requirement, after the addition of the measurement, scaling and petal-width bias metric uncertainties. To that end, the flight analysis FEM was built with the same techniques as the test article FEM, utilizing the same material properties. The flight petal model was then cross-correlated with the prototype, for the prototype test temperatures of -50°C , -15°C and 50°C , to verify the flight petal model behaved as expected, Section 4.3. Lastly, the flight model was then used to predict the petal-width bias for the on-orbit environments. The following sections describes the details of this process and the results.

4.2 Analysis Model

A finite element model of the flight Starshade design was built in FEMAP / NX Nastran, Figure 4-1. The key thermal distortion members of the model (petal, truss longerons and truss nodes) used representative element geometry and material properties to match the as-built prototypes, and most importantly, we use the measured thermal strain as a function of temperature.

Nodal temperatures were mapped for the sun angle cases run on the thermal analysis model, section 2.2. The thermal distortion analysis uses a nonlinear solver to take into account the non-linear nature of CTE and modulus material properties. The non-linear solution applies the nodal temperatures, and uses the appropriate CTE and modulus vs. temperature lookup tables to produce thermal strain, which is the result we compare to the milestone.

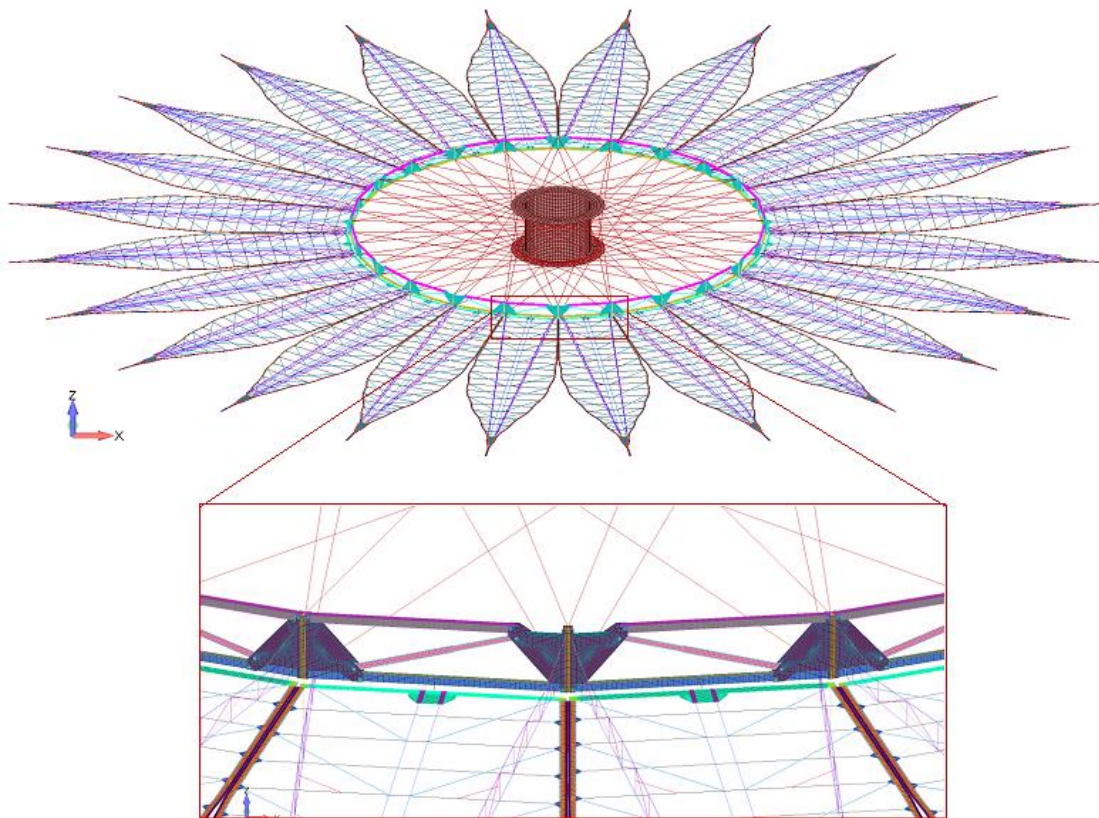


Figure 4-1: Flight design analytical model w/ detail of truss-bay – petal interface

4.2.1 Petal Subsystem

The petal structure assembly is comprised of the battens, braces, spine, optical edge, root, and tip, which are the same components discussed in Section 3.3.3, but with the addition of a pop-up rib. The rib was not represented in the prototype petal for milestone 6A, but will be present for 6B. The flight petal components were modeled using the same methodology as discussed in Section 3.3.3, which provides confidence that the FEM is accurately representing the flight petal structure.

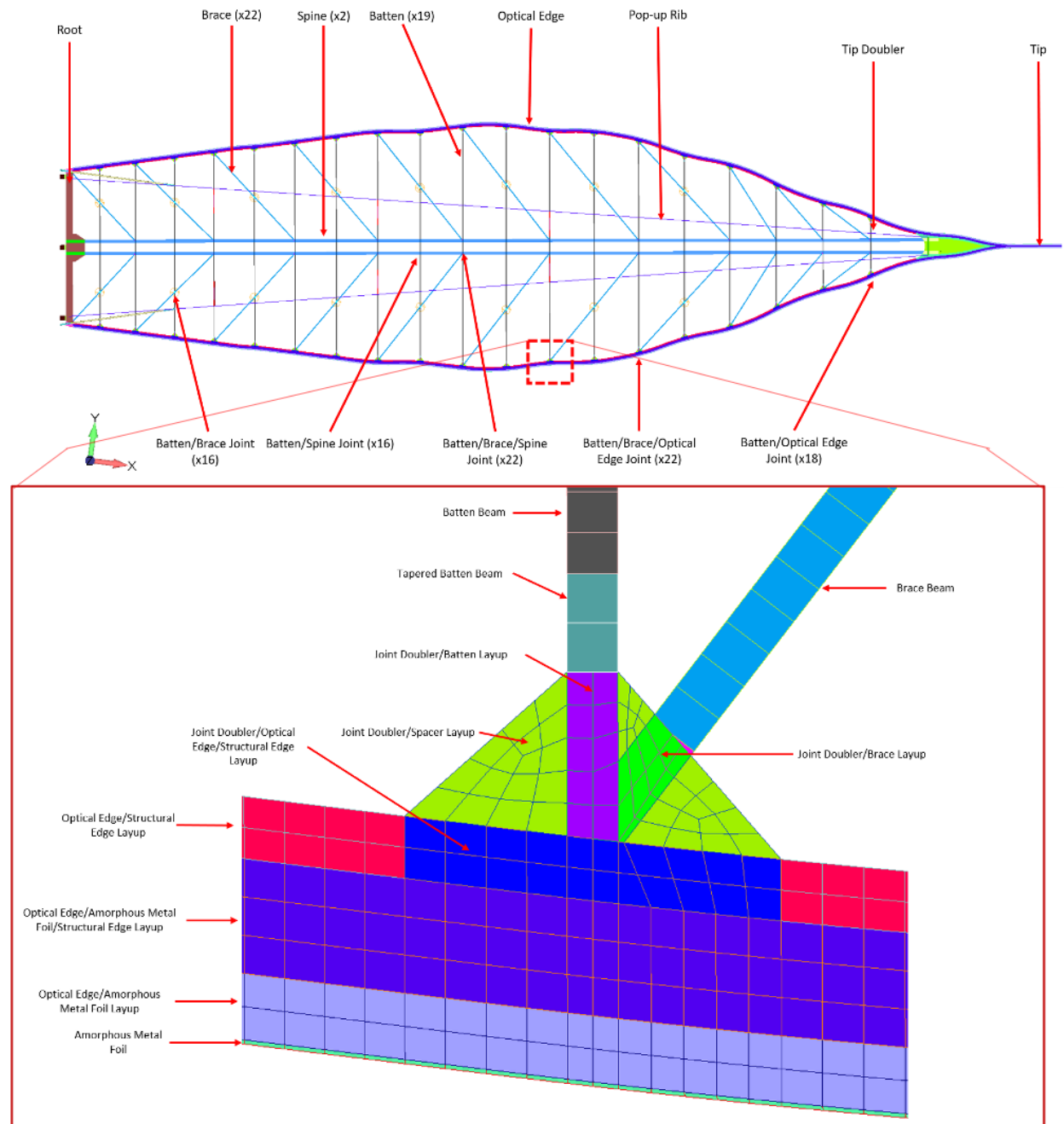


Figure 4-2. Flight petal subsystem analytical model includes all flight structural components that contribute to thermal strain and is constructed in the exact same fashion as the fine prototype test article FEM.

Figure 4-2 shows the flight petal FEM, including a detail of the batten-brace-optical edge joint, which is important for thermal distortion performance. The figure shows that the modeling technique remains consistent with the method presented in Section 3.3.3.

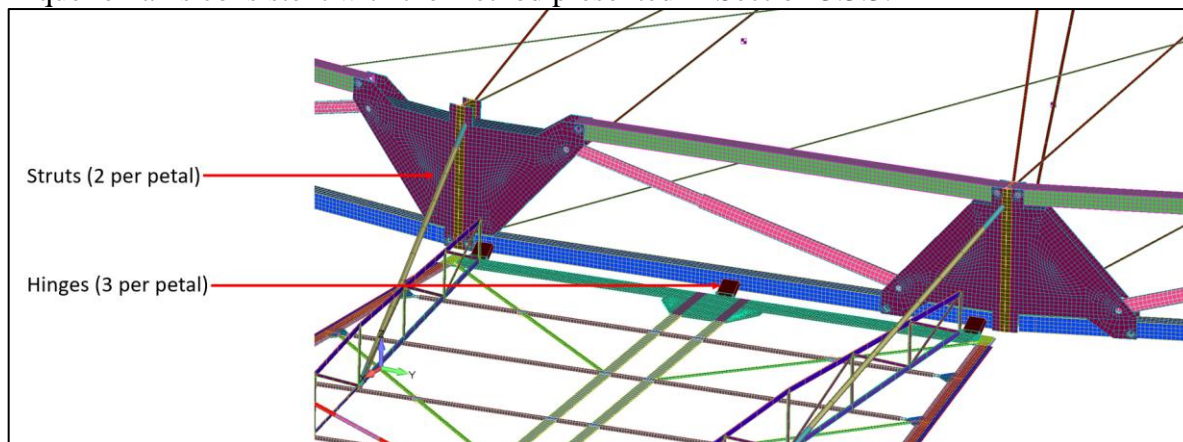


Figure 4-3. Detailed view of the connection of the flight petal to the inner disk truss-bay FEM from milestone 8A. Longerons, shorterons, and diagonals are free to rotate about their hinge axes, more on inner disk detail are available in milestone 8A.

Figure 4-3 illustrates that each petal is hinged at three locations to the longeron, represented by beam elements, and allows rotation about the root of the petal; the center hinge constrains the petal tangentially. The petal is held in-plane with two struts up to the truss bay. These boundary conditions minimize over-constraining the petal and keep the petal in the starshade plane.

4.3 Flight Design FEM Correlation to Prototype FEM

A correlation between the flight petal FEM and the test article FEM was performed to demonstrate that the flight model behavior was as-expected based on the test article performance; this was performed for the test article environments of -50°C , -15°C and $+50^{\circ}\text{C}$. The test article petal was specifically designed to capture the key geometry of the flight petal, which was accomplished by matching the inboard and outboard sections of the flight design, then smoothing out the ‘seam’, per discussion in Section 3.3.1. This allowed the flight petal FEM to be correlated to the test article FEM at the structurally equivalent locations.

Figure 4-4 shows the petal thermal strain correlation for the upper temperature limits of the test article thermal test environment of 50°C bulk temperature soak, where the geometry of the test article petal is shown at the bottom of the plot, and the data for the flight petal is overlaid at the locations that match to the test article. The blue and red dots represent the thermal strain in ppm of the test article FEM for flight and prototype, respectively, where perfect correlation would be represented by all dots perfectly inside of the hollow square. That said, we do not expect the flight FEM to exactly match the test article prediction, because the flight design geometry we are matching to the test article is part of an overall larger structure, and the test article is sections of that larger petal that have been joined together. The correlations for -15°C and -50°C are in Appendix C: Additional Plots & Figures.

The results show that the flight FEM correlates very well to the test article at the batten locations, with a difference in the *average* strain of the battens being within 7% across all correlation temperatures. The average strain of the relevant midspan locations is within 11% across all correlation temperatures. The tighter correlation at the battens is to be expected, because they are structurally more deterministic, whereas the midspans are structurally softer, so their behavior

will depend more on their boundary conditions, which differ between flight and test petal. Importantly the overall trends and behavior between prototype and flight petals is consistent. Overall, correlation between the flight FEM and test article FEM is considered very good, and no further work was considered necessary to utilize the flight FEM for on-orbit performance prediction.

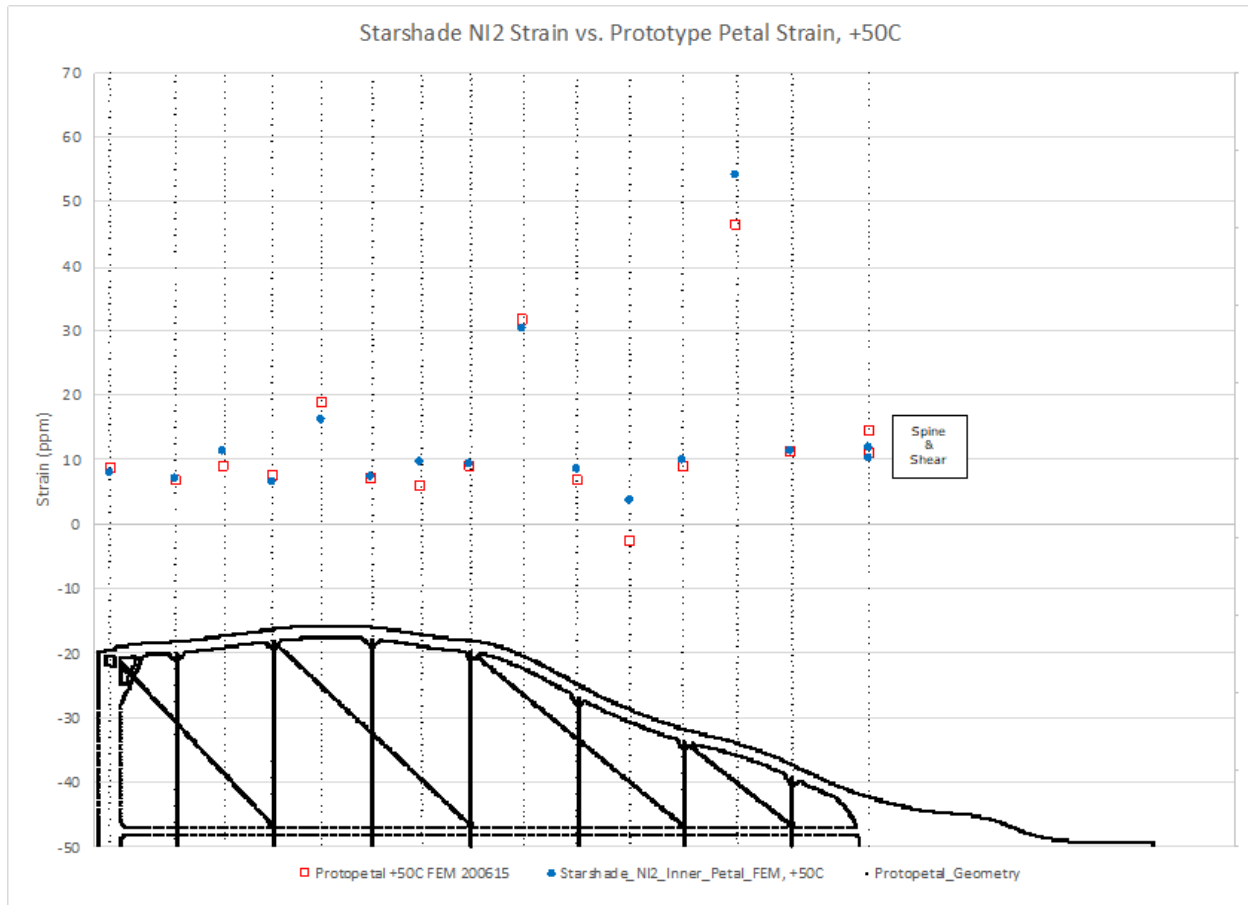


Figure 4-4: Correlation between validated prototype petal and flight petal for -50°C . The y-axis is in thermal strain (ppm) and the petal geometry is along the x-axis, and vertical dashed grey lines align the geometry. The prototype petal measurements are red boxes, while the flight petal are blue dots. The petal length and shear measurement are individually labeled, and align with the measurement location at the tip of the petal. The flight petal is modeled with the same techniques and material properties; however, we crosscheck the flight model response at the prototype petal test temperatures to verify that the flight petal FEM response is similar in behavior and magnitude. The first two battens and midspans from the inboard section of the petal are matched to the corresponding flight geometry, and the remainder of the battens and midspans are matched to the outboard section of the petal, from which the tip of the prototype petal was designed, per Section 3.3.1. The correlation is not expected to be an exact because the overall geometry of the two petals is different, however we find that the results are both similar in behavior and magnitude and consider the flight petal geometry to be accurately modeling the behavior of the test article.

4.4 On-Orbit Performance Predictions

The validated flight analysis model can now be used to make a prediction of the effective petal-width strain for the on-orbit thermal environment, Figure 4-5. The petal-width bias of the flight-design validated FEM is coplotted with the ideal petal-width bias, determined from the preliminary breakout FEM of the petal, Figure 2-8. The petal width bias error is the difference between the prediction and the ideal, which is discussed in Section 5.

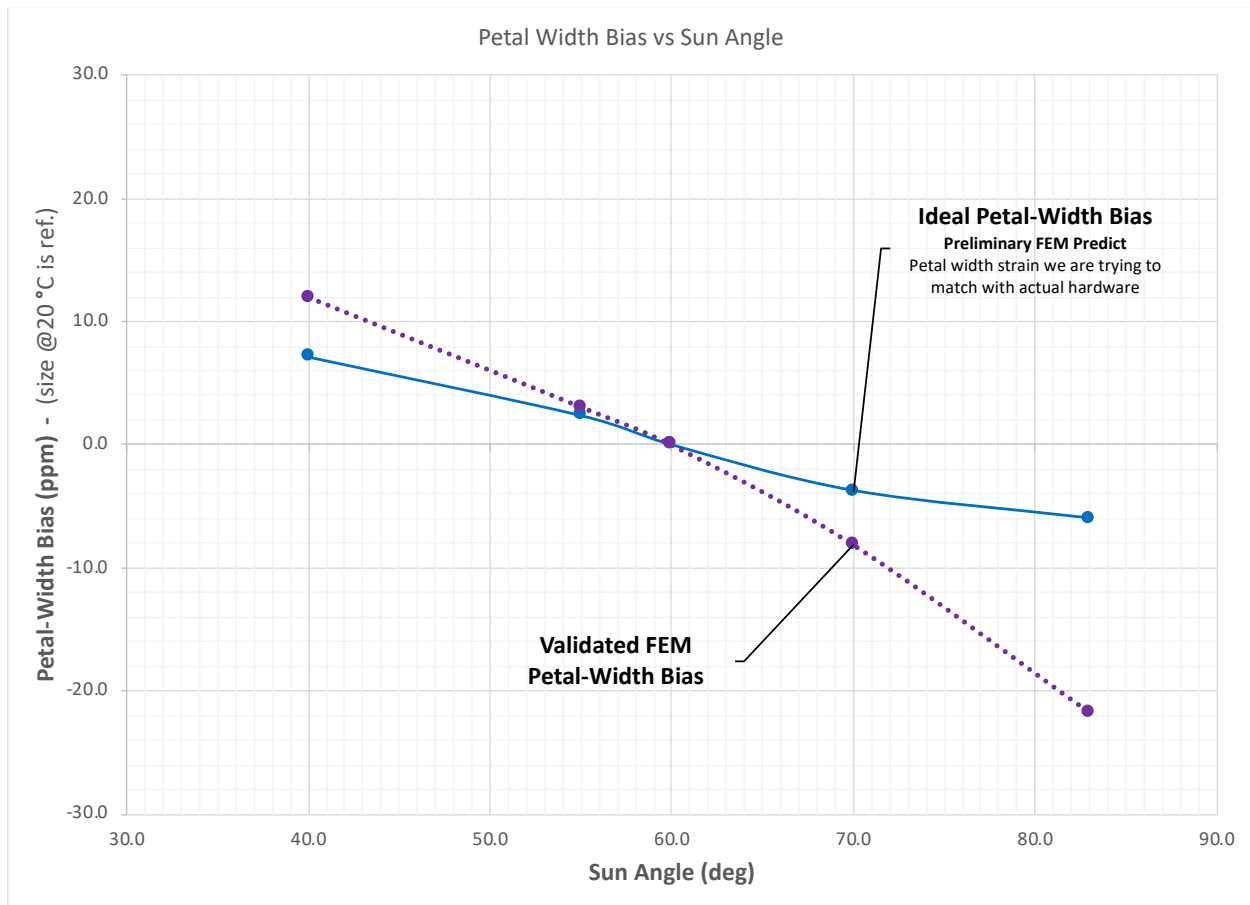


Figure 4-5. Validated flight analysis model prediction of the petal-width bias, co-plotted with the ideal petal-width bias that was determined at the beginning of the program. The petal-width bias error is the difference between the two. The bias for the on-orbit observational sun angle range of 40 to 83 degrees, is with respect to a 20°C reference temperature, which occurs at ~SA60.

The petal-width bias for the worst-case performance prediction from Section 2.4 is presented in Figure 4-6 alongside the nominal on-orbit results. When considering the performance at the extremal conditions (sun angles), we find that the $\pm 10^\circ\text{C}$ temperature uncertainty has a larger effect on petal-width bias than the 3-sigma material property variation. This logically follows from Figure 2-9, because the slope of the thermal strain curve is steeper above the reference temperature (the battens are above the reference temperature for sun angles SA40 and SA55).

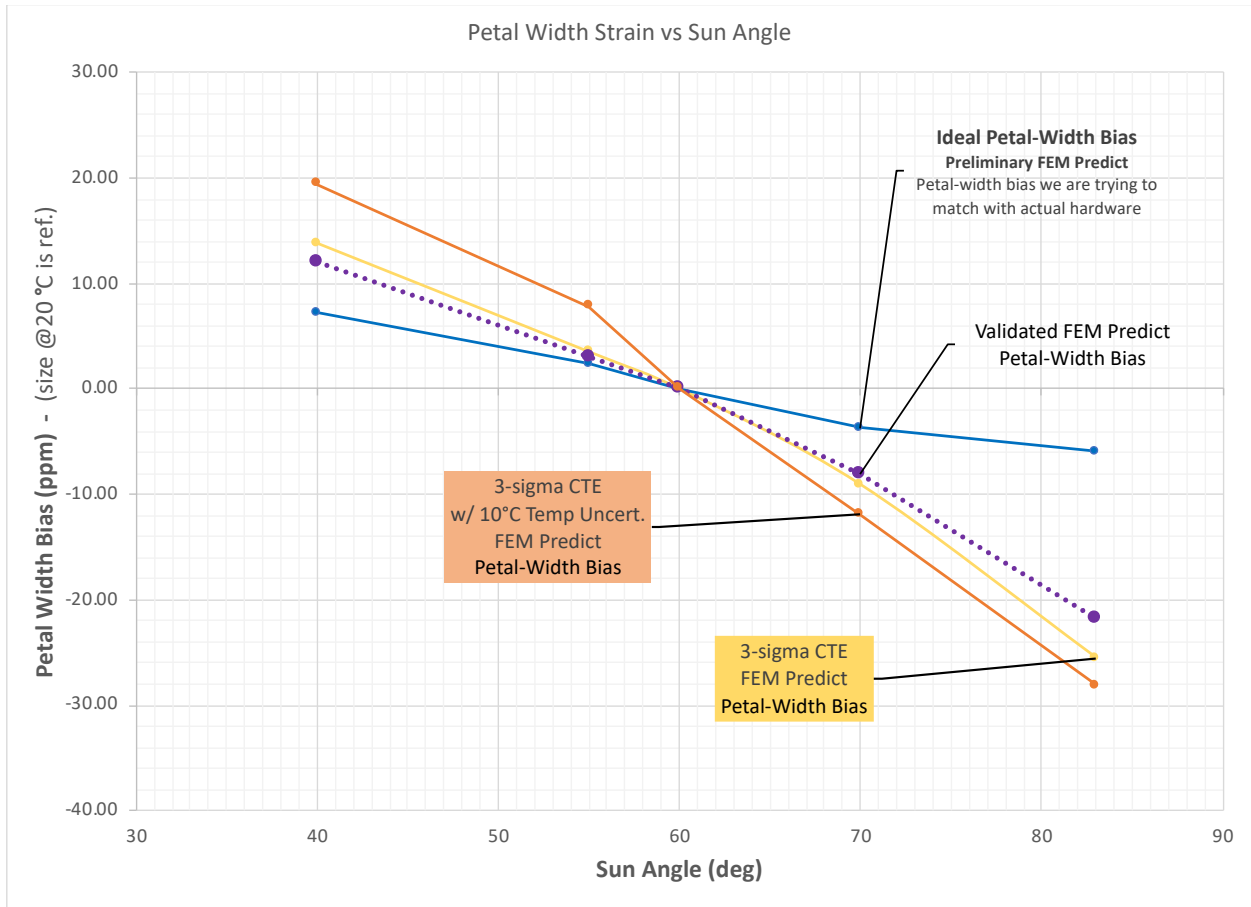


Figure 4-6. Petal-width bias of the nominal validated FEM case, the 3-sigma CTE case, and the worst case of 3-sigma CTE with a $\pm 10^\circ\text{C}$ temperature uncertainty. The worst-case performance prediction assumes the material properties are biased toward higher thermal strain (in absolute value), and temperature is driven 10°C hotter at SA40, and 10°C colder for SA83.

5 Milestone Analysis & Conclusions

Milestone 6A requires demonstration of on-orbit thermal stability of the global petal-width bias to within ± 25 ppm of the ideal petal-width bias, by analysis, using a validated model of critical dimension vs. temperature. This specification applies as the difference between the petal-width bias of the validated FEM and the ideal petal-width, for a given on-orbit thermal environment. In showing that this requirement can be met for all petals, and not just their mean, per discussion in Section 1, the random petal-width bias error requirement is also met.

5.1 Petal-Width Bias Error

In order to compare the validated FEM prediction to the milestone, the ideal petal-width bias is first subtracted from the validated FEM prediction of petal-width bias, to get the *error* in petal-width bias. The result is plotted in Figure 5-1 as the petal-width bias error in parts per million (strain) versus sun angle in degrees. The uncertainties in the FEM prediction discussed in Section 3.1 are also plotted with respect to the validated FEM prediction. The resulting petal-width bias error, including the associated uncertainties, can now be directly compared to milestone requirement of ± 25 ppm.

We find, as expected, that the largest errors (with uncertainty) of ± 13.3 ppm are at the extremal sun angles of 40 and 83 degrees. SA40 and SA83 are equally driving cases because the petals are shimmed to center the error. This results in an allowable growth of 88% against the ± 25 ppm requirement.

The validated FEM width-bias error in Figure 5-1 is purposefully centered on the requirement to create equal margin either side of the uncertainty, as will be performed in a flight program. In the flight program, material properties of the constituent materials will be extensively sampled for CTE, and a sufficient number of petals will be characterized to validate the finite element model of thermal distortion. This will lead to a similar characterization of the offset in the bias error that centers the petals on the remaining margin by physically shimming the interfaces between the petal and truss, as was performed in milestone 7C. The amount by which the bias error is to be centered, is the value to which we would shim the petal with respect to the truss, and becomes the nominal value to which milestone 7C shims. Note that the accuracy in shimming is accounted for under milestone 7C.

The error is driven by the aforementioned midspan bowing that did not manifest in the preliminary petal-width analysis model, because only a cross-section of the petal was analyzed. This was the reference, ideal petal-width bias, by which the error is assessed, per discussion in Section 3.3.3. Future iterations will include, and minimize, midspan bowing, establishing a new ideal petal-width bias, and minimizing error.

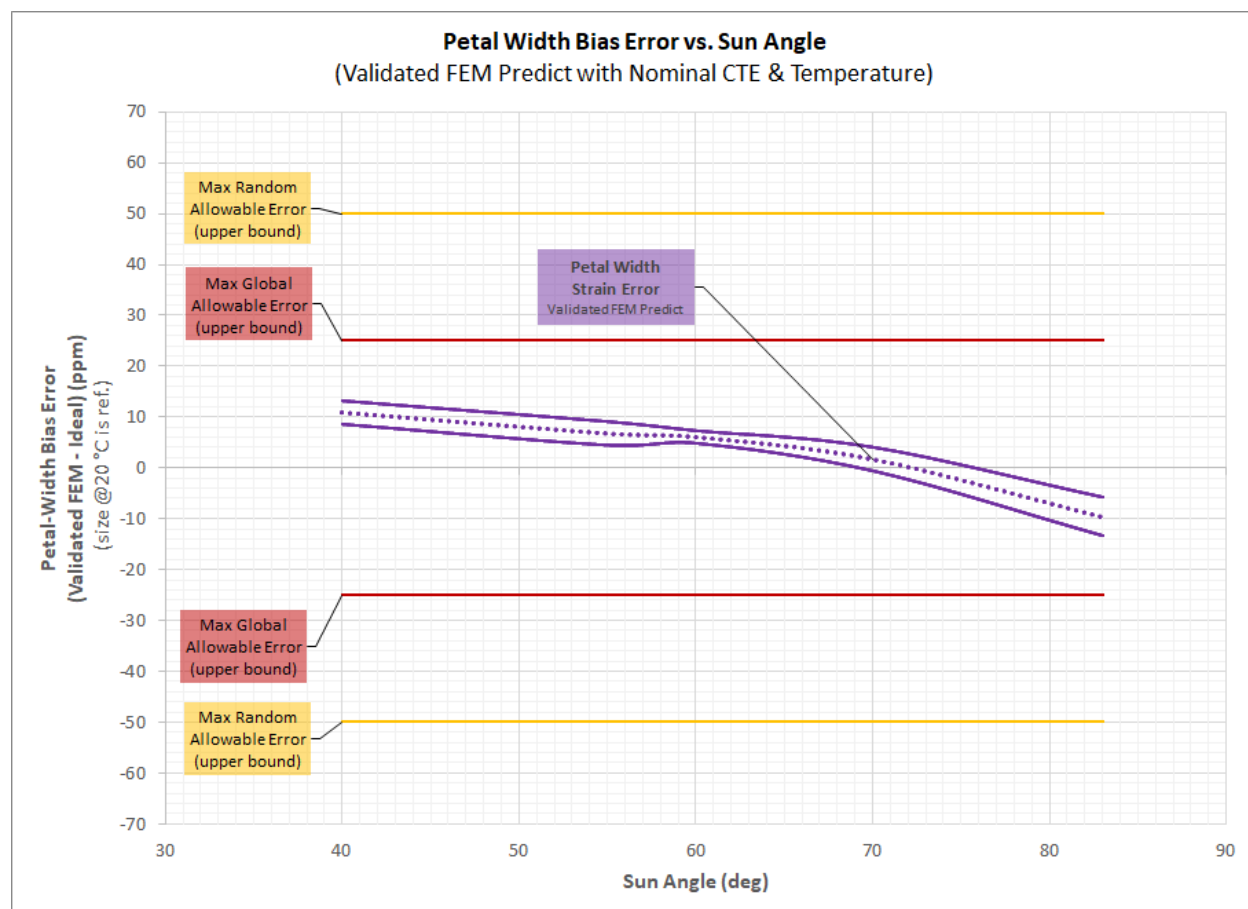


Figure 5-1. The petal-width bias error of the validated FEM from the ideal is plotted in ppm on the y-axis as a function of sun angle in degrees for the on-orbit thermal environment. The ideal petal-width bias error, by definition, is at $y = 0$ for all sun angles, which would represent an error of 0 ppm from the ideal petal-width. The validated flight design analysis model prediction is coplotted with the model, scaling and petal-width bias uncertainty. This can now be compared to the overall requirement of ± 25 ppm. Note that the model uncertainty is always zero at the reference temperature, 20°C , which occurs at SA60, however the petal-width bias metric error is always non-zero. Petal-width bias error is adjusted to center the bias per discussion in body of text.

Figure 5-2 includes 3-sigma CTE bounds and a $\pm 10^{\circ}\text{C}$ temperature uncertainty. We find, as expected, that the maximum width-bias error is still at the extremal sun angles of 40 and 83 degrees. The margin against the requirement is smallest at SA40, and is 6.7 ppm (18.3 ppm maximum expected vs 25 ppm allowable), or 27% allowable growth, which we evaluate as satisfactory for a worst-case performance prediction. Note the margin at SA83 is 10.8 ppm (-14.2 ppm expected vs -25 ppm allowable), or 76% allowable growth. Also note that the same bias error shift is used here as in the nominal results. While the effect of as-built material properties can and will be adjusted for, the temperature uncertainty portion of the error cannot; we conservatively do not apply any shimming for the portion attributed by the material properties in our worst-case performance assessment.

Note that this performance assessment assumes all petals have a petal-width bias at the 3-sigma extreme, and assumes a systematic temperature bias of the starshade at the maximum value, a very conservative assumption. In practice, only a few petals would be at the extremes, and those individual petals would be compared to the ± 50 ppm, and the mean of the 24 petal biases would be compared to the ± 25 ppm requirement. Nonetheless, with worst-case condition assessed in this fashion, we show margin against the conservatively assessed requirement.

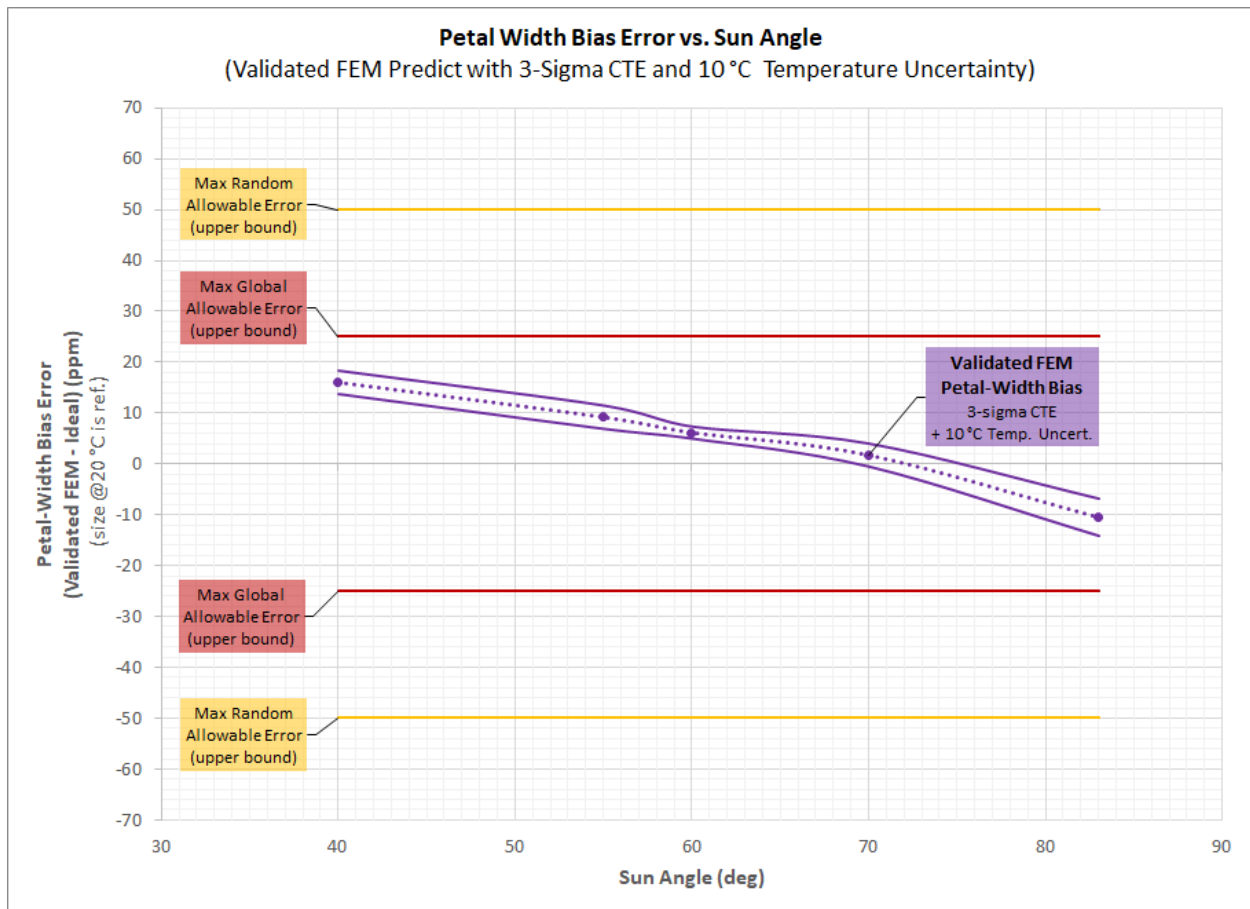


Figure 5-2. The predicted petal width bias error for the worst case of 3-sigma CTE variation combined with $\pm 10^\circ\text{C}$ temperature uncertainty applied in the worst-case direction. The validated flight design analysis model prediction is coplotted with the model, scaling and petal-width bias uncertainty. It can then be compared to the overall global requirement of ± 25 ppm.

5.2 Instrument Contrast Results

Since the quantity of interest is ultimately the thermally deformed starshade optical performance, an optical model is used to evaluate the change in contrast resulting from the validated FEM prediction of the on-orbit, thermally distorted starshade. Contrast is evaluated at the longest wavelength within the starshade bandpass, in this case 552 nm. We do this for the thermally deformed petals that have been placed at the ideal disk radius from milestone 8A. We then also evaluate the thermally deformed petals at the actual disk radius that was predicted by the validated FEM from milestone 8A, which used longeron and truss node measurement data. Additionally, we evaluate the petals for the worst-case performance condition of 3-sigma material properties with a 10°C temperature uncertainty, again, at both the ideal and actual disk radii. Important to note, all cases are FEM predictions, and do not include model or measurement uncertainty. For these cases, we do *not* assume shimming out the bias, as described Section 5.1 in the report, which is conservative, and results in a worse performance (higher delta contrast).

Figure 5-3 shows a side-by-side of the thermal distortion quiver plot for the driving on-orbit thermal environment of SA83, along with the resulting change in instrument contrast for both cases, which is listed in the titles. The left plot is evaluated at the ideal disk from milestone 8A,

and the right plot is evaluated at the actual disk from milestone 8A. We find, as expected, the effect on instrument contrast for the ideal disk case is less than that of the actual disk.

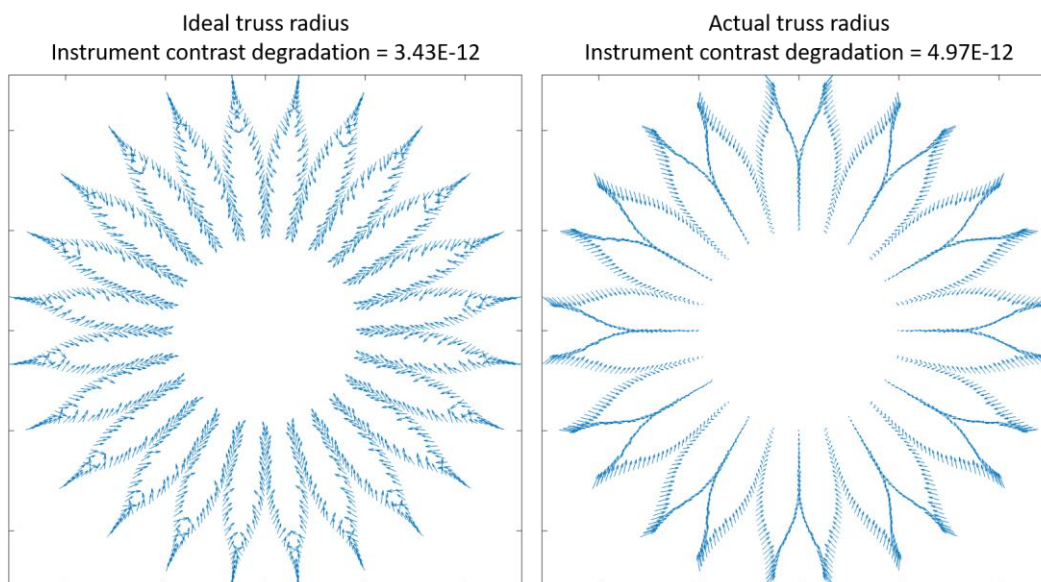


Figure 5-3. Nominal CTE and temperature cases - Thermal distortion quiver plots for the performance driving on-orbit thermal environment of sun angle 83 degrees, with the disk at the ideal thermally distorted radius (upper left), and with the actual disk radius from the milestone 8A FEM prediction for the environment (upper right). Quivers are at different scales for each thermally deformed starshade. The starshade quiver plots are dominated by petal position bias, and we can see that the actual truss rotates the petals in pairs, which is expected based on the pair-wise nature of the perimeter truss bays that comprise the inner disk. The petal rotations have little effect on instrument contrast; however, the rotations dominate the width-wise vector of the quiver plot; this is because the tangential motion is much larger than the petal-width distortions.

Table 5-1 and Table 5-2 present the change in instrument contrast due to the thermally deformed petals for all on-orbit cases we analyzed, varying between nominal and worst-case conditions, and ideal and actual truss radius. A reminder that the FEM predictions do *not* include model correlation, measurement, or width-bias uncertainties, they are simply the results of the validated model. We find, as expected, that the worst-case condition for SA83 at the *actual* truss radius creates the largest delta contrast.

For both the ideal (Table 5-1) and the actual (Table 5-2) truss radius cases, the contrast degradations are less than the corresponding allocations. For the ideal truss radius cases (Table 5-1), the contrast degradation is due to thermoelastic deformation of the petals alone, and so the corresponding contrast allocation is 8.0E-12 for KPP6. For the actual truss radius cases (Table 5-2), the thermoelastic deformation of both the truss and the petals contributes contrast degradation, so the performance must be compared against the sum of the allocations towards KPP6 and KPP8, which is 9.0E-12. In both the ideal and the actual truss radius cases, the contrast allocations are met, with margin.

Table 5-1: Instrument contrast degradation at sun angles 40° and 83°, using FEM-predicted thermal petal width changes, and assuming ideal inner disk performance. As such, these contrast degradations are due to the petals alone, and ought to be compared to the total KPP6 contrast allocation, which is 8.0E-12. The nominal cases use expected material properties and temperatures, and the worst cases use material CTEs at the 3 σ level and a 10°C temperature uncertainty (+10°C for the hot case, -10°C for the cold case). The petal-width bias error is the difference between the predicted petal width bias and the assumed ideal inner disk radial bias. Note that in these cases, we do not take advantage of the ability to shim the petals to the optimal radial position, as we do in Section 5.1, and as such the petal-width bias errors and associated contrast degradations are larger. (At the maximum petal-width bias error from Section 5.1 of 18.3 ppm – at SA40 worst-case – we expect 3.37E-12 contrast degradation due to petal-width bias alone.) Despite this conservatism, the contrast degradation is below the allocation of 8.0E-12.

Sun Angle (degrees)	Case	Petal-Width Bias Error (ppm)	Instrument Contrast Degradation ($\times 10^{-12}$)
40	Nominal	4.9	0.41
	Worst Case	12.0	1.79
83	Nominal	-16.7	3.43
	Worst Case	-22.5	6.06

Table 5-2: Instrument contrast degradation at sun angles 40° and 83°, using FEM-predicted thermal deformations for both the inner disk and the petals. As such, the contrast degradation ought to be compared to the combined contrast allocations for KPP6 and KPP8, which is 9.0E-12. The nominal cases use expected material properties and temperatures, and the worst cases use material CTEs at the 3 σ level and a 10°C temperature uncertainty (+10°C for the hot case, -10°C for the cold case). The petal-disk differential strain is the difference between the predicted petal width bias and the inner disk radial bias. Since the thermal deformations of the inner disk are close to the ideal performance for sun angle 40°, there is not much difference between the ideal (Table 5-1) and FEM-predicted performance for that sun angle. Note that in these cases, we do not take advantage of the ability to shim the petals to the optimal radial position, as we do in Section 5.1, and as such associated contrast degradations is larger. Despite this conservatism, the contrast degradation is below the allocation of 9.0E-12.

Sun Angle (degrees)	Case	Petal-Disk Differential Strain (ppm)	Instrument Contrast Degradation ($\times 10^{-12}$)
40	Nominal	4.4	0.34
	Worst Case	12.0	1.63
83	Nominal	-21.4	4.97
	Worst Case	-27.5	8.23

5.3 Concluding Statement on Performance

This report detailed the S5 efforts to verify petal on-orbit thermal stability performance by analysis using a validated model. In doing this, we attempted to be conservative, so that our results would be robust against the requirement. The conservatism was threefold.

Firstly, because we only built and validated one prototype petal, we conservatively set out to satisfy the tighter global requirement of ± 25 ppm as if it applied to each petal individually, when in fact it is only the *mean* petal-width bias of the 24 flight petals that will ultimately be assessed against that requirement. Any given petal can actually have a petal-width bias of ± 50 ppm (random). The global requirement of ± 25 ppm was satisfied with 88% allowable growth, including model, measurement and petal-width bias uncertainties, Figure 5-1.

Secondly, we performed a worst-case performance analysis, in which we conservatively assumed each parameter was biased toward the largest absolute petal-width bias limit (worse performance). This included the assumption that all components and materials were biased to the 3-sigma limits of the petal test article material measured CTE's, each of which was biased in the worst-case direction. In doing this, we neglect the fact that JPL has demonstrated the capability to tune the CTE's of the components on flight programs. This is especially true for the battens, which dominate petal-width. Also neglected is our ability to utilize a set of CTE selection criteria for the components. We then added a 10°C temperature uncertainty, in which we conservatively assumed the petals were systematically biased to the extreme of the temperature uncertainty in the direction that created worse performance on both the hot side and cold sides, diametrically opposed. For this very conservative worst-case, including model, scaling and petal-width bias uncertainties, the tighter global requirement was again satisfied, Figure 5-2.

Lastly, this program did not benefit from incorporating measured material properties, or a detailed petal assembly level analysis model, until after the ideal petal-width bias was established. All future programs, including milestone 6B, will benefit immensely from incorporating the collected data and analysis from this program and milestone 8A. Doing so will define a new ideal petal-width bias, and accordingly, a new ideal disk radius, with respect to validated models. The ideal petal-width bias is the reference from which the requirement is assessed. This milestone attempted to predict the material and structure behavior of a petal, whereas future programs will only need to refine the design, and better characterize the uncertainties.

It for these reasons, we feel confident that the results presented in this report are extremely robust to the flight on-orbit requirements, and that future programs will in fact attain better performance.

5.4 Future Work

The results of this program were large margins on nominal performance, and positive margin on a worst-case performance analysis. While these results are highly encouraging, we will work to improve our understanding of the design and our performance margins.

More specifically, work has already begun on redesigning the batten to edge joint to reduce the resulting midspan bowing. Per discussion in Section 3.3.3, the midspan bowing can and will be incorporated into the milestone 6B ideal petal-width bias, however, reducing midspan bowing is desirable, as smaller thermal deformations result in smaller uncertainty in performance.

An analysis of the reduction in error from incorporating the midspan bowing into future results showed a margin for the worst-case performance analysis of *100% margin* against the conservative requirement. Incorporating these results and reducing midspan bowing is a funded task to be completed in 2021 before the start of the petal test article for milestone 6B, see further discussion in Appendix B: Designing-Out Midspan Bowing. As part of the design process, we will define and prototype all the necessary hardware and interfaces for the medium-fidelity petal subsystem.

Upon the completion of milestones 6A and the updated flight design, the ideal petal-width bias will be updated for milestone 6B to include the validated results of this model, as well as the effect on performance of the as-measured uncertainties in the materials. This will limit risk of milestone 6B to only the difference in the already validated model, and our ability to reproduce those results with the additional hardware fidelity required by milestone 6B.

We will also assess the effect of petal self-stress on its thermoelastic distortion response. The petal structure is statically indeterminate, and can sustain several orthogonal states of self-stress (i.e. loads within its component members that are self-equilibrated, without the presence of external loading). As these states of self-stress vary over the petal lifetime (through manufacturing,

assembly and integration, release of gravity and gravity offload, non-uniform shrinkage due to moisture loss etc.), they could lead to variations in the stiffness matrix of the petal structure, which would affect the petal's thermoelastic distortion response to in-space temperatures. Using the structure finite element models already developed, we will assess the magnitude of these states of self-stress, the possible variations in these states over the petal lifetime, and the effect such self-stress may have on the thermoelastic response.

Acknowledgements

Special thanks to the tremendous efforts of all the engineers, scientists and contributors to the variously funded mechanical engineering efforts described in this report, including the teams at JPL, Tendeg, Applied Composites, Northrup Grumman, Southern Research, the Applied Sciences Lab and JLA.

The research was carried out at the Jet Propulsion Laboratory, California Institute of Technology, under a contract with the National Aeronautics and Space Administration (80NM0018D0004).

Acronyms

CFRP	Carbon Fiber Reinforced Polymer
CLT	Classical Laminate Theory
CTE	Coefficient of Thermal Expansion
DMI	Displacement Measuring Interferometers
FEM	Finite Element Model
IMF	Interferometric Measurement Facility
PPM	Parts Per Million
RPM	Revolutions per Minute

References

1. Willems, P., "Starshade to TRL5 (S5) Technology Development Plan," Tech. rep., Jet Propulsion Laboratory, Dec. 2018.
2. Seager, S., Kasdin, N. J., et al., "Starshade Rendezvous Probe Study Report," Tech. rep., Feb. 2019.
3. Gaudi, S., Seager, S., et al., "HabEx: Habitable Exoplanet Observatory Final Report," Tech. rep., Aug. 2019.

6 Appendix A: Petal-Width Bias

This Appendix details the definition of the *petal-width bias* that was adopted to characterize the key performance parameter defining petal on-orbit shape stability, the driver of on-orbit instrument contrast. This metric aims to accurately predict change in instrument contrast for a given thermally deformed petal. The reference curve is the change in instrument contrast for a perfect petal-width bias, which has uniform petal-width strain. We look for correlation between our petal-width bias metric for the actual thermally deformed petals, and that reference curve.

We determined that an accurate metric of petal-width bias is the median of the thermal width strain, excluding the petal tip. This metric was defined by analyzing various thermally deformed petals for the validated flight-design, as well as numerically created shapes applied to the flight design (with no actual physical effects driving strain). This metric was validated against our reference curve. The difference between the validated FEM and simulated cases, and the reference curve, is the uncertainty in the prediction. This difference is shown to be due to variations in the thermal strain around the petal-width bias, particularly at the petal midspan locations, and the tip. Nevertheless, over all the simulated cases spanning the range of expected thermal deformations, the deviation from the uniform strain curve was less than 1.2 ppm, 5% of the 25 ppm global bias requirement. Therefore, we can compute the petal-width bias utilizing the median of the thermal width strain, excluding the petal tip, and our calculation of petal-width bias will be accurate within ± 1.2 ppm. We apply this petal-width bias uncertainty against the requirement in quadrature with our measurement uncertainty in our milestone analysis.

6.1 Key Components of The Petal

In the following sections, x refers to the longitudinal axis of the petal, and y the width-wise axis of the petal. As described in Section 3.1, critical features that define the petal include the intersection of the batten with the optical edge, and the points on the edge between two battens, referred to as the midspans. The thermally induced deformations are relatively uniform at the petal edges corresponding to the batten-rod x locations, since these members are stiff, with minor variations in CTE (section 2.4). However, the optical edge displacements at the more compliant midspan locations are also affected by the movement in both x and y of the neighboring battens, and present much larger variations. The tip plate is made of quasi-isotropic CFRP, which has a CTE of roughly 0.0055 ppm/°C at -50°C, in the width-wise direction. But as the petal width gets thinner—by a factor of 7.5 with respect to the widest part of the tip plate—the CTE of the adhesive (EA9394, 63 ppm at -50°C) has a larger contribution to the width-wise thermal behavior. This results in very large strains at the tip, up to 25 times the thermal strain evaluated at the battens. These critical features are shown in Figure 6-1, and are used in the following simulations to define modified petal deformations and evaluate the effect of petal shape stability on optical contrast.

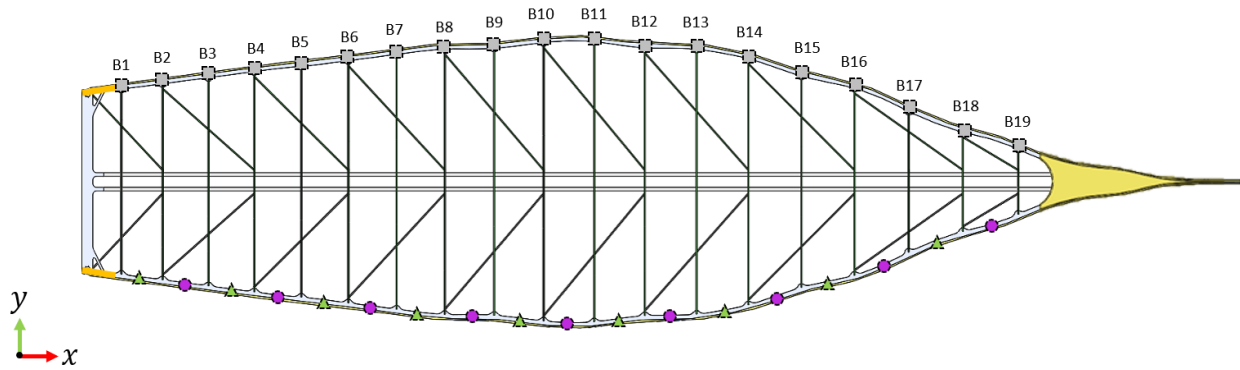


Figure 6-1. Flight-design petal with critical features highlighted. The 19 intersections of the battens with the optical edge (numbered gray squares on the top edge) are the most deterministic locations. The midspans (shown on the lower edge) are divided into two groups referred to as “odd” (green triangles) and “even” (magenta circles), and are differentiated by the location of the diagonal brace. The width-wise strain at the root and at the tip plate, shown in yellow, are also factors in determining the overall shape of the optical edge.

6.2 Petal Shape Variations

To evaluate the effect of petal-width variations on the optical performance of the starshade, and extract a correlation factor defined as the *petal-width bias*, different petal shapes were created with either thermal FEM predictions, exaggerations of those predictions, or artificially imposed variations. The analysis of the artificial variations was used to validate the definition of the petal-width bias (defined as the median excluding the tip) and obtain a sample set spanning the expected range of variations. To *artificially* modify the shape of the petal from the nominal flight design, strains were imposed on a number of control points at the root of the petal, the batten locations, the midspan locations, and the tip plate (Figure 6-1). The strains at the remaining points that define the optical edge were calculated by cubic spline interpolation, using the previously defined control points as queries. The word “artificially” is used here to differentiate these cases from those where the petal widths were obtained directly with the results of the flight-design, validated FEM. Three different series of cases (A, B, and C) are described below:

- A. **Constant width strain imposed everywhere along the petal.** These cases are equivalent to assuming that the petal is constructed of a single material of uniform CTE, and undergoes uniform thermal soak. The petal grows or shrinks with a constant width-wise strain from the root to the tip.
- B. **Artificial width strain imposed using regular patterns.** A constant width strain (± 10 , ± 20 , or ± 25 ppm) is imposed at the 19 batten locations, between the root and the first batten, and at the tip plate. Additionally, variations between the battens are introduced by forcing the strain at the midspan locations to a constant value (within ± 25 ppm of the battens). The midspans either all have the same strain (all the same direction), or are set so that the even and odd midspan strains alternate around the batten strain (Figure 6-2 and Figure 6-3).

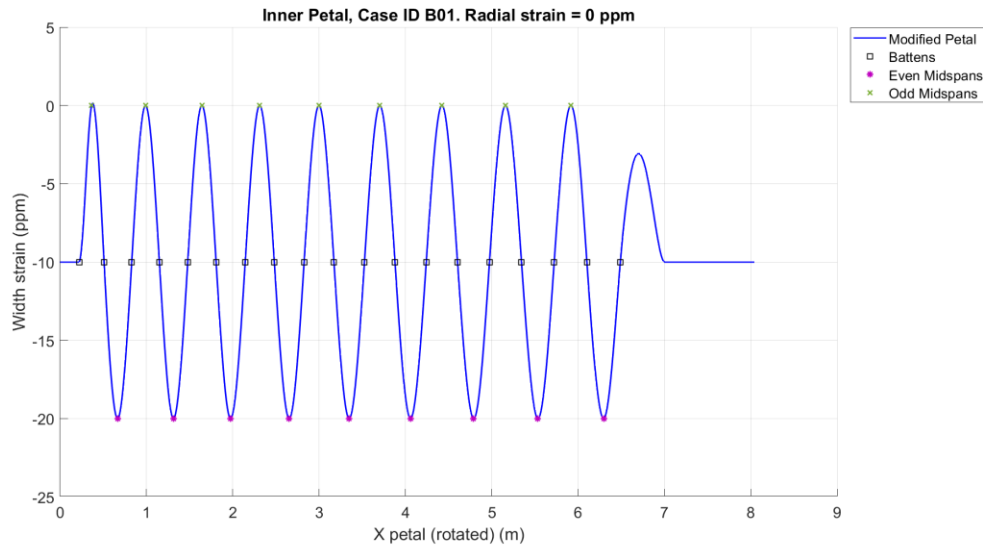


Figure 6-2. Artificially imposed width strain along the petal length. For B01, the root, battens, and tip are set to -10 ppm, all even midspans set to -20 ppm, and all odd midspans set to 0 ppm, creating an alternating pattern.

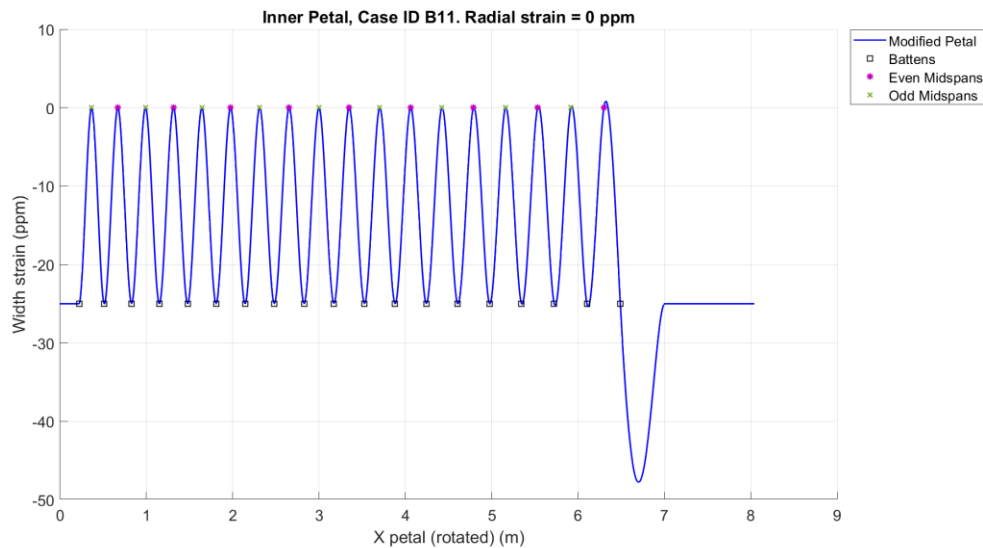


Figure 6-3. Artificially imposed width strain along the petal length. For B11, the root, battens, and tip are set to -25 ppm, and all even and odd midspans set to 0 ppm.

- C. **Width strain imposed used flight-design, validated FEM outputs.** Various simulations, including the worst-case condition (Section 2.4), were analyzed to evaluate the petal shape stability at different sun angles, and were presented in this report. The change in instrument contrast of starshades with these petal-width distributions is evaluated and compared to the metric defined as *petal-width bias* (defined in Section 6). These cases include results for SA83 and SA40, with the worst-case condition (3-sigma CTE's & temperature uncertainties of $\pm 10^\circ\text{C}$), and also, scenarios with very large CTE variations, e.g. up to 100% increase (which is an arbitrary variation value).

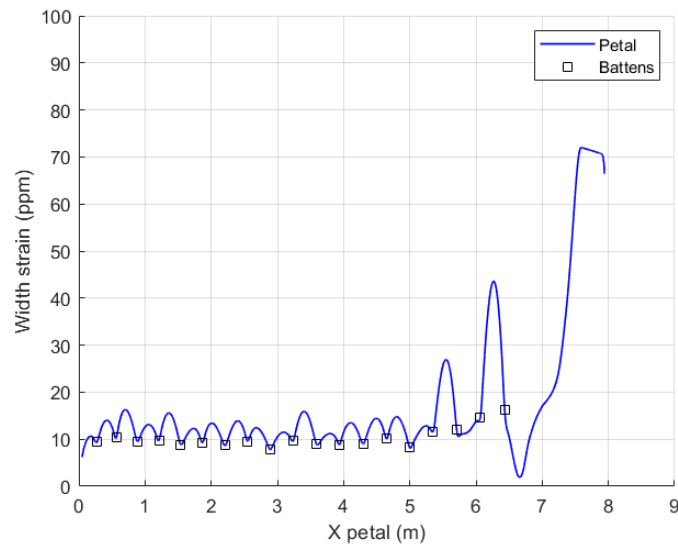


Figure 6-4. Flight-design validated FEM results for the width strain along the petal length for a sun angle of 40° (hot).

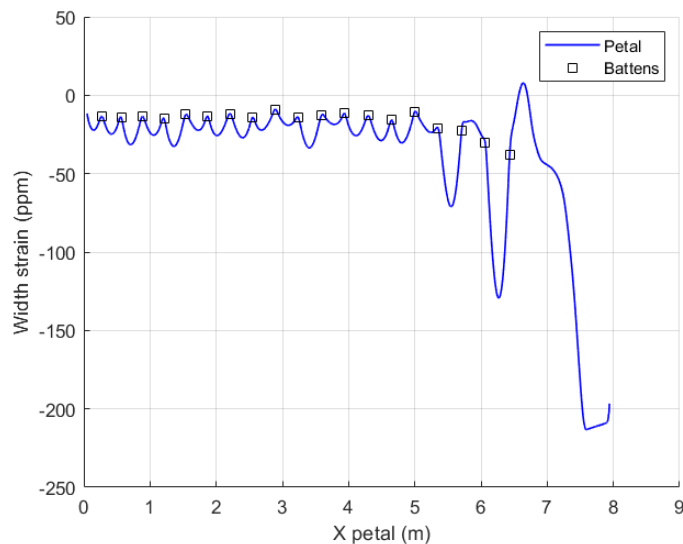


Figure 6-5. Flight-design validated FEM results for the width strain along the petal length for a sun angle of 83° (cold).

6.3 Correlation Between Instrument Contrast and Petal-Width Bias

Analysis of the change in instrument contrast of starshades with petal widths modified from nominal (following the process described in the previous section), showed that the instrument contrast was proportional (in quadrature) to an overall change in petal width-wise strain. More specifically, large variations at the midspans did not have a strong effect on contrast, and the driving parameter could be defined as the median of the width strain, calculated from the root of the petal to the beginning of the tip plate ($x \approx 7$ m)—excluding any contributions from the tip. Although the average of the petal-width strain was considered as a metric, it was too sensitive to variations in the midspans. The median, however, is not skewed by small proportions of extremely

large or small values, and characterizes the strain at the midpoint of the distribution. The following results show the strong correlation between this term and the change in instrument contrast for a wide range of petal shapes. As a result, the *petal-width bias* is simply the median of the petal-width strain, excluding the tip plate.

- A. **Constant width strain imposed everywhere along the petal.** These results serve as the optical performance reference, with the contrast change from nominal following a quadratic behavior as a function of the petal-width bias, as expected.

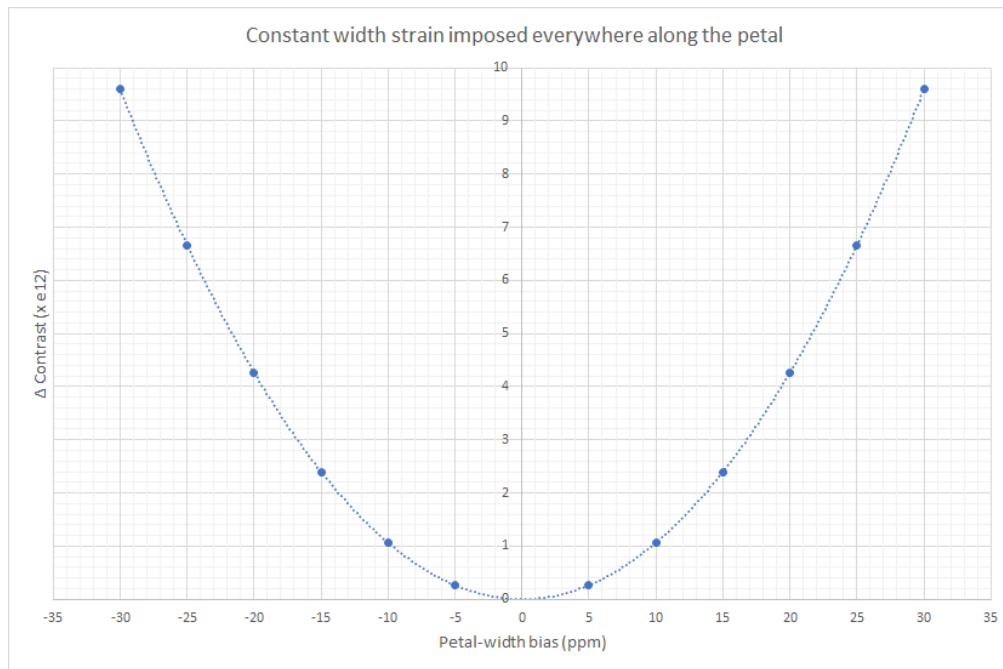


Figure 6-6. Contrast difference between starshades with petals with constant width strain (with respect to nominal) and the design.

- B. **Artificial width strain imposed using regular patterns.** Although the variations in strain of the midspans were quite large in some of these cases (up to ± 25 ppm), the petal with regular strain patterns imposed, when evaluated at the petal-width bias, followed the reference curve with strong correlation. The correlation uncertainty, defined as the strain difference between the measured petal-width bias and the petal-width bias of the reference curve, was below 1.7 ppm.

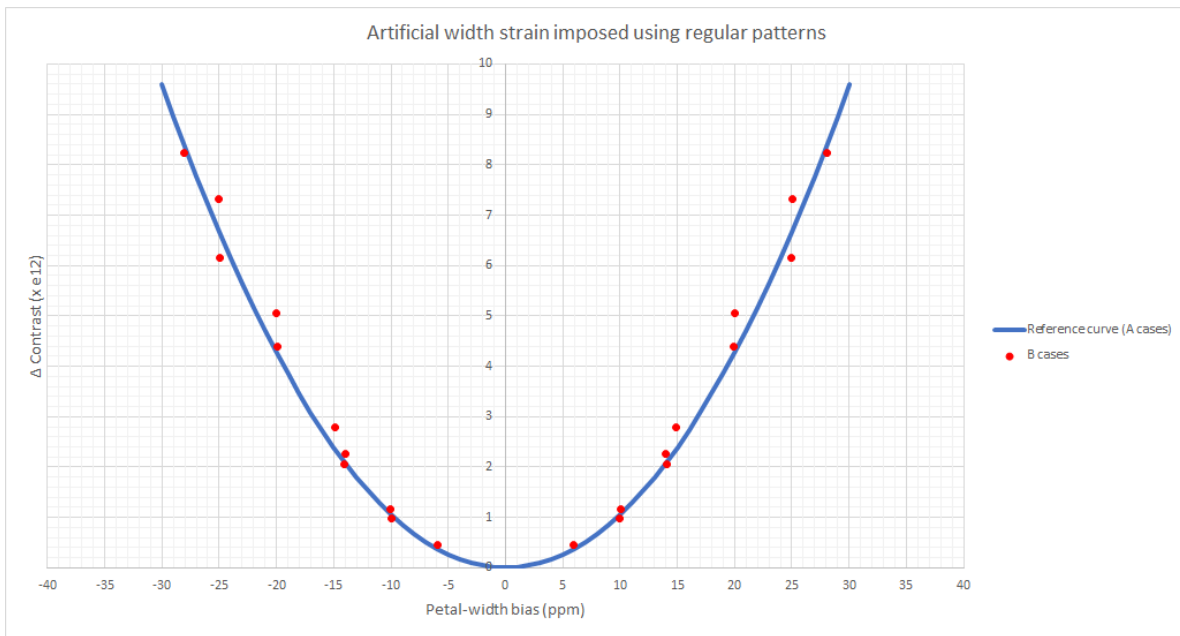


Figure 6-7. Contrast difference from nominal for starshades with petals undergoing artificial variations, with constant strains imposed at the root, battens, tip, and midspans (red points). The reference curve (constant strain cases A) is added for reference, and demonstrates a strong correlation as a function of petal-width bias (median up to 7 m).

- C. **Width strain imposed used flight-design, validated FEM outputs.** The contrast difference from nominal of starshades with petal widths predicted by the FEM also followed the reference curve when using the petal-width bias as a characteristic metric of shape change. It is important to note that these thermally deformed petals are for the on-orbit predicted temperatures, but they are maintained at the nominal (undeformed) disk radius. This results in a net larger change in contrast for the given thermally deformed petal. This logically follows because the petal-width bias error will be larger for the cases presented herein, as compared to ideal disk radius. The correlation uncertainty was below 1.2 ppm for the cases of interest to our on-orbit scenarios.

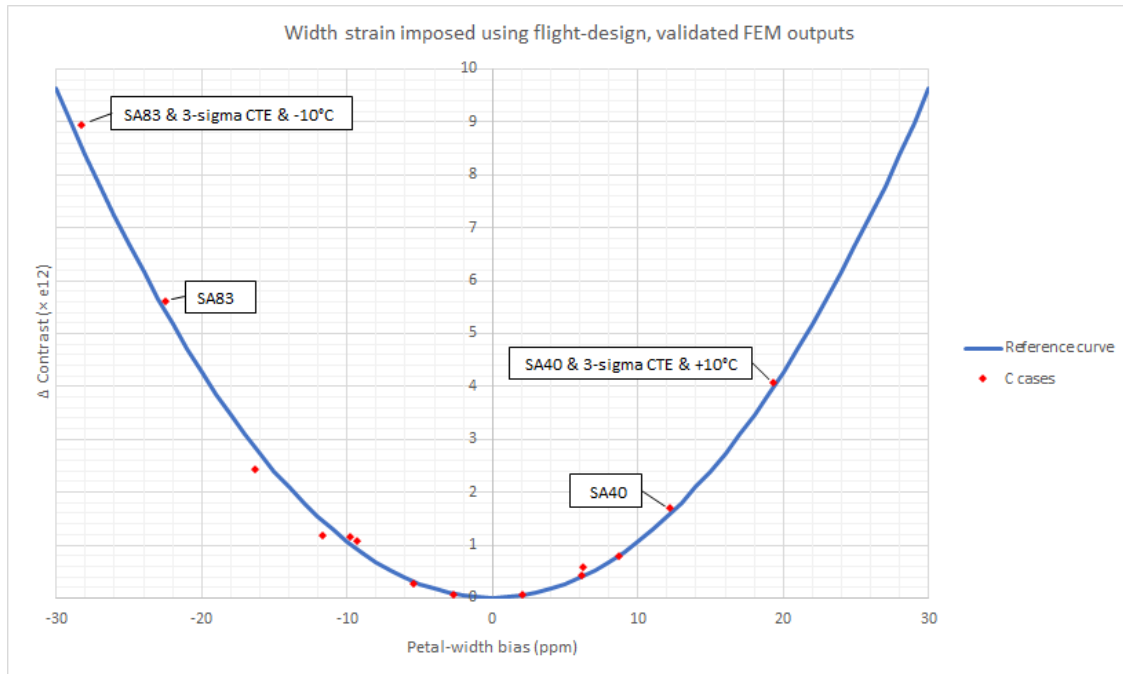


Figure 6-8. Contrast change from nominal as a function of petal-width bias for flight-design, validated FEM predicts, including worst-case assumptions on material CTEs and temperature uncertainty.

6.4 Summary of Simulation Results

The results of these simulations demonstrate that the petal-width bias, as calculated by the median of the petal-width thermal strain, excluding the petal tip, is an accurate metric of contrast performance due to petal on-orbit thermal deformations. We validated this metric with simulations, including FEM and simulated cases against a reference curve, the change in instrument contrast for a perfect petal-width bias, which has uniform petal-width strain. The uncertainty in the prediction for our cases of interest is 1.2 ppm, or 5% of the 25 ppm global bias requirement. This uncertainty is due to the thermal strain variations about the petal-width bias of the midspans (ripples) and the tip. We apply this petal-width bias uncertainty against the requirement in quadrature with our uncertainty for our milestone analysis.

7 Appendix B: Designing-Out Midspan Bowing

The midspan bowing (ripples) along the petal edge is an artifact of two factors: the batten to optical edge joint effect on edge bowing, see Appendix G: Batten to Optical Edge Joint Effect on Edge Shape - Midspan Bowing, and the difference in thermal strain between the optical edge and the spine. If these two sources of midspan ripples are reduced or eliminated, the petal-width bias will be reduced, and as discussed in Section 3.3.3, the uncertainty in the midspan bowing is the largest source of petal-width bias error for milestone 6B.

The batten to optical edge joint effect on midspan bowing is currently being studied as part of the post-milestone 6A effort in moving forward toward milestone 6B, per discussion in Section 5.4. Preliminary results show a redesign of the joint will greatly reduce the midspan bowing effect of the joint, and ongoing work will continue to refine the design toward that end.

With a reduction in the effect of the batten to edge joint, the difference in thermal strain between the optical edge and the spine will still contribute to midspan bowing. This effect is the product of the difference in CTE and temperature between the edge and the spines. In other words, if the entire petal were a uniform CTE and temperature, the petal would only shrink and grow uniformly, and there would be no shape irregularities (no ripples). To eliminate or greatly reduce the ripples that form along the edge, we need to reduce or eliminate the difference in thermal strain between the edge and spine. The task then is to best match the thermal strain profiles for these two components, for the given sun angle environment. Ideally, we would eliminate any difference between the spine and edge thermal strain, however in practice, this is not possible, due to the difference in temperature between the two components across the sun angle environment, and so we reduce the difference between the two, with a focus on the sun angle environment that drives performance.

Matching thermal strain profiles of the edge and spine is the most obvious and simple way to resolve edge rippling, however, other options exist. An option we explored was removing the constraints between the edge and spine, which is what is allowing the differential thermal strain to couple between the two components. It was found that releasing the constraints between the spine and battens also had the same effect as matching the thermal strain. In our current design, Figure 7-1, the spine is 1/8" thick, and passes through the 5/16" thick battens via slots in the battens. The spine is bonded to the batten at these locations, but the constraint is not necessary structurally. Removing that bond is another way to relieve differential thermal strain between the spine and edge. The slotted/free slide joint is the same as what is already implemented at the batten/brace joint, also pointed out in the figure. The brace passes through a slot in the batten, and has no epoxy, it is free to slide, which is done to eliminate structural redundancy.

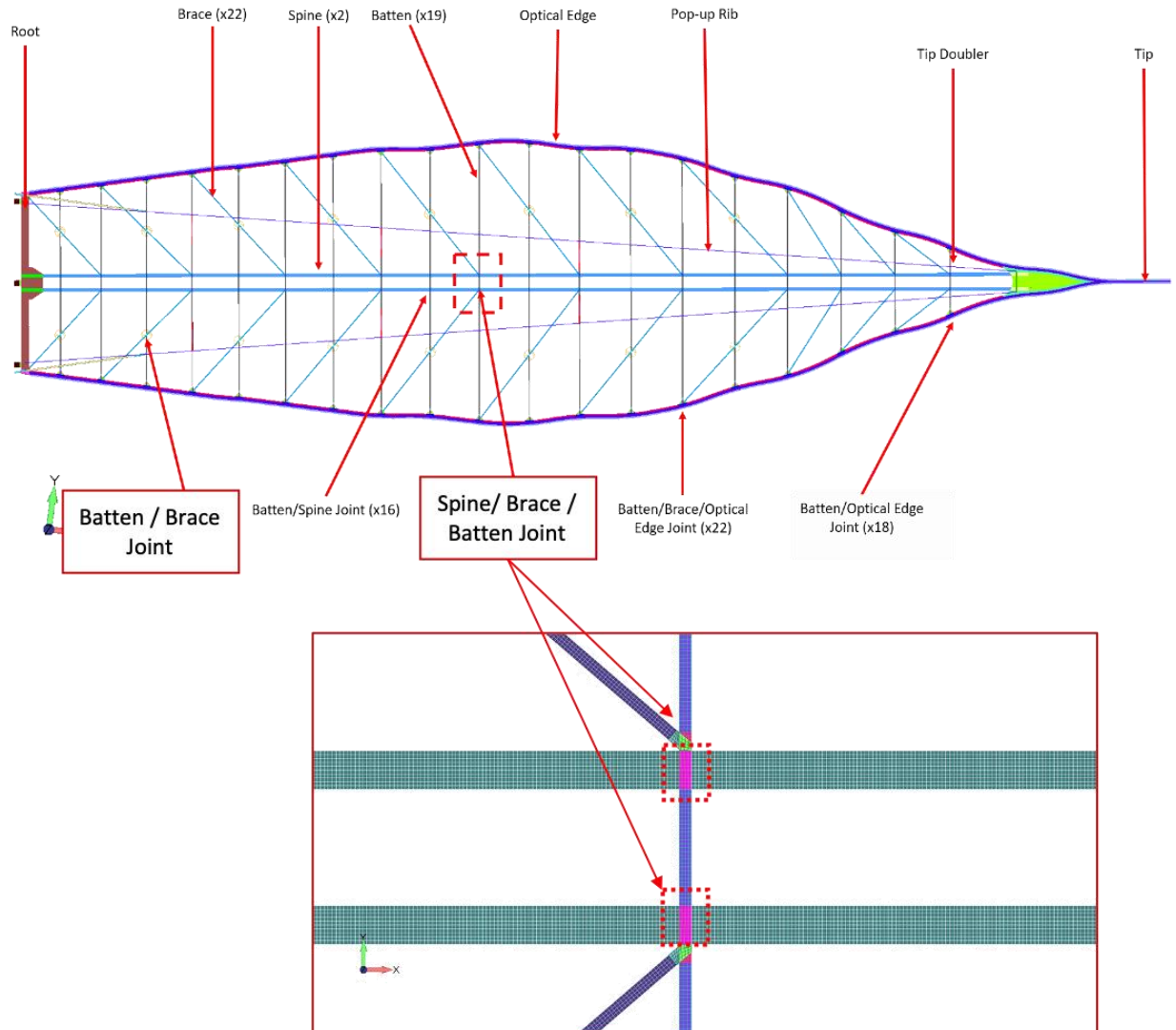


Figure 7-1. Current petal design, with detail of the spine interface to the batten. Currently this joint is bonded, but it could be free to slide, exactly as the batten/brace joint is now. This would also be performed at the tip, where the spine is constrained in a slot within the tip. This would relieve differential thermal strain between the spine and edge, an option for eliminating ripples.

Figure 7-2 shows the effect on ripples of the two options explored for reducing midspan ripples, matching thermal strain and releasing the batten-spine joint to slide. The matched thermal strain is straight-forward to do, with no impact on the hardware, and will definitely be implemented for milestone 6B. The spine-batten joint release models the joint already at the brace to batten joint, however it will need to be considered more thoroughly for any impacts on the hardware. We find that the first iteration of matched thermal strain has a significant impact on reducing ripples, but that releasing the spine from the battens all but eliminates the ripples.

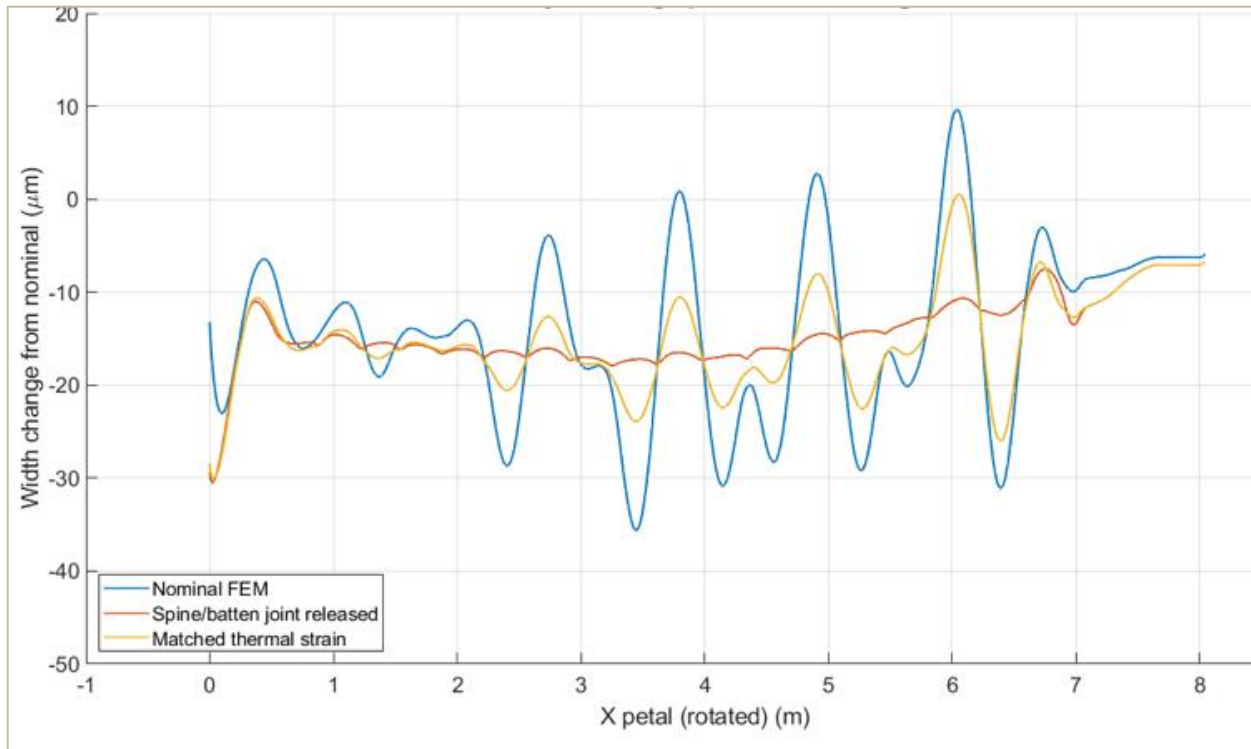


Figure 7-2. Petal-width change from nominal in microns for the SA83 thermally distorted petal with the nominal case, thermal strain matching and spine/batten joint release.

8 Appendix C: Additional Plots & Figures

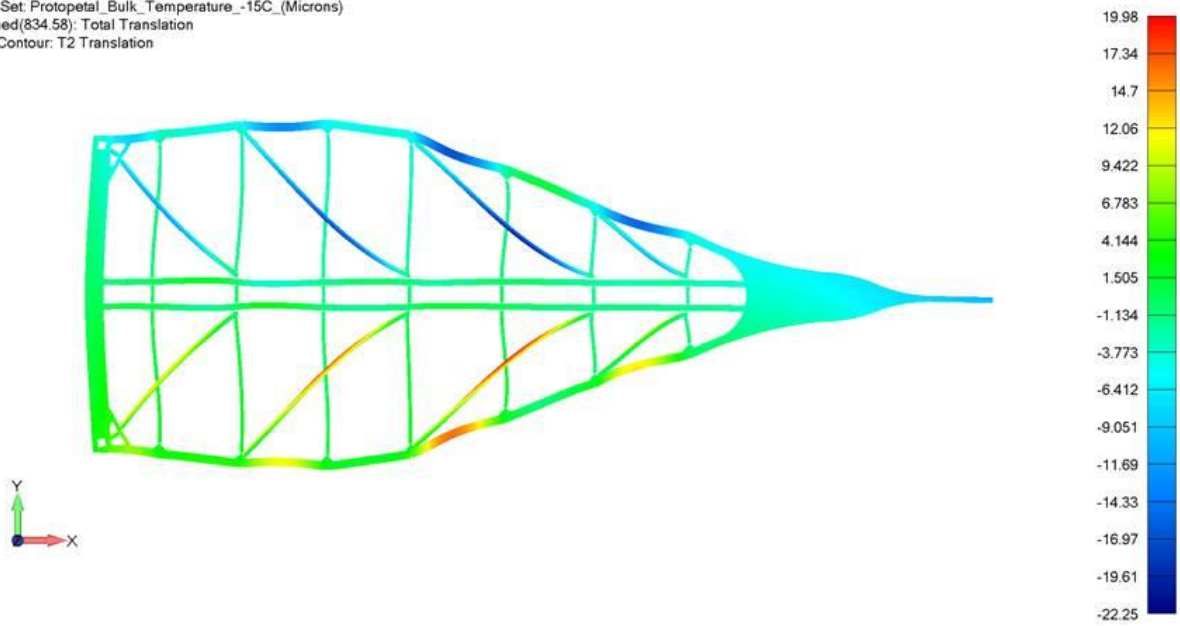
Table 8-1: System Uncertainty (with 4000 μ -Radian Abbé Rotation and Temperature > -20 °C)

	Variable	Sensitivity	Coefficient	Uncertainty across 1 meter (micron)	Uncertainty across 2 meters (micron)
1	Laser wavelength	$\pm 0.067 \text{ } 2\sigma \text{ ppm/lifetime}$	path length	0.07	0.13
2	Elec Error (resolution)	$\pm 1 \text{ LSB } (0.01 \mu)$	fixed	0.01	0.01
3	Optics Non-linearity (est.)	0.0022 μ	fixed	0.00	0.00
4	BK7 Retro Reflector ε_T differential	7.1 ppm/°C	$\Delta T \cdot \text{height (est } 1^\circ\text{C} \times 10.2\text{mm)}$	0.07	0.07
5	PBS Reference Point	0.55 ppm/°C	max Δ from CL (6.35mm x 70°C)	0.24	0.24
6	Invar Retro-Reflector Holder Reference Point	1.2 ppm/°C	max Δ from retro face 5.7mm x 70°C	0.48	0.48
7	Abbe error beam asymmetry	$[\sin\theta_x - \sin\theta_{(x+\text{error})}] / 2$	0.5mm and 4000 μ radians	1.00	1.00
8	Atmospheric Compensation - Relative Humidity	0.01 μ /meter per %RH at 620mm Hg	$\pm 2.5 \text{ \%RH}$	0.03	0.05
	Atmospheric Compensation - Relative Humidity	0.01 μ /meter per %RH at 620mm Hg	0.003 m	0.00	0.00
9	Atmospheric Compensation - Temperature	0.89 μ /meter per °C at 620mm Hg	1 °C	0.89	1.78
	Atmospheric Compensation - Temperature	0.89 μ /meter per °C at 620mm Hg	0.003 m	0.21	0.21
10	Atmospheric Compensation - Barometric Pressure	0.36 μ /meter per mm Hg	$\pm 0.225 \text{ mm Hg}$	0.81	1.62
	Atmospheric Compensation - Barometric Pressure	0.36 μ /meter per mm Hg	0.003 m	0.15	0.15
11	Atmospheric Compensation - O ₂ Concentration	6ppm pure N ₂ to Air	$\pm 1\% \text{ O}_2 / 20\% \text{ O}_2 \times 6 \text{ ppm}$	0.90	0.60
			cumulative	4.26	6.35
			RSS	1.70	2.74

Table 8-2: System Uncertainty (with 4000 μ -Radian Abbé Rotation and Temperature \leq -20 °C)

	Variable	Sensitivity	Coefficient	Uncertainty across 1 meter (micron)	Uncertainty across 2 meters (micron)
1	Laser wavelength	$\pm 0.067 \text{ } 2\sigma \text{ ppm/lifetime}$	path length	0.07	0.13
2	Elec Error (resolution)	$\pm 1 \text{ LSB } (0.01 \mu)$	fixed	0.01	0.01
3	Optics Non-linearity (est.)	0.0022 μ	fixed	0.00	0.00
4	BK7 Retro Reflector ε_T differential	7.1 ppm/°C	$\Delta T \cdot \text{height (est } 1^\circ\text{C} \times 10.2\text{mm)}$	0.07	0.07
5	PBS Reference Point	0.55 ppm/°C	max Δ from CL (6.35mm x 70°C)	0.24	0.24
6	Invar Retro-Reflector Holder Reference Point	1.2 ppm/°C	max Δ from retro face 5.7mm x 70°C	0.48	0.48
7	Abbe error beam asymmetry	$[\sin\theta_x - \sin\theta_{(x+\text{error})}] / 2$	0.5mm and 4000 μ radians	1.00	1.00
8	Atmospheric Compensation - Relative Humidity	0.01 μ /meter per %RH at 620mm Hg	$\pm 2.5 \text{ \%RH}$	0.03	0.05
	Atmospheric Compensation - Relative Humidity	0.01 μ /meter per %RH at 620mm Hg	0.003 m	0.00	0.00
9	Atmospheric Compensation - Temperature	0.89 μ /meter per °C at 620mm Hg	1 °C	0.89	1.78
	Atmospheric Compensation - Temperature	0.89 μ /meter per °C at 620mm Hg	0.003 m	0.21	0.21
10	Atmospheric Compensation - Barometric Pressure	0.36 μ /meter per mm Hg	$\pm 0.225 \text{ mm Hg}$	0.81	1.62
	Atmospheric Compensation - Barometric Pressure	0.36 μ /meter per mm Hg	0.003 m	0.15	0.15
11	Atmospheric Compensation - O ₂ Concentration	6ppm pure N ₂ to Air	$\pm 1\% \text{ O}_2 / 20\% \text{ O}_2 \times 6 \text{ ppm}$	0.90	1.80
12	Data Stitching	Accumulation of stitches	engineering judgment estimation	2.00	2.00
			cumulative	6.86	9.55
			RSS	2.76	3.80

Output Set: Protopetal_Bulk_Temperature_-15C_(Microns)
Deformed(834.58): Total Translation
Nodal Contour: T2 Translation



Output Set: Protopetal_Bulk_Temperature_-50C_(Microns)
Deformed(1708.6): Total Translation
Nodal Contour: T2 Translation

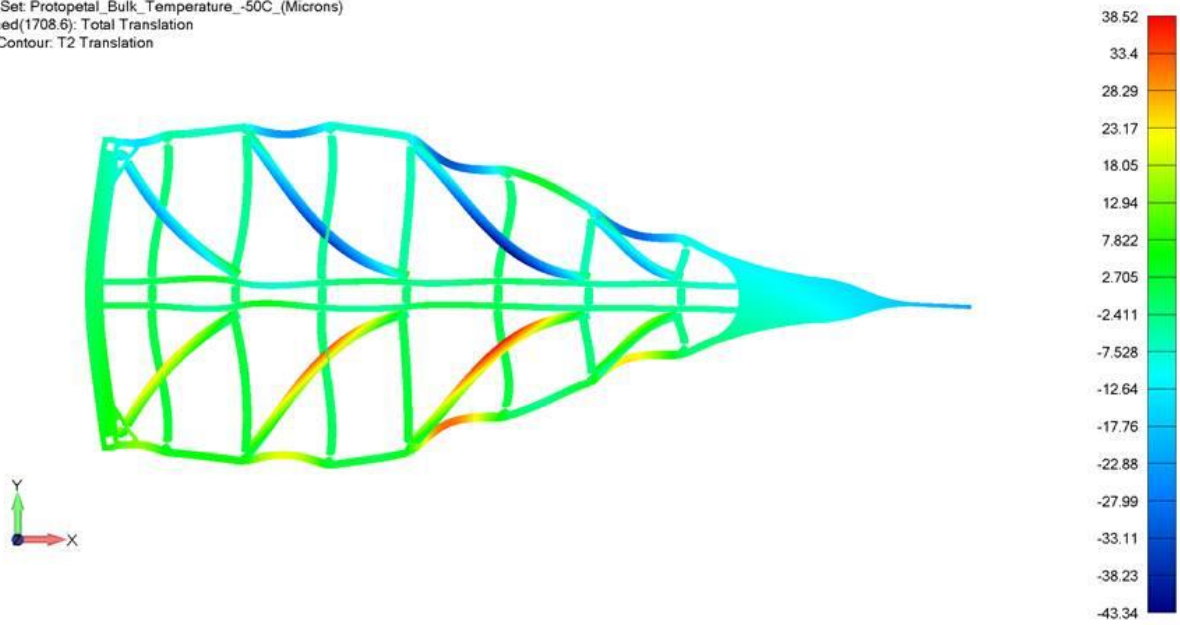


Figure 8-1. Thermal deformation plots for -15°C (top) and -50°C (bottom), scale in microns.

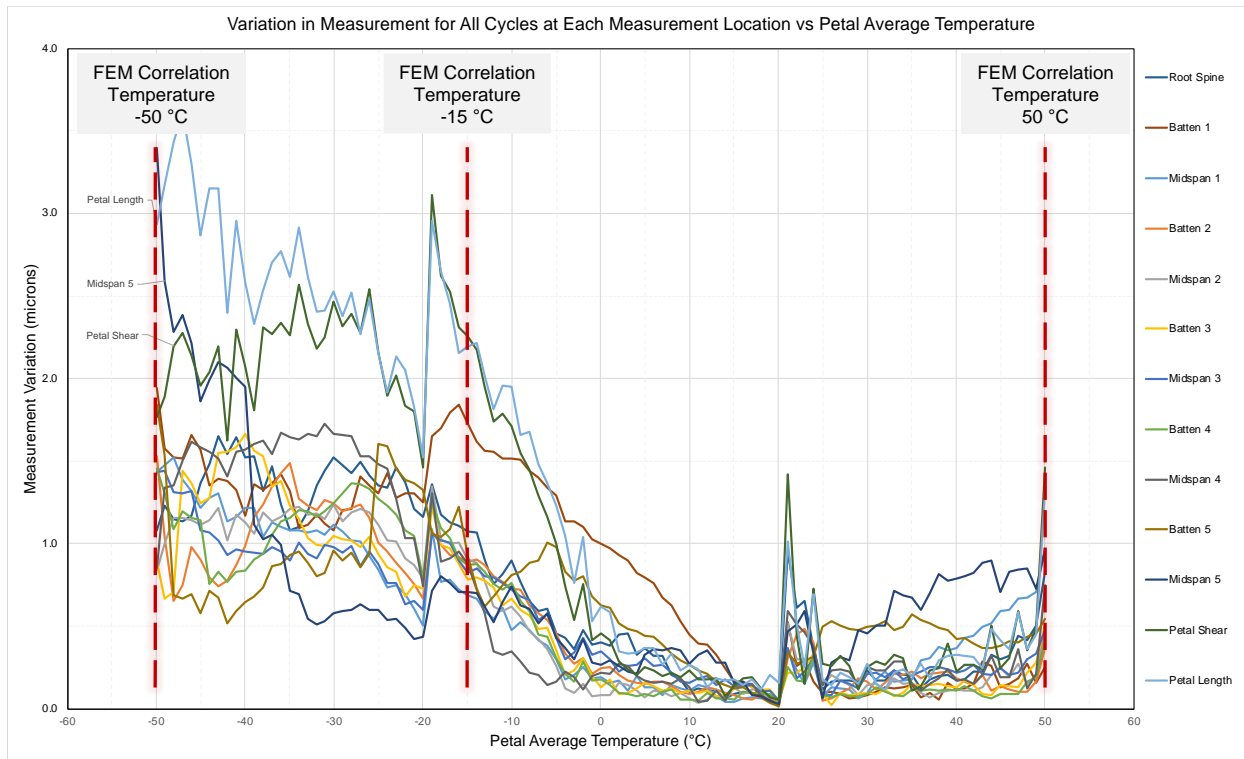
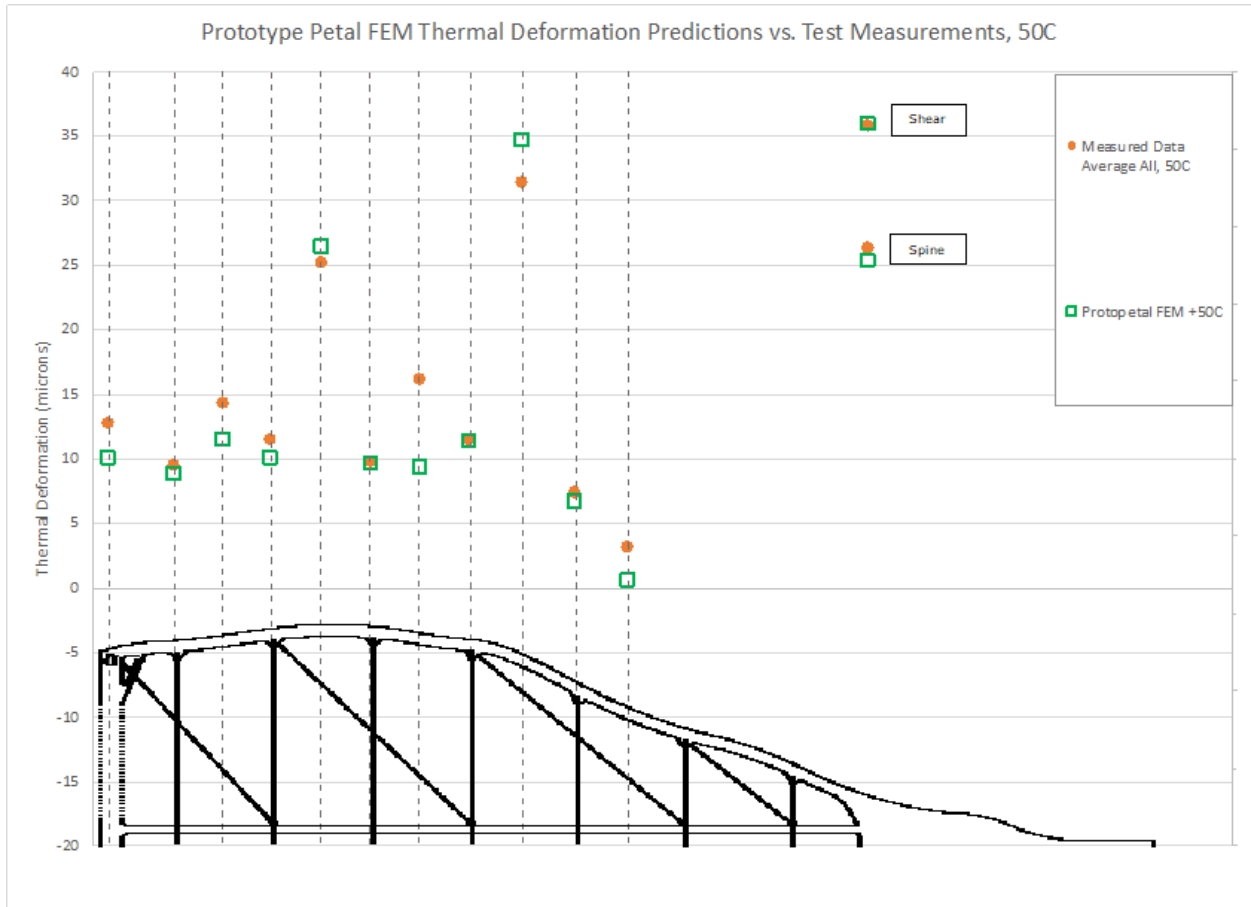
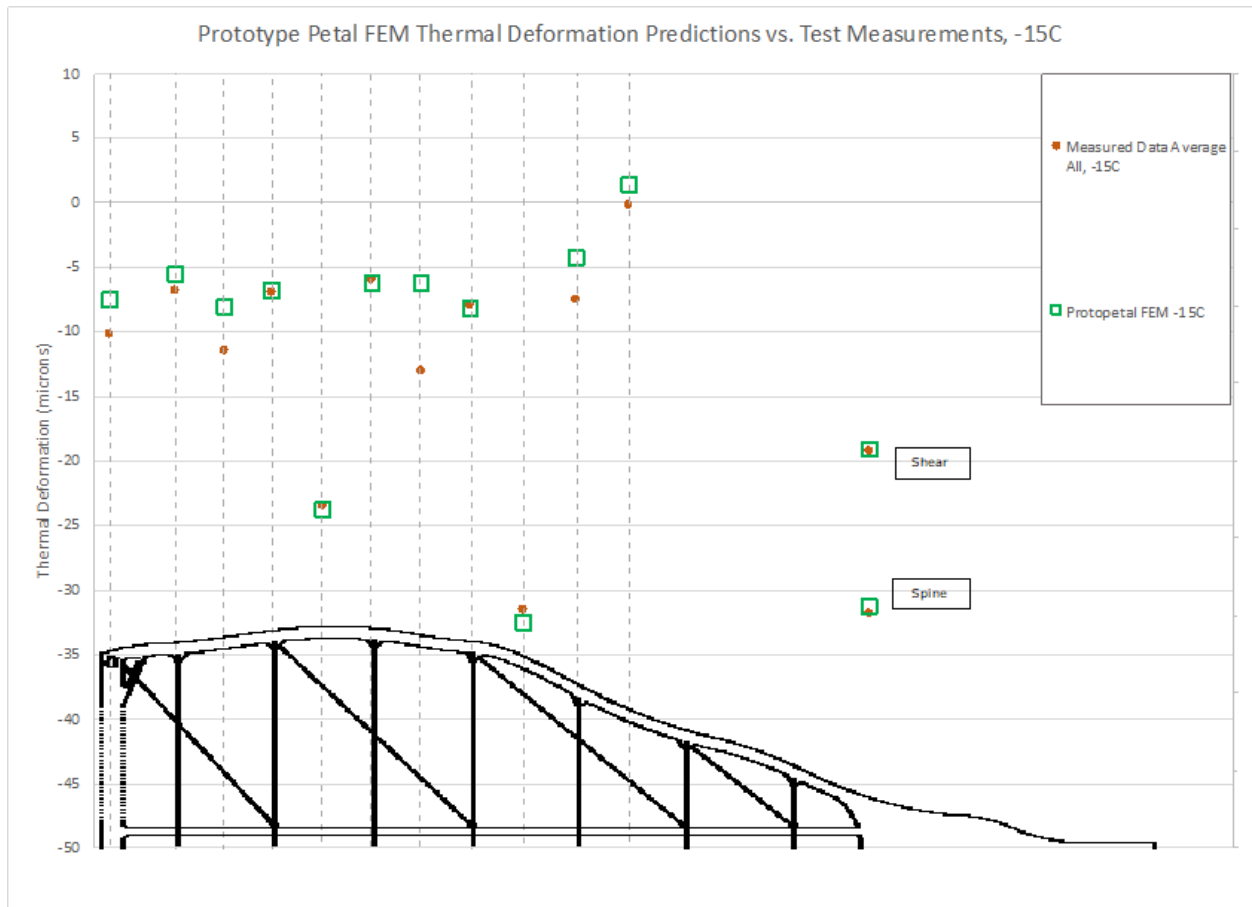


Figure 8-2. The variation in measurement values for all cycles at each of the measurement locations as a function of the petal average temperature. The largest variations were in the longest measurement locations (e.g. petal length) and where the measured value was near zero (e.g. midspan 5), which is to be expected. The variation of the measurements from cycle to cycle are within the system measurement uncertainty. System measurement uncertainty increased for colder temperatures, largely due to freezing of moisture in the air, which caused measurement dropouts, and because the oxygen and other sensors used for measurement correction dropped out below -15°C.





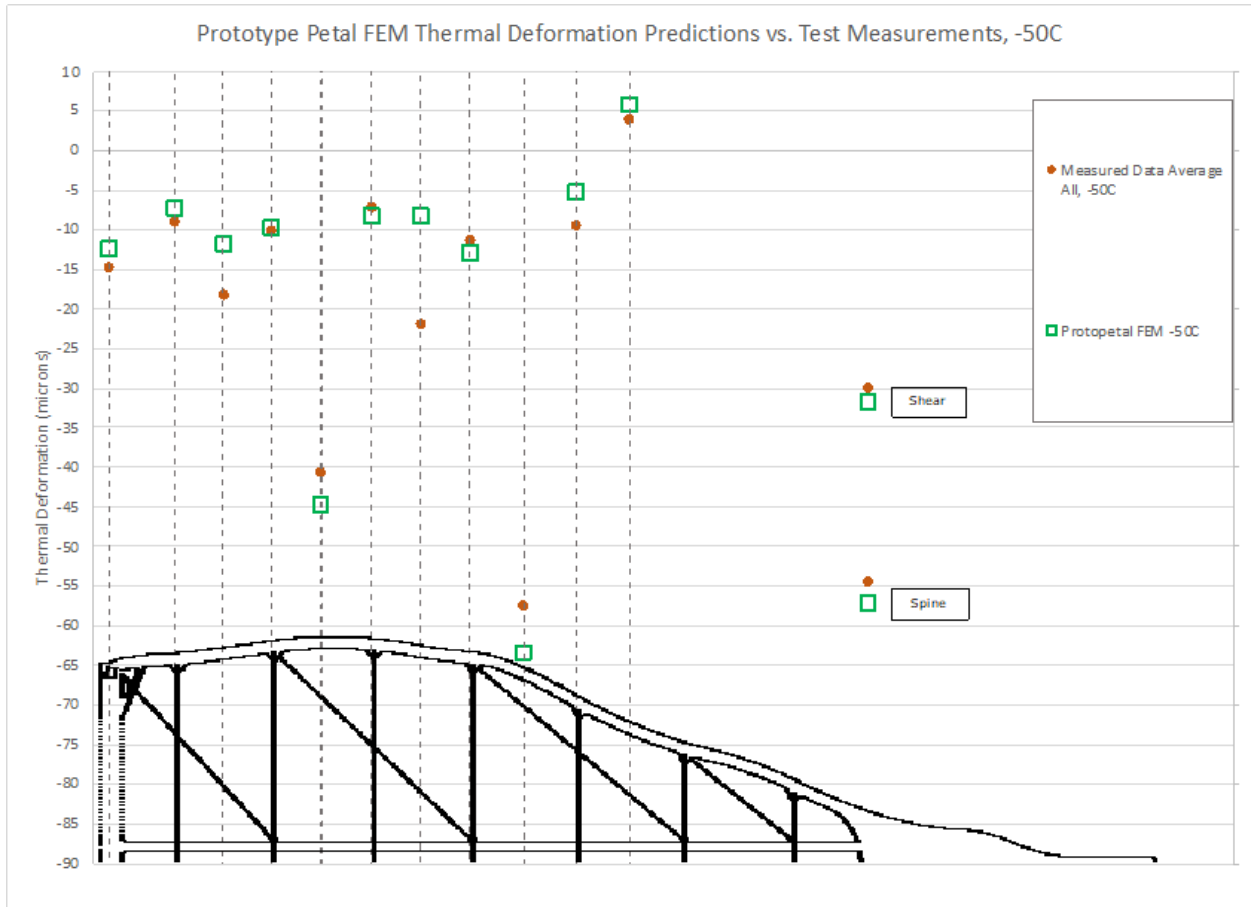
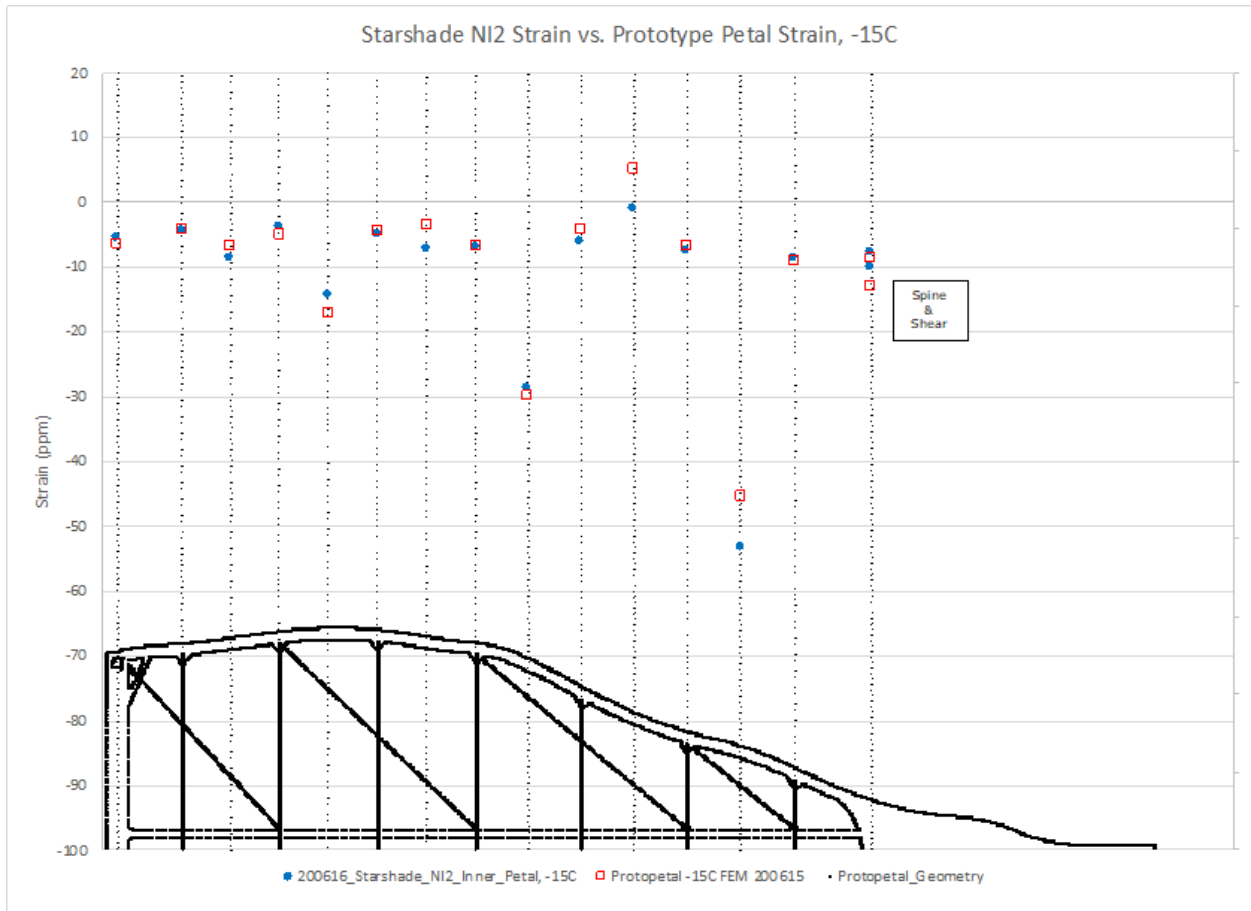


Figure 8-3. Prototype petal finite element predictions vs. test measurements for the 50°C, -15°C and -50°C cases. The y-axis is in microns and the petal geometry is along the x-axis, and vertical dashed grey lines align the geometry with the predicted and measured values at each location. The petal length and shear measurement are individually labeled, and align with the tip of the petal, at which the retroreflector was placed.



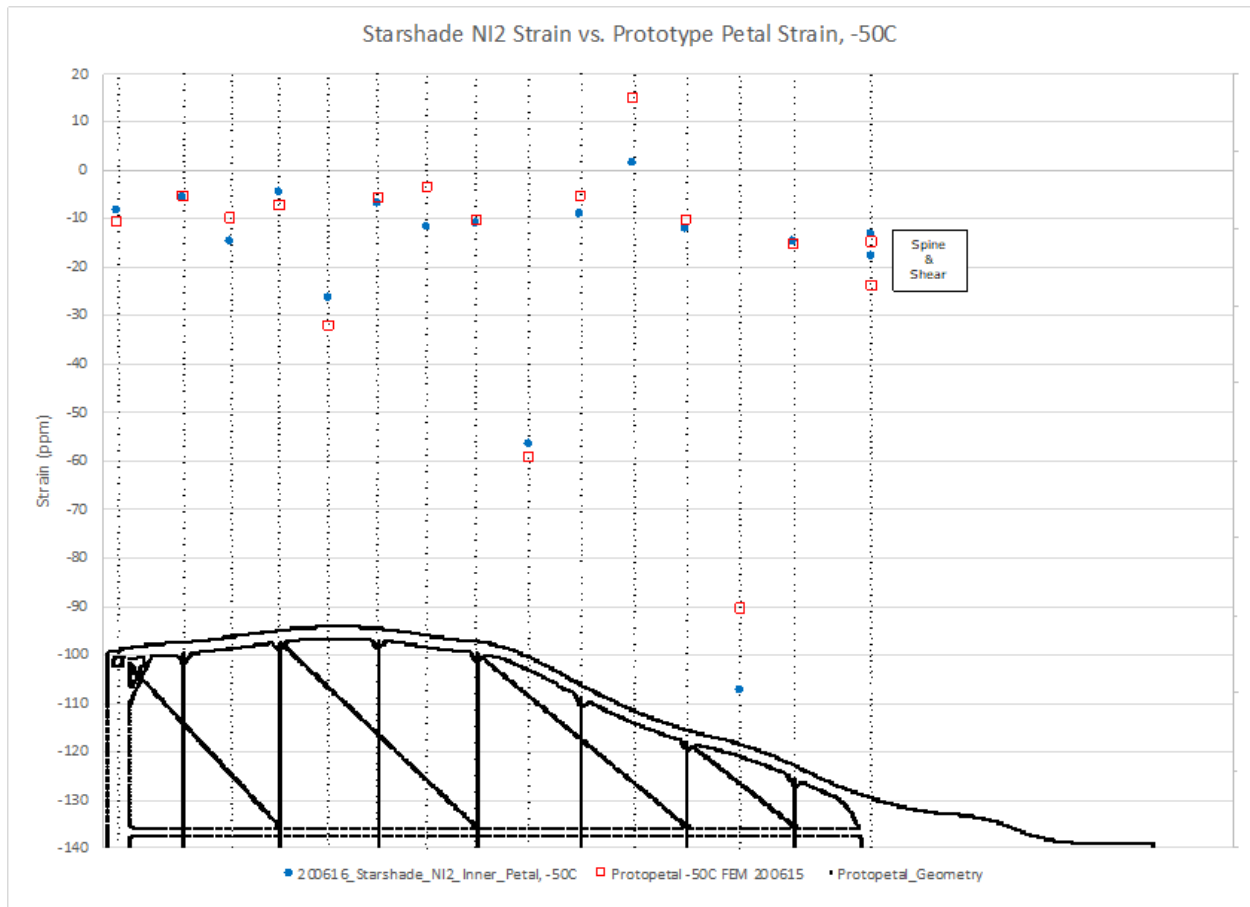


Figure 8-4. Correlation between validated prototype petal and flight petal for the -15°C and the -50°C cases. The y-axis is in thermal strain (ppm) and the petal geometry is along the x-axis, and vertical dashed grey lines align the geometry. The prototype petal measurements are red boxes, while the flight petal are blue dots. The petal length and shear measurement are individually labeled, and align with the measurement location at the tip of the petal. The flight petal is modeled with the same techniques and material properties; however, we crosscheck the flight model response at the prototype petal test temperatures to verify that the flight petal FEM response is similar in behavior and magnitude. The first two battens and midspans from the inboard section of the petal are matched to the corresponding flight geometry, and the remainder of the battens and midspans are matched to the outboard section of the petal, from which the tip of the prototype petal was designed, per Section 3.3.1. The correlation is not expected to be an exact because the overall geometry of the two petals is different, however we find that the results are both similar in behavior and magnitude and consider the flight petal geometry to be accurately modeling the behavior of the test article.

9 Appendix D: Material Properties

Samples for each component and material from which the petal was made were cut from the lot, and were measured at the Interferometric Metrology Facility at NGIS described in milestone 8A. We used the average thermal strain of the sample set for the nominal on-orbit predictions, and for prototype petal model correlation, but then calculated 3-sigma variations from the samples to use in the worst-case performance prediction.

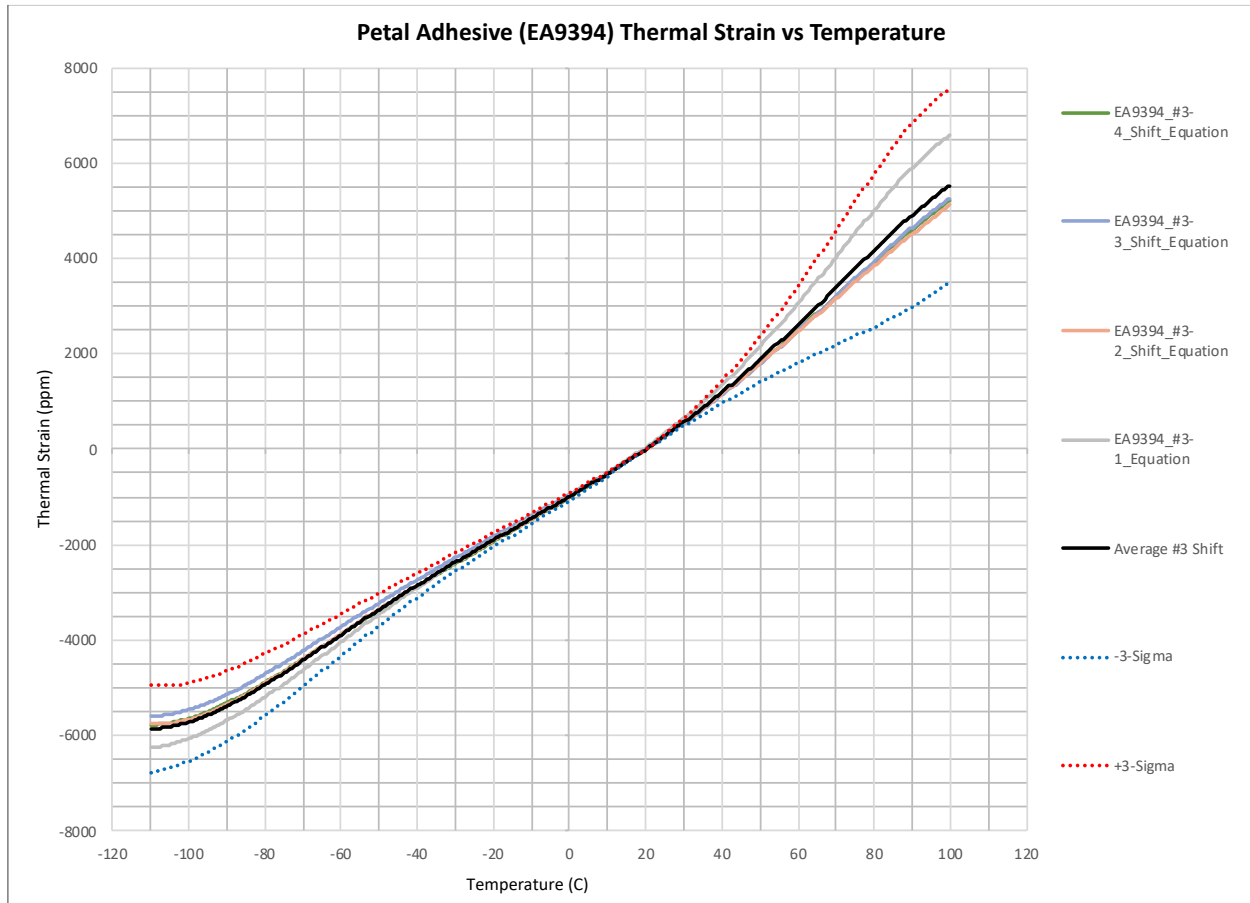


Figure 9-1. Petal adhesive (EA9394) thermal strain vs temperature used to bond the individual components together at room temperature to the shape of the petal. The variability of the CTE for the samples is shown, as well as the calculated 3-sigma variation in those samples, which was used in the worst-case performance prediction.

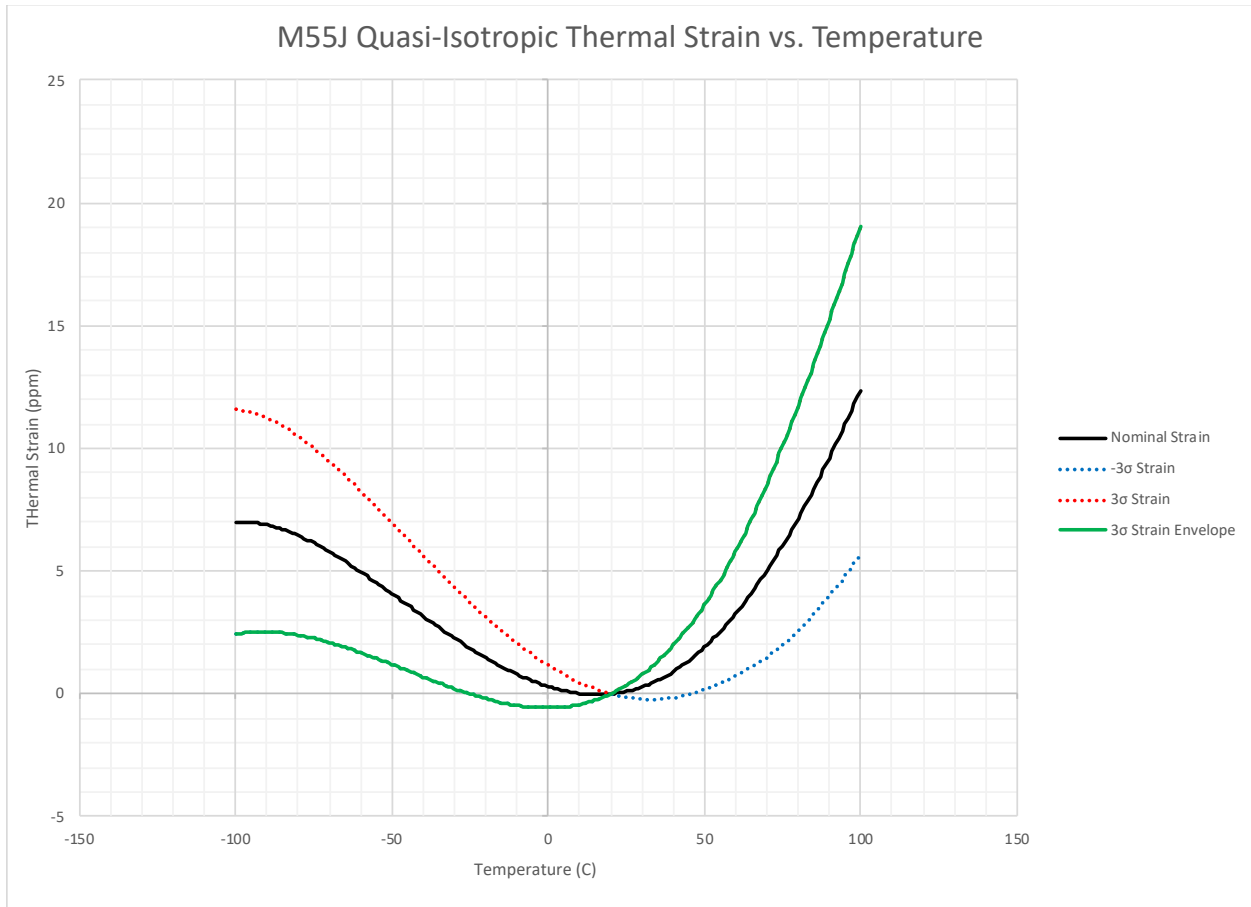


Figure 9-2. Quasi-isotropic M55J CFRP laminate data. The nominal (average) thermal strain and resulting 3-sigma bounds of all samples is shown, which was used in the worst-case performance prediction. The worst-case standard deviation for all laminate samples for the varying layups was used to conservatively bound laminate performance. The quasi-iso is shown as an example of the final result.

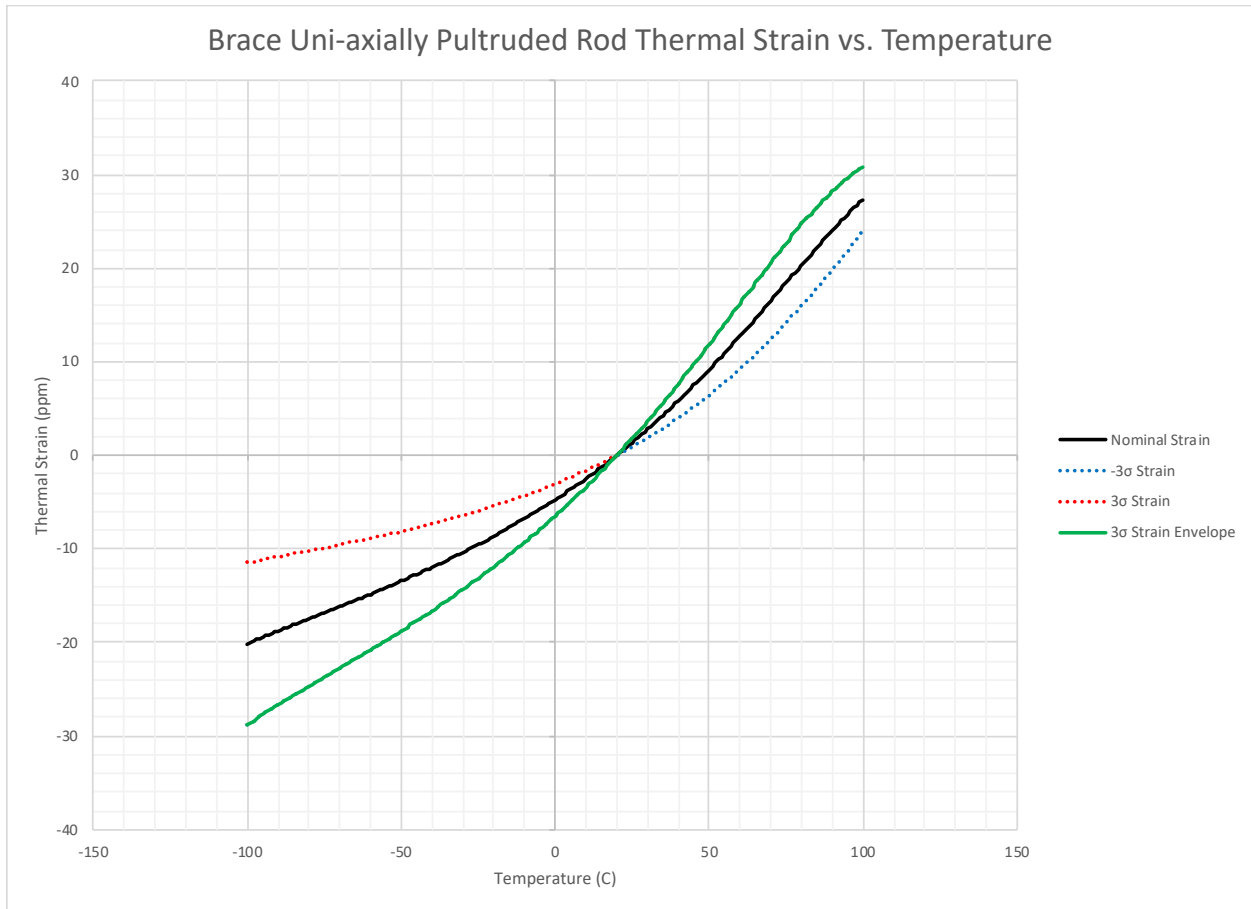


Figure 9-3. Petal brace thermal strain vs temperature. The nominal (average) thermal strain and resulting 3-sigma bounds of all samples is shown, which was used in the worst-case performance prediction.

11 Appendix F: Optical Edge Layup Geometry

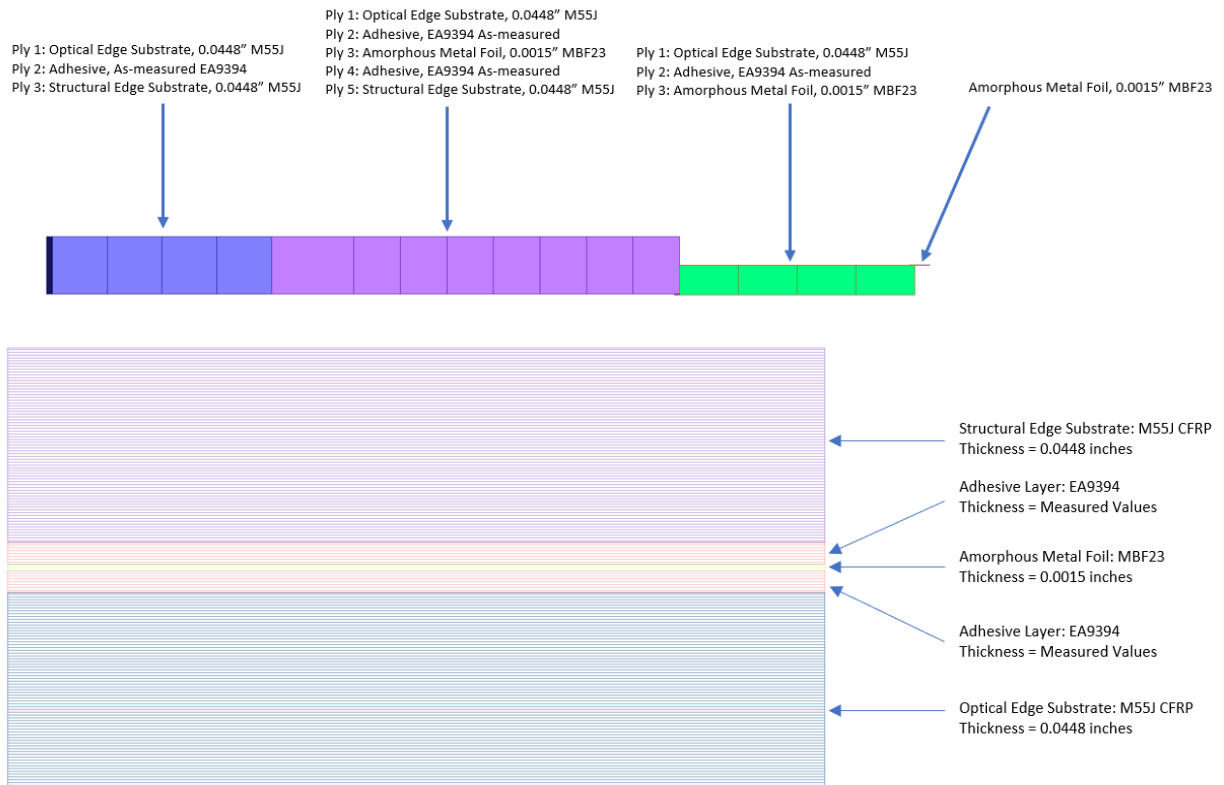


Figure 11-1: Prototype petal test article optical edge layup

12 Appendix G: Batten to Optical Edge Joint Effect on Edge Shape - Midspan Bowing

Upon completion of the thermal deformation test, it was observed that the test data showed a large disparity in behavior of the edge in the midspan measurement locations from that of the initial FEM. Initially, it was thought that the measured midspan deformations were a metrology artifact, as a large array of sensitivity studies were unable to reproduce the measured effect, see Appendix H: Prototype Petal Midspan Sensitivity Studies. Further investigation discovered two sources driving the disparity in results. This section discusses the disparity between the initial prediction and the model changes that identified the source of the disparity in midspan edge behavior.

Initial modeling of the optical edge thermally induced deformations exhibited a sinusoidal deflection of the optical edge with a two-batten frequency, see Figure 12-1 dashed red curve. This FEM predicted sinusoidal deformation was determined, through analysis, to be caused by a thermal strain mismatch between the center spines and the optical edge, creating a shear strain that relieved itself through in-plane bowing of the edge between battens. The two-batten frequency was the result of the petal architecture, which has a two-batten frequency for the diagonal brace.

The test data, however, exhibited a thermally induced deformation with a single-batten frequency, with all midspans bowing outboard in conditions above the reference temperature, and inboard for conditions below the reference temperature. The black-colored curved in Figure 12-1 infers the shape of the edge between black-colored points that are the measured data. Because the as-measured data was not able to be reproduced in the FEA model of the prototype test article, which led the team to believe that a metrology artifact was the cause of the disparity, however, further analysis of metrology sources of error was unable to reproduce the effect.

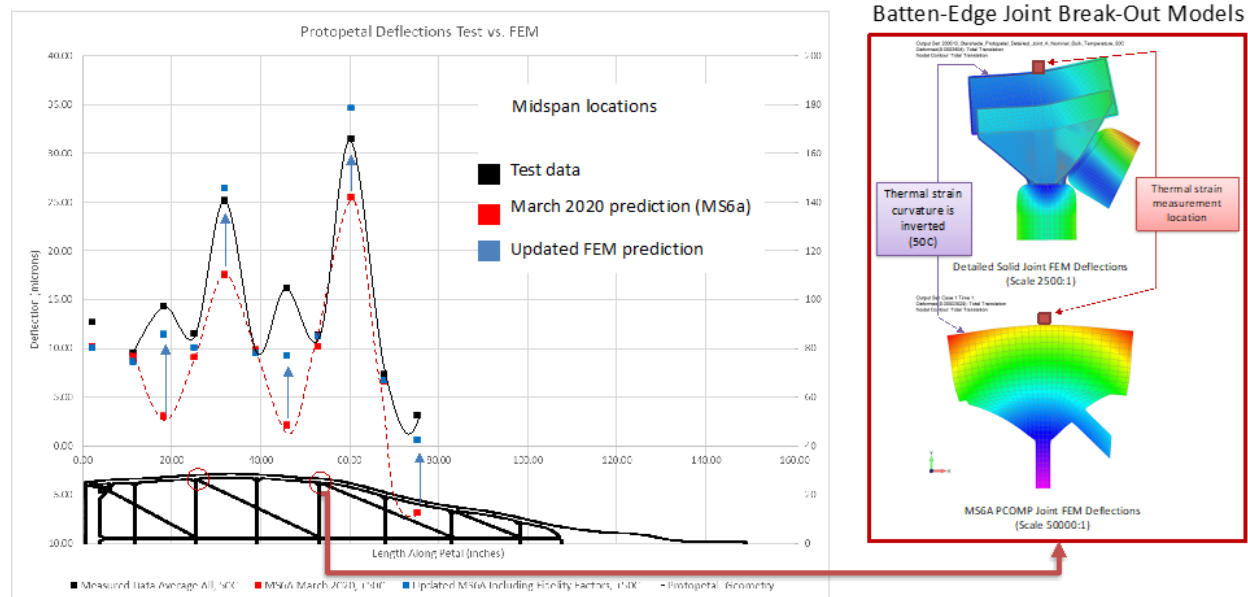


Figure 12-1: Prototype petal model prediction vs test (left) and 2-D vs 3-D joint breakout model behavior (right). Note the 2-D joint actually predicts an inverse edge behavior to that of its 3-D solid FEM counterpart, which contributed to the initial prototype assembly level disparity at the midspan measurement locations.

Further investigation into the batten to optical edge joint discovered two primary sources of error that were ultimately the source of the disparity between model and test data at the midspans:

- 1) Batten and brace transverse CTE material properties for the portions inside the joint
- 2) The use of simplified 2-D elements (CQUAD/PCOMP), versus solid 3-D elements, to represent the joint in the system level petal FEM (for reduced model size)

Joint level model validation – The initial batten to optical edge joint breakout 2-D model was validated against a prototype joint that was measured at Northrop Grumman’s Interferometric Metrology Facility (IMF) before insertion into the petal-level model. This testing method only reports the deformation at one point on the edge, with no additional information on the shape of the edge. For the joint model validation, it was known that manufacturing variation and test setup measurement error would be large sources of variation in the test data as compared to the model prediction. As-manufactured variation includes CFRP material local to the joint materials, bond-line thicknesses and epoxy batch-to-batch material properties. Test setup was also known to be a challenge in that the IMF has an error due to the centering method in which abbe error is corrected with dual laser measurements. These sources of variation combined, the prediction of 0.75 microns as compared to a test measurement of ~2 microns, was considered sufficiently close at the time of correlation, see Figure 12-2, red dot test measurement, and corresponding location on the purple curve.

Further investigation of the 3-D and PCOMP representation of the joint showed a large disparity in edge profile of the joint; this joint level behavior imposes a moment into the edge at the assembly level, causing the edge to bow between battens in response. The primary source of this joint-level edge profile behavior is the material properties of the batten and brace in the transverse direction (x-axis of right image, Figure 12-2). The battens and braces are uni-axial pultruded CFRP, which results in a very near-zero CTE, and high modulus, in the axial direction of the fiber, however the transverse direction is dominated by the high CTE, low modulus, epoxy resin matrix. Initial 3-D modeling of the effect of the transverse material properties exhibited little benefit on model to test correlation for the single test measurement location, see yellow and purple squares, as compared to test location (red square), Figure 12-2. Inclusion of these transverse material properties was, therefore, not predicted to have an assembly level effect on the petal. After prototype petal assembly level test data did not agree at the midspans, a deep dive investigation discovered the disparity in joint edge profile behavior.

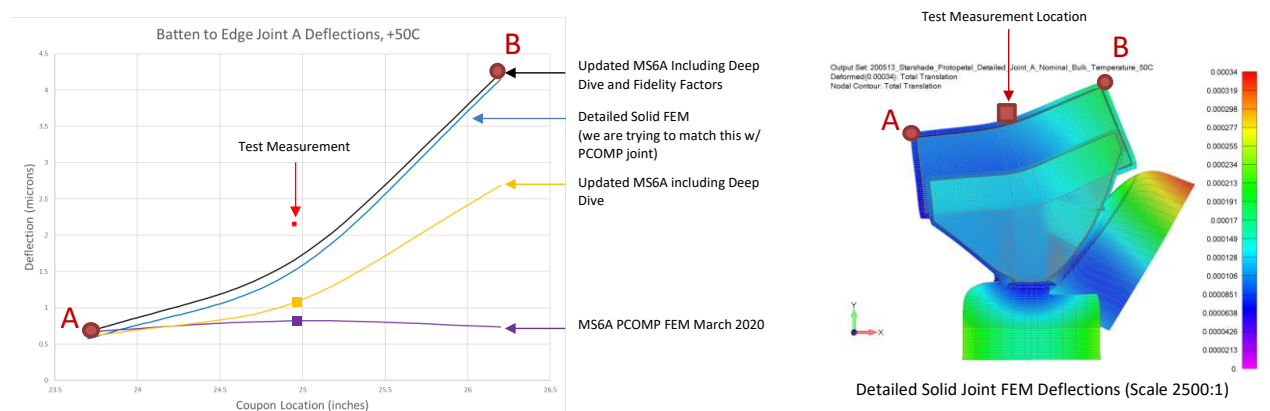


Figure 12-2: Batten to optical edge joint prediction vs test (left) and 3-D solid joint breakout model (right). Ultimately, the behavior of the joint had a very large effect on the edge behavior at the midspans and was important for petal-width bias prediction

The inclusion of the batten and brace transverse material properties in the 2-D CQUAD/PCOMP model was not sufficient to completely close the gap on the joint edge-profile behavior exhibited in the 3-D joint breakout model, yellow vs blue curve Figure 12-2. The reason the 2-D elements do not completely match the 3-D elements is thought to be the large difference in CTE and modulus of the various components in the through-thickness of the joint, which the CQUAD/PCOMP is not able to model as well as the solid elements. The disparity between 2-D

and 3-D elements was closed in utilizing ‘fidelity factors’, multiplication factors that were applied to the 2-D elements material properties that resulted in behavior that more closely matched the 3-D joint behavior. The prototype petal assembly level behavior at the midspans was then verified for the 2-D versus 3-D modeling approach against the prototype petal test data, and was shown to correlate as described in Section 3.4. The 2-D elements were then able to be utilized in the flight system model that included ~56x more instances of these joints than the single prototype petal. The updated flight model was then utilized to predict the thermal deformations for the on-orbit thermal environment, which was assessed against milestone metric (petal width bias) and optical contrast.

13 Appendix H: Prototype Petal Midspan Sensitivity Studies

This appendix contains a list of studies which were performed to understand the cause of the disparity in the as-measured and FEM predicted thermally induced deformations at the midspan locations before the root cause was found, described in Appendix G: Batten to Optical Edge Joint Effect on Edge Shape - Midspan Bowing. In general, the below studies found that changing the parameters of the study could improve the correlation of the FEM to test at some locations, but in general, led to loss of correlation at the remaining measurement points.

- Material CTE Studies: These studies were intended to understand the impact on the midspan deflections when a material did not meet the average measured CTE value.
 - Amorphous metal foil double CTE
 - Amorphous metal foil zero CTE
 - EA9394 epoxy double CTE
 - EA9394 epoxy zero CTE
 - Batten zero CTE
 - Batten double CTE
 - Brace zero CTE
 - Brace double CTE
 - Spine $\frac{1}{2}$ CTE
 - M55J double CTE
 - M55J average CTE (averaged the CTE of all M55J measured data)
 - Root spacer CTE directional test (switched the 0 and 90 degree CTE values)
- Material Modulus Studies: These studies were intended to understand the impact of a softer component on the deflections if a material/joint did not have full stiffness
 - Spine $\frac{1}{2}$ modulus
 - Root $\frac{1}{2}$ modulus
 - Batten $\frac{1}{2}$ modulus
 - Brace $\frac{1}{2}$ modulus
 - EA9394 $\frac{1}{2}$ modulus
 - Brace zero modulus
- Boundary condition studies: This study change the boundary conditions to simulate off nominal constraints
 - Constraints shifted 1 inch in plane
 - Friction between constraint pads and prototype petal
- Thickness studies: This study was intended to see how material thickness might impact the overall petal deflections.
 - EA9394 epoxy double thickness
 - Amorphous metal foil double thickness
 - Amorphous metal foil zero thickness
- Other Studies
 - No Batten to brace connection
 - Initial batten distortion (this study applied an initial curvature to the batten to try and force a different lowest energy state)
 - K6ROT = 1.0 (K6ROT is a parameter in Nastran which controls the out of plane rotational stiffness).
 - Root spacer gaps (modeled discontinuities in the root spaces which decreased the stiffness in the root).

- Joint spacer gaps (modeled the discontinuities in the joint doublers to be filled with air/adhesive).

14 Appendix I: Lattice-Tip Transition Strain

As shown in Appendix A, petal-width bias is a good predictor of the degradation in instrument contrast due to thermally deformed petals, even in cases when the width strain is not uniform along the length of the petal, but has variations as large as 25 ppm around the median value. However, it is expected that local width strain deviations from the petal-width bias – at some large amplitudes – will degrade contrast beyond the level predicted by the petal-width bias metric. Indeed, this is seen in the FEM-predicted deformations for the sun angle of 83° (for both nominal and worst-case material properties).

Figure 14-1 shows the width strain profile of an inner petal at a sun angle of 83° , for the case of nominal material properties. As can be seen, there are large deviations from the petal-width bias (up to about 100 ppm) at the final two even midspans (at roughly $x = 5.6$ m and $x = 6.2$ m). These localized deviations occur at the transition between the truss-like lattice region and the plate-like tip region of the petal. (Note that the high strains in the tip region are due to the small widths in this region; the deformations are small and roughly uniform over the entire petal length.)

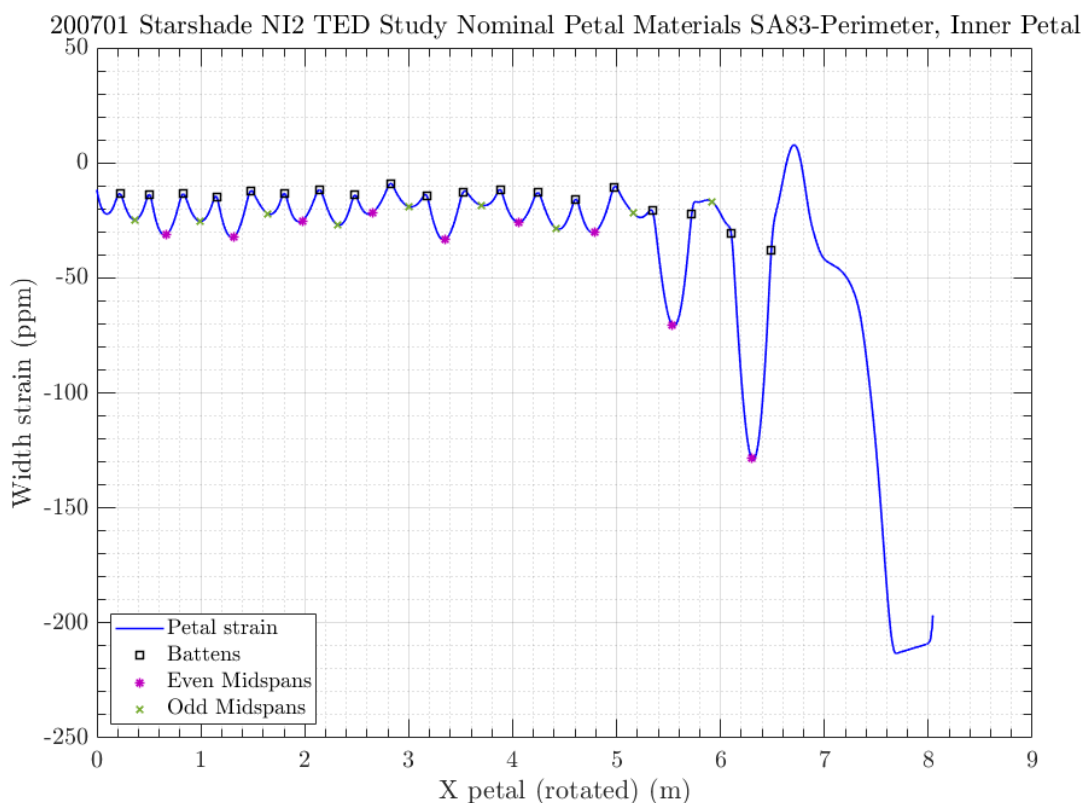


Figure 14-1: Width strain profile of an inner petal with nominal material properties at sun angle of 83° .

These “lattice-tip transition strain deviations” contribute contrast degradation beyond the level expected from a petal with a uniform width strain equal to the petal-width bias. This was determined based on two analyses:

1. There is non-zero contrast degradation when petals with such strain profiles are positioned with inner disk radial strain equal to the petal-width bias. (We expect zero contrast from a uniformly strained starshade, i.e. when the petals and inner disk have uniform dilation.) In fact, there is no inner disk radial strain at which petals thus

deformed can be positioned to give zero contrast degradation. Figure 14-2 shows contrast degradation for the thermally deformed petals (at a sun angle of 83° , for both the nominal and worst cases) placed at varying inner disk radial strains, and it can be seen that there is always non-zero contrast degradation. This indicates that there are contrast degradation mechanisms beyond uniform petal strain.

2. If the width strain at the final two midspans is artificially reduced by 75% (by post-process the FEM results), this extra contrast disappears. This indicates that the source of this extra contrast, beyond what would be predicted by the petal-width bias metric, is the strain in this lattice-tip transition region.

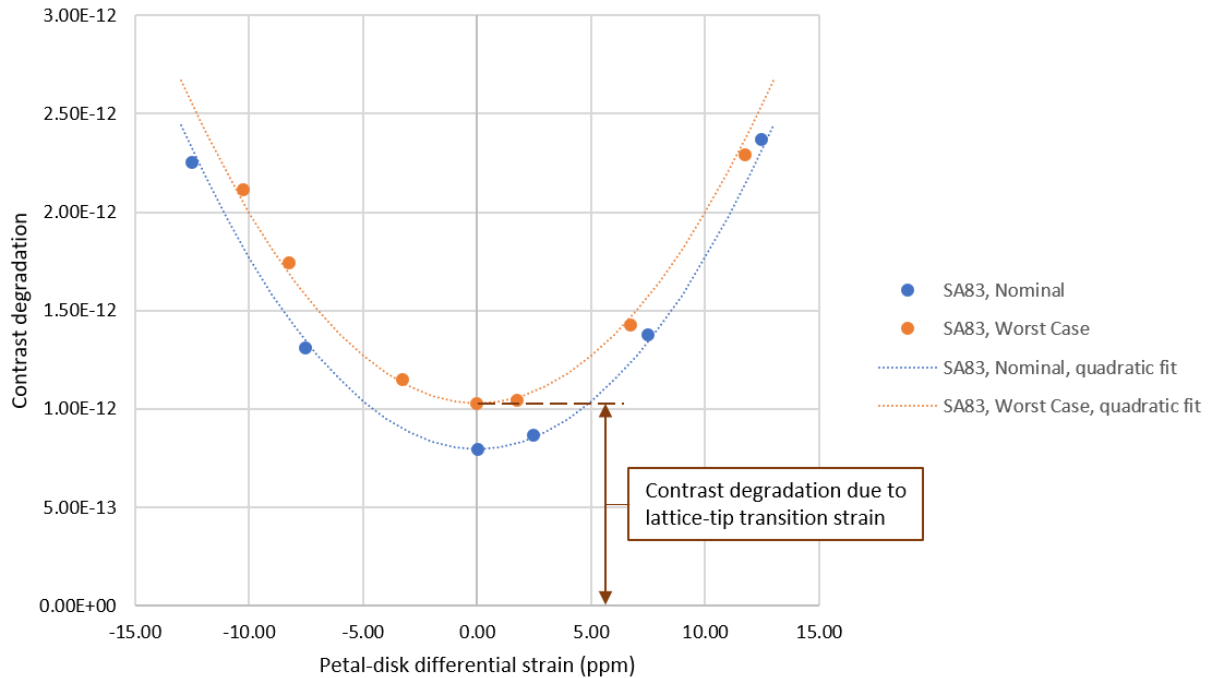


Figure 14-2: Contrast degradation due to thermally deformed petals at a sun angle of 83° , with the petals placed at varying levels of inner disk radial strain.

There is a contrast allocation of $1.45\text{E-}12$ for this effect, as shown in in Table 1-1. Based on the present study, the maximum expected contrast degradation due to this effect is $1.03\text{E-}12$; this is the residual contrast when the worst-case thermally deformed petals (i.e. with 3σ material properties and an additional -10°C temperature bias) at a sun angle of 83° are positioned at the inner disk radial strain equal to the petal-width bias, as shown in Figure 14-2. Thus, the contrast margin is 40% (for the worst case of 83° sun angle with worst case material properties and -10°C temperature bias), expressed as allowable growth.

Moving forward, the intent is to generate petal designs that minimize non-uniform width strains over their lengths, as discussed in Appendix B: Designing-Out Midspan Bowing. (That is, to generate petal structural designs that have thermal deformations as close as possible to a uniform, homogenous, isotropic body.) As such, there have been preliminary studies to ascertain the root cause of and reduce the magnitude of these localized high strains. These preliminary studies have identified differential thermal expansion between the spines and the edges of the petals as possible cause. Further studies and design iterations (e.g. reducing the differential thermal expansion between the spines and the edges) will reduce the magnitude of these effects.

15 Appendix J: Petal-Inner Disk Cross Term

Contrast degradation due to thermoelastic deformation of the starshade depends on the thermal strains of the inner disk and of the petals. Their contributions are bookkept separately: contrast degradation from thermally deformed petals falls under KPP6, and contrast degradation from thermally deformed inner disk falls under KPP8. This appendix describes the approach to addressing the contrast degradation that depends on both the petal and inner disk thermal strains.

There is no contrast degradation associated with equal dilatation of the petals and the inner disk (i.e. uniform strain everywhere on the starshade). For small strains, contrast degradation ΔC due to starshade thermoelastic deformation depends only on the difference between the petal strain ϵ_p and the inner disk strain ϵ_d :

$$\Delta C = a(\epsilon_p - \epsilon_d)^2 \quad \text{Eq. (15-1)}$$

Here, ϵ_p is the uniform strain within the petals, and ϵ_d is the uniform strain within the inner disk. (Note that these quantities vary with sun angle.) For the present case, the constant of proportionality $a = 8.46\text{E-}12/(30\text{ppm})^2$. For the following discussion, it is assumed that the uniform petal strain ϵ_p is the global petal-width bias, and that the uniform inner disk strain ϵ_d is the global inner disk radial bias.

For milestones 6A (petal thermoelastic stability) and 8A (inner disk thermoelastic stability), the approach was to establish a reference strain (also called “ideal” strain) as a function of sun angle (see Section 2.3). This ideal strain curve provided a common reference for the otherwise independent petal and inner disk design efforts. Figure 15-1 plots the ideal strain as a function of sun angle, and also the FEM-predicted inner disk and petal strains from milestones 6A and 8A.

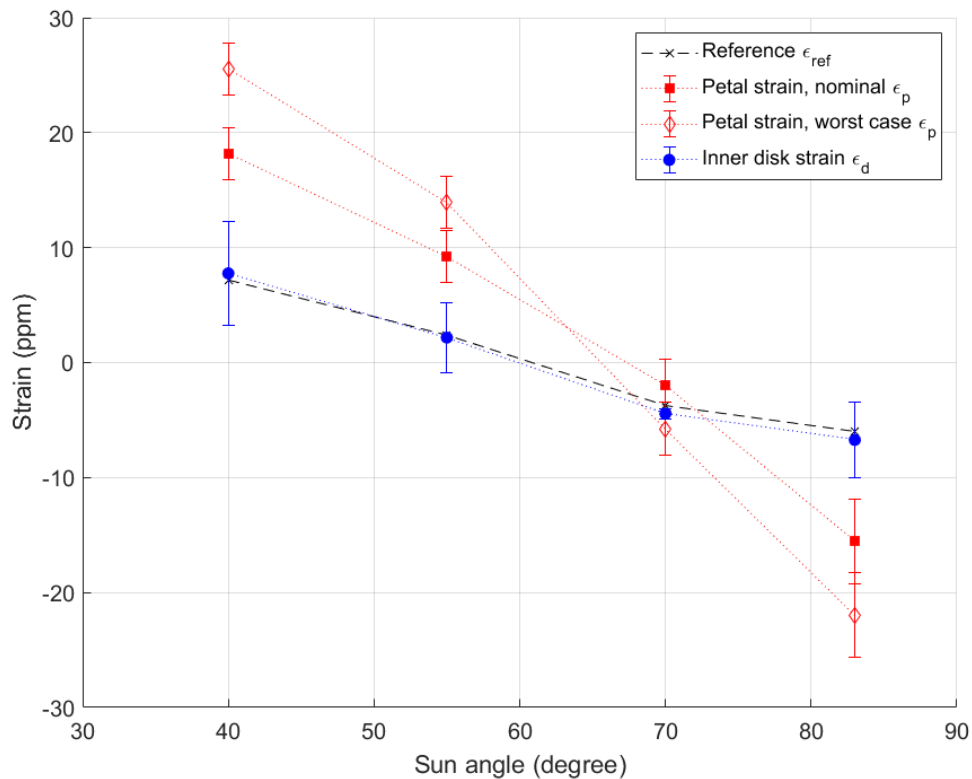


Figure 15-1: The reference or “ideal” strain as a function of sun angle that was used to set a common design reference for the petals and the inner disk for milestones 6A and 8A. The FEM-predicted petal and inner disk strains from those milestones are also shown, as functions of sun angle. The bars represent uncertainty measures.

Based on this reference strain approach and Eq. (15-1), contrast degradation ΔC can be expressed as a function of *strain errors* (i.e. the difference between the predicted and the ideal) of the petal and the inner disk:

$$\Delta C = a[(\epsilon_p - \epsilon_{ref}) - (\epsilon_d - \epsilon_{ref})]^2 \tag{Eq. (15-2)}$$

Here, ϵ_{ref} is the reference or ideal strain. Contrast degradation as a function of petal strain error $(\epsilon_p - \epsilon_{ref})$ and inner disk strain error $(\epsilon_d - \epsilon_{ref})$ is plotted in Figure 15-2. As can be seen, lines of equal contrast have unity slope on this plot, and contrast goes in a quadratic fashion perpendicular to these lines. The strain errors predicted for milestones 6A and 8A are also plotted, as is a red dashed rectangle that indicates the allocated levels of strain.

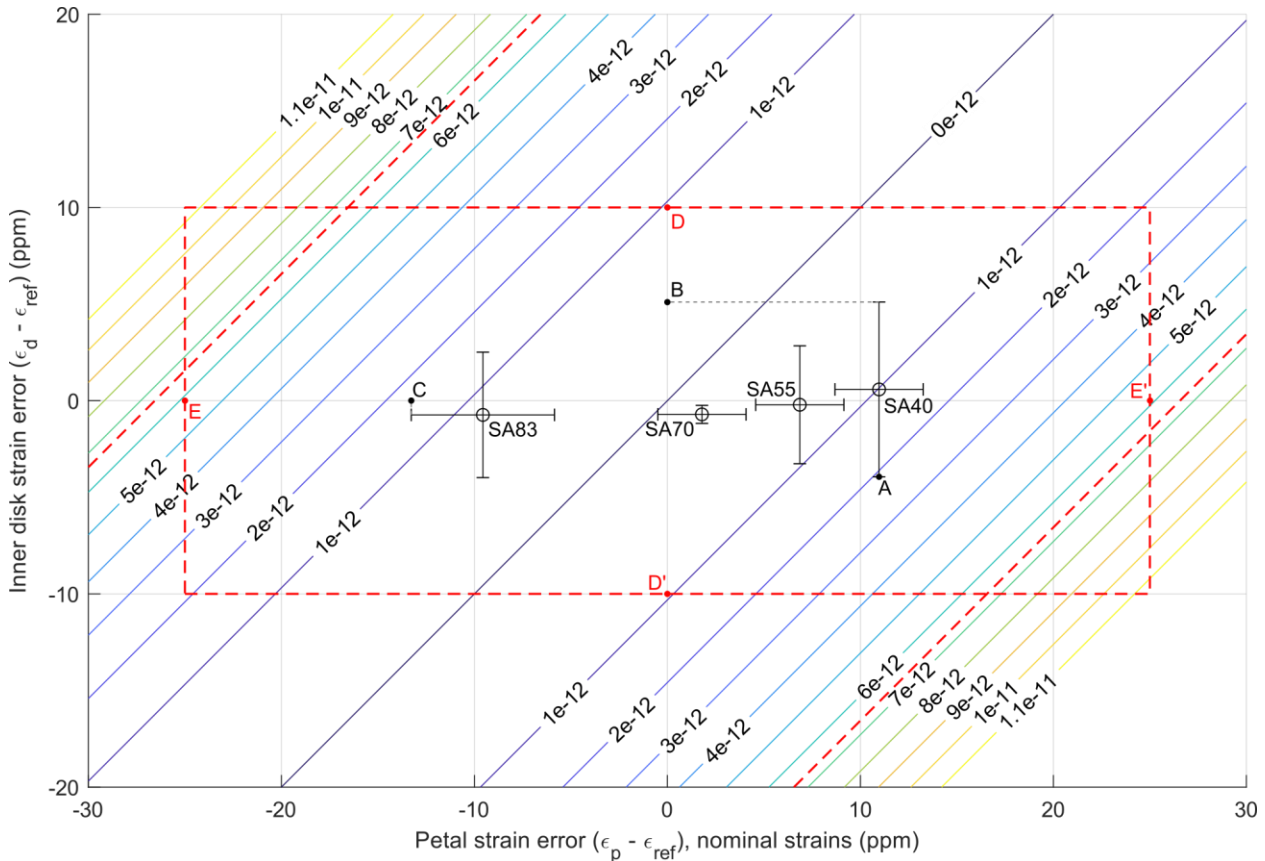


Figure 15-2: Contrast due to petal and inner disk strain errors, using petal strains predicted using nominal temperature predictions and material properties. The petal and inner disk performance (as shown in in Figure 15-1) is plotted for the four sun angles; the error bars indicate uncertainty measures. The red dashed rectangle shows the ± 25 ppm petal strain error allocations and the ± 10 ppm inner disk strain error allocations. Note that the contrast is only due to the global uniform strain terms: global petal-width bias and global inner disk radial bias.

In the current error budget, contrast degradations due to the petals and the inner disk are computed independently (assuming nominal performance for the other subsystem) and then linearly summed. As such, KPP6 and milestone 6A operate only along the *x*-axis of Figure 15-2, and KPP8 and milestone 8A operate only along the *y*-axis. The allocated contrast degradation due to petal strain error is $5.8E-12$ (at points E and E') and the allocated contrast degradation due to inner disk strain error is $0.9E-12$ (at points D and D'). Thus, the total contrast allocation for these two terms combined is $5.8E-12 + 0.9E-12 = 6.7E-12$; this level is indicated by the two diagonal red dashed lines in Figure 15-2. (Note that this is allocation for only the global petal-width bias

and global inner disk radial bias terms; allocations for the random terms are separate.) As is evident from the plot, the strain performance of both the inner disk and the petals can be within the allowable rectangle and exceed the total allocated contrast of $6.7\text{E-}12$ if the performance falls in either of the two triangular regions (bounded by red dashed lines) in the northwest or southeast corners of the plot. However, allocating sufficient contrast degradation (up to $1.15\text{E-}11$) to account for an unfavorable correlation between the thermoelastic strain errors of the petals and the inner disk would be overly conservative. A basic philosophy of the current error budget is to treat individual error terms as independent and uncorrelated. If the error budget were to account for every unfavorable correlation between error terms, the allocations for each term would be very small (and perhaps prohibitively so).

As is shown in Figure 15-2, current predicted performance (with measurement uncertainty) meets the combined contrast allocation of $6.7\text{E-}12$ (and also the individual petal and inner disk allocations). In fact, the effect of the coupling between the petal and inner disk terms is small. Computing contrast degradation due to the petals and the inner disks separately and then summing these contributions:

- Due to the petals alone, maximum expected contrast degradation = $1.7\text{E-}12$ (corresponding to point C in Figure 15-2)
- Due to the inner disk alone, maximum expected contrast degradation = $2.5\text{E-}13$ (corresponding to point B in Figure 15-2)
- Summing these gives contrast degradation = $1.9\text{E-}12$

Comparing this value to the maximum expected contrast degradation considering the petals and inner disk together – which is $2.1\text{E-}12$ (corresponding to point A in Figure 15-2) – it can be seen that the coupling between the petals and the inner disk (i.e. the contrast due to the cross-term between the petals and the inner disk strains) contributes only $0.2\text{E-}12$ additional contrast; this is less than 3% of the total allocation. Overall, the maximum expected contrast of $2.1\text{E-}12$ due to both petals and inner disk has 219% margin (expressed as allowable growth) against the allocation of $6.7\text{E-}12$.

Similar analysis can be performed considering the worst-case petal performance (i.e. with $\pm 10^\circ\text{C}$ temperature bias and 3σ material properties), shown in Figure 15-3. In this case, the coupling between the petals and the inner disk contributes $0.4\text{E-}12$ additional contrast ($4.7\text{E-}12$, point A subtracting the sum of $4.0\text{E-}12$, point C and $2.5\text{E-}13$, point B), which is less than 6% of the total allocation. In this case, the maximum expected contrast of $4.7\text{E-}12$ has 43% margin (expressed as allowable growth) against the allocation of $6.7\text{E-}12$.

It is expected future performance will have similarly small magnitudes of coupling effects between the petals and the inner disk. Additionally, future milestones 6B and 8B will re-establish the ideal strain curve based on the material testing and FEM work done for the present milestones, re-tailor the inner disk material design to meet the expected petal performance, and thus achieve lower strain errors; this approach is explained in Section 5.4. As such, there is low risk of future strain errors falling outside the central hexagon in Figure 15-2. (In fact, even if future errors were uniformly distributed throughout the rectangle, only about 6% of the cases would lie in the two triangles and exceed the $6.7\text{E-}12$ contrast; this is a straightforward consequence of the fact that the two triangles occupy a small area of the rectangle.)

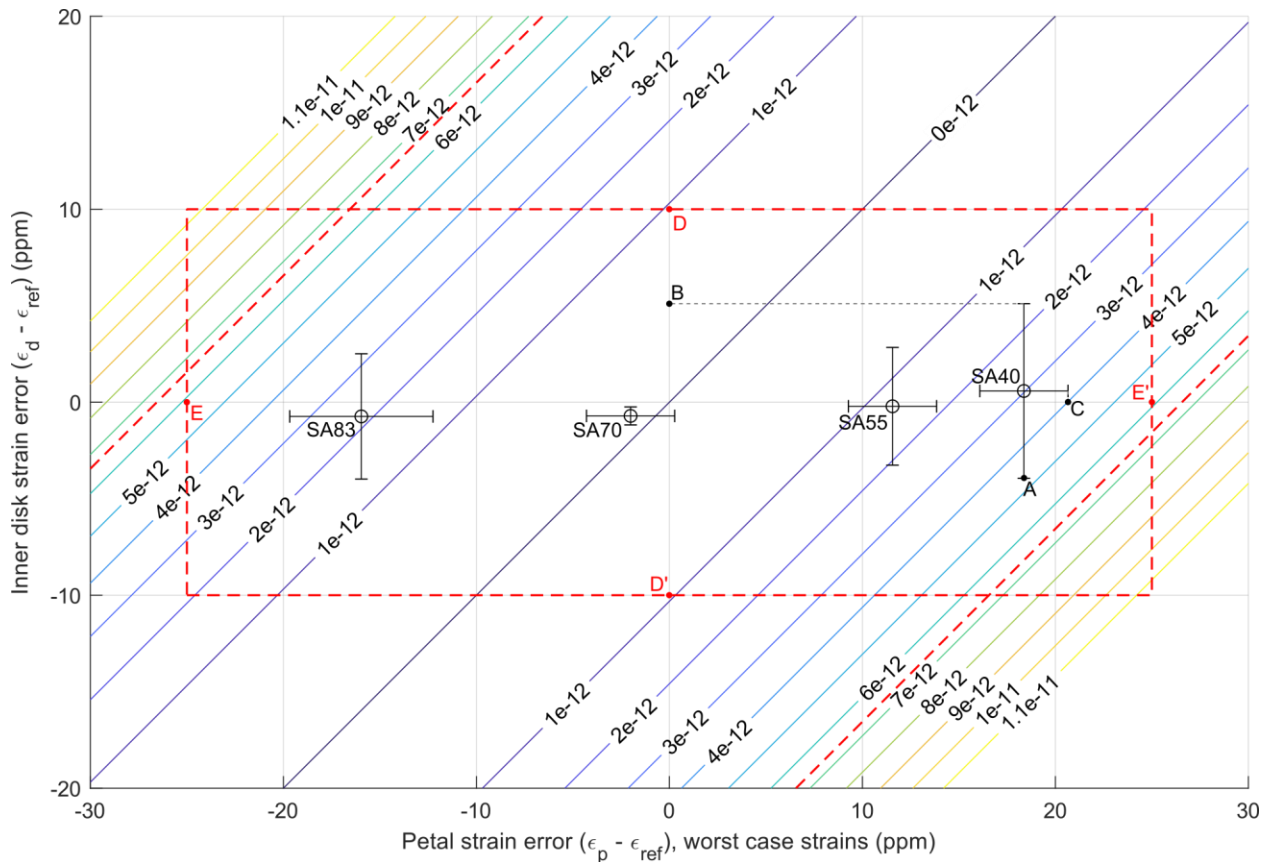


Figure 15-3: Contrast due to petal and inner disk strain errors, using petal strains predicted using additional $\pm 10^\circ\text{C}$ temperature biases, and worst-case 3σ material properties. The petal and inner disk performance (as shown in in Figure 15-1) is plotted for the four sun angles; the error bars indicate uncertainty measures. The red dashed rectangle shows the ± 25 ppm petal strain error allocations and the ± 10 ppm inner disk strain error allocations. Note that the contrast is only due to the global uniform strain terms: global petal-width bias and global inner disk radial bias.

In conclusion, the present approach of allocating contrast degradations to the petals and the inner disk thermal strains independently without consideration of the coupling between them is sufficiently conservative. The strength of the coupling in the predicted results is small, and there are large margins between the allocation and the maximum expected contrasts, even when considering the worst-case petal strain predictions.